UNIVERSITY OF CALIFORNIA
RIVERSIDE

Characterizing Extremely Red Quasars & Quasar Outflows Using Rest-UV Spectroscopy

A Dissertation submitted in partial satisfaction
of the requirements for the degree of

Doctor of Philosophy

in

Physics

by

Jarred Orion Gillette

September 2023

Dissertation Committee:

Prof. Fred Hamann, Chairperson
Prof. Gaby Canalizo
Prof. Laura Sales
Prof. Brian Sienna

The Dissertation of Jarred Orion Gillette is approved:

_____

_____

_____

_____

Committee Chairperson

University of California, Riverside

Acknowledgments

I would like to thank my family, who have been understanding and supportive throughout my journey to achieve this important milestone. Completing this work would not have been possible without the guidance and support of my research advisor, Fred Hamann. I appreciate and thank my collaborators for their contributions that have made this work possible and their valuable feedback. Thank you to all of the astronomy faculty at UCR-especially my committee members: Gaby Canalizo, Brian Siana, and Laura Sales-and all of the astronomy graduate students and postdocs for building a supportive community.

I acknowledge financial support from UCR through the Chancellor's Distinguished Fellowship. My team acknowledges support from the USA National Science Foundation grant AST-1911066.

The observations for this work utilized the following facilities for the KCWI integral-field spectrograph on the Keck II telescope at the W. M. Keck Observatory.

To complete the analyses in this work, I acknowledge the following open source Python packages: Astropy (Astropy Collaboration et al. 2013, 2018), Matplotlib (Hunter 2007), NumPy (Oliphant 2007), and SciPy (Oliphant 2007).

Some of the data presented herein were obtained at the W. M. Keck Observatory, which is operated as a scientific partnership among the California Institute of Technology, the University of California and the National Aeronautics and Space Administration. The Observatory was made possible by the generous financial support of the W. M. Keck Foundation. Data presented herein were partially obtained using the California Institute of Technology Remote Observing Facility. The authors wish to recognize and acknowledge the very significant cultural role and reverence that the

summit of Maunakea has always had within the indigenous Hawaiian community. We are most fortunate to have the opportunity to conduct observations from this mountain.

This dissertation contains drafts of articles that have been submitted (Chapter 2, Chapter 3, and Chapter 4) for publication by Oxford University Press in the Monthly Notices of the Royal Astronomical Society written by me and my collaborators.

ABSTRACT OF THE DISSERTATION

Characterizing Extremely Red Quasars & Quasar Outflows Using Rest-UV Spectroscopy

by

Jarred Orion Gillette

Doctor of Philosophy, Graduate Program in Physics
University of California, Riverside, September 2023
Prof. Fred Hamann, Chairperson

This PhD dissertation investigates the phenomenon of extreme outflows in quasars and its implications for galaxy evolution and quasar feedback. The study focuses on two distinct quasar populations: extremely red quasars (ERQs) and normal quasars, both exhibiting powerful outflows, but in different contexts.

The first part of the dissertation explores a population of extremely red quasars (ERQs) with exceptionally fast outflows, likely representing a young stage of galaxy evolution. The ERQs, situated at a median redshift of $z \approx 2.6$, are studied through Keck/KCWI integral field spectra of 11 quasars. Analysis of their properties, such as median color (i–$W3$ = 5.9 mag), median bolometric luminosity ($\langle L_{\rm bol} \rangle \approx 5 \times 10^{47}$ erg s^{-1}), Lyα halo luminosity ($\langle L_{\rm halo} \rangle = 5 \times 10^{43}$ erg s^{-1}), and maximum linear size (>128 kpc), reveals similarities to blue quasars while exhibiting unique characteristics. The ERQ halos have compact and circularly symmetric inner regions, and they are kinematically quiet. Despite their powerful outflows, there is no clear evidence for feedback on circumgalactic scales, potentially due to long outflow travel times. The dissertation also confirms the importance of narrow

Lyα emission spikes in ERQ aperture spectra for systemic redshift determination and measuring outflow speeds.

In the second part, the dissertation investigates the driving factors behind fast outflows in normal quasars using a large sample of 39,249 quasars at a median redshift of $\langle z \rangle \approx 2.17$. Redshifts based on the Mg II emission line are re-measured, enabling the exploration of unprecedented outflow velocities (>6000 km s^{-1}) while ensuring statistical significance and uniformity. Analysis reveals significant correlations, indicating that higher Eddington ratios and softer far-UV continua (hν >54.4 eV) are primary contributors to faster outflows. Supporting evidence suggests that radiative line-driving may generate extreme outflow velocities, influenced by multiple factors. This study emphasizes the importance of considering a multi-dimensional parameter space to understand the fundamental causes of extreme outflows in quasars.

In conclusion, this comprehensive dissertation provides valuable insights into extreme outflows in quasars, encompassing both ERQs and normal quasars. The findings contribute to our understanding of the early stages of galaxy evolution and the impact of quasar feedback on host galaxies. The study highlights the complexities of quasar outflows and their driving mechanisms, underscoring the significance of multi-dimensional analyses in future studies.

Contents

List of Figures

List of Tables

Chapter 1

Introduction

Quasars are powered by the rapid accretion of material onto supermassive black holes at the centers of galaxies. They are fundamental to understanding massive galaxy evolution, and the interplay between feedback mechanisms governing supermassive black hole growth and star formation. These luminous objects are associated with various triggering events such as galaxy mergers, or streams of infalling gas (Hopkins et al. 2006, 2008; Somerville et al. 2008; Kereš et al. 2009; Dekel et al. 2009; Faucher-Giguère & Kereš 2011; Fumagalli et al. 2014; Glikman et al. 2015). These triggers are instrumental in shaping galaxies by inducing starbursts and influencing quasar activity, as well as generating outflows that can potentially impact their surroundings (Costa et al. 2014; Nelson et al. 2015; Suresh et al. 2019). Theoretical frameworks propose an evolutionary scenario wherein a central black hole grows unnoticed until feedback-driven outflows clear the obscuring medium, revealing a luminous quasars (Sanders et al. 1988; Di Matteo et al. 2005; Hopkins et al. 2006, 2008, 2016; Rupke & Veilleux 2011, 2013; Liu et al. 2013; Stacey et al. 2022).

In this context, red quasars stand as pivotal subjects for investigating the hypothesis that obscured quasars might represent an early stage in their evolution. Red quasars are potentially reddened by dust produced in major starbursts triggered by galaxy mergers or cold-mode accretion, and could display hallmarks of youth such as high accretion rates, enhanced infall from the intergalactic medium, or pronounced outflows (Glikman et al. 2015; Wu et al. 2018; Zakamska et al. 2019). Among these, Extremely Red Quasars (ERQs) have emerged as a particularly intriguing subclass, identified based on their extremely red rest-UV to mid-IR colors (i–$W3$> 4.6 mag; Ross et al. 2015; Hamann et al. 2017). ERQs exhibit distinct spectral properties, including strong and blueshifted C IV emission lines, notable wingless profiles, and fast outflows traced by [O III] emission lines (Hamann et al. 2017; Perrotta et al. 2019). These features hint at potent accretion-disk outflows that may shape their unique characteristics (Zakamska et al. 2016; Hamann et al. 2017; Perrotta et al. 2019).

ERQs inhabiting a rabid transition phase in their evolution may show signs of disruption in their environment, which may correlate with properties of the quasar emission and outflows. We delve into the study of Lyα halo emission as indicators of the galactic environment and quasar feedback processes. These halos provide a window into the extended circumgalactic regions, offering valuable insights into the interplay between quasar-driven outflows and the surrounding environment. Building upon the insights from our examination of Lyα halo characteristics around ERQs, we perform a more detailed analysis of ERQ outflows, aiming to find the underlying mechanisms that give rise to their distinctive spectral features.

Transitioning from the investigation of ERQ outflows, and their potential influence the galactic environment, we study quasar outflows more generally. This transition in focus allows us to extend our understanding beyond ERQs, and delve into the fundamental mechanisms that determine

outflow processes in quasars more broadly. Through this exploration, we contribute to a more comprehensive understanding of the interrelation between quasar attributes, outflow speeds, and their role in shaping the evolving galaxy/quasar.

Determining the precise systemic redshifts for quasars is crucial for accurately assessing the properties of their outflows. However, the presence of outflow signatures complicates this task, as typical redshift indicators such as C IV emission lines can be blueshifted from their rest wavelengths (Richards et al. 2011; Coatman et al. 2019; Rankine et al. 2020). To address this challenge, we meticulously determined systemic redshifts through careful fitting of Mg II emission lines, we achieve a unified approach to studying an unprecedented range of outflow velocities across a substantial sample size. This approach allows us to closely examine the correlations between blueshifts and a multitude of quasar characteristics. With accurate redshifts established, we investigate the link between outflow properties, characterized by blueshifted broad emission lines, and various quasar characteristics, aiming to unveil patterns indicative of feedback and quasar evolution (Hopkins et al. 2008, 2016; Wylezalek & Zakamska 2016; Veilleux et al. 2016; Rupke et al. 2017; Baron et al. 2017; Vayner et al. 2021).

1.1 Dissertation Outline

The work in this dissertation strives for a more comprehensive exploration of quasar outflows as potential feedback mechanisms in ERQs, and outflow properties in general, through the lens of three distinct publications. Our journey unfolds as follows:

Chapter 2 focuses on ERQs and their Lyα halos. We delve into the unique features of ERQ spectra and their Lyα halo emission, which provide insights into the extended circumgalactic region.

By employing methodologies such as integral field spectroscopy with the Keck Cosmic Web Imager, and analyzing the spatial and kinematic properties of circumgalactic gas, we uncover the complex interplay between quasar-driven outflows and the host galaxy. This investigation sheds light on the potential feedback mechanisms at play, shaping ERQ evolution within their galactic environments.

Chapter 3 builds upon the insights from Chapter 2, and we transition to a broader analysis of ERQ outflows. In this publication, we implicate the physical conditions and driving forces behind the distinctive spectral features of ERQs, by combining catalogued observations of gas outflows with our gained insight for approximating the true systemic redshift. By focusing on the outflow properties of ERQs, we contribute to a deeper understanding of their role in quasar evolution and the mechanisms that govern their behavior.

Chapter 4 expands our investigation beyond ERQs, and broadens our scope to encompass a more comprehensive study of quasar outflows. With a focus on understanding the link between quasar properties and the velocities of their outflows, we delve into the fundamental mechanisms underlying outflow processes. By dissecting the intricate connections between quasar attributes and outflow dynamics, we provide insights into the driving mechanisms that shape these phenomena across a diverse range of quasar systems.

Finally, the main conclusions of the dissertation and potential future work are summarized in Chapter 5. Through the synthesis of these three publications, we aim to understand ERQs, their outflow properties, quasar outflows in general, contributing to a holistic understanding of the complex interplay between these luminous entities and their evolving galactic environments.

Chapter 2

Paper I: Compact and Quiescent Circumgalactic Medium and Lyα Halos around Extremely Red Quasars (ERQs)

2.1 Abstract

Red quasars may represent a young stage of galaxy evolution that provide important feedback to their host galaxies. We are studying a population of extremely red quasars (ERQs) with exceptionally fast and powerful outflows, at median redshift $z = 2.6$. We present Keck/KCWI integral field spectra of 11 ERQs, which have median color i–$W3 = 5.9$ mag, median $\langle L_{\rm bol} \rangle \approx 5 \times 10^{47}$ erg s^{-1}, Lyα halo luminosity $\langle L_{\rm halo} \rangle = 5 \times 10^{43}$ erg s^{-1}, and maximum linear size >128 kpc. The ERQ halos are generally similar to blue quasar halos, following known trends with $L_{\rm bol}$ in halo properties. ERQs have halo symmetries similar to Type-I blue quasars, suggesting Type-I spatial orientations.

ERQ $\langle L_{\rm halo} \rangle$ is ∼2 dex below blue quasars, which is marginal due to scatter, but consistent with obscuration lowering photon escape fractions. ERQ halos tend to have more compact and circularly symmetric inner regions than blue quasars, with median exponential scale lengths ∼9 kpc, compared to ∼16 kpc for blue quasars. When we include the central regions not available in blue quasar studies (due to PSF problems), the true median ERQ halo scale length is just ∼6 kpc. ERQ halos are kinematically quiet, with median velocity dispersion 293 km s^{-1}, consistent with expected virial speeds. Overall we find no evidence for feedback on circumgalactic scales, and the current episode of quasar activity, perhaps due to long outflow travel times, has not been around long enough to affect the circumgalactic medium. We confirm the narrow Lyα emission spikes found in ERQ aperture spectra are halo features, and are useful for systemic redshifts and measuring outflow speeds in other features.

2.2 Introduction

Quasars are supermassive black holes which grow as they rapidly accrete infalling material at the center of their host galaxy. At high redshift, accretion can coincide with galactic assembly via galaxy mergers, or streams of infalling gas. Major merger activity could trigger both star formation and growth of the central black hole (Hopkins et al. 2006, 2008; Somerville et al. 2008; Glikman et al. 2015). The process of infalling gas, cold-mode accretion, may also be a dominant mechanism for supplying matter for the formation of galaxies, triggering starbursts, and fueling quasars (Kereš et al. 2009; Dekel et al. 2009; Faucher-Giguère & Kereš 2011; Fumagalli et al. 2014). Accretion by infall can coincide with outflows as the subsequent galaxy activity generates feedback, influencing the galaxy's formation (Costa et al. 2014; Nelson et al. 2015; Suresh et al. 2019). A possible

evolutionary scheme is where the central back hole grows in obscurity until feedback generates outflows, which clear the obscuring interstellar medium, to reveal a luminous quasar (Sanders et al. 1988; Di Matteo et al. 2005; Hopkins et al. 2006, 2008, 2016; Rupke & Veilleux 2011, 2013; Liu et al. 2013; Stacey et al. 2022).

Red quasars are important for testing the hypothesis that obscured quasars may be in a young evolution phase. Young quasars may be reddened by dust created in a major starburst inside the galaxies, triggered by a merger or cold-mode accretion. They may show signs of early evolution such as rapid accretion or more powerful outflows from the quasar, or more infall from the intergalactic medium, as they transition in to blue quasars. Studies of red/obscured quasars have found many to be in mergers or high-accretion phases (Glikman et al. 2015; Wu et al. 2018; Zakamska et al. 2019). Extremely Red Quasars (ERQs) display powerful outflow signatures, and are interesting candidates for studying a young quasar phase in the galaxy/quasar evolution scheme (Hamann et al. 2017).

ERQs were first discovered among the Baryon Oscillation Spectroscopic Survey (BOSS, Pâris et al. 2017a) in the Sloan Digital Sky Survey-III (SDSS, Eisenstein et al. 2011) and the ALLWISE data release (Cutri et al. 2011, 2013) of the Wide-field Infrared Survey Explorer (WISE, Wright et al. 2010a). They were initially described in Ross et al. (2015), and were further refined in Hamann et al. (2017) to ~200 objects, characterized by their extremely red colors (i–$W3$>4.6 mag; Hamann et al. 2017). Currently known ERQs are at comic noon redshifts $z \sim 2$–4, and are on the high end of quasar bolometric luminosities $L_{\rm bol} > 10^{47}$ erg s^{-1}.

ERQs exhibit other extreme spectral properties that make them unique compared to other red quasar samples, beyond being extremely red. Many have unusually strong and/or blueshifted broad emission lines, with C IV rest equivalent widths >100Å, and peculiar wingless profiles with

high kurtosis (Monadi & Bird 2022). They also frequently have unusual emission line flux ratios (e.g. high N v λ1240/Lyα or N v λ1240/C iv λ1549). These broad line features indicate outflow properties controlled by accretion, and reside on scales of tens of parsecs (Zhang et al. 2017; Alexandroff et al. 2018). ERQs also have the most blueshifted [O iii] λ5007 emission lines ever reported, with speeds $>$ 6000 km s^{-1}(Zakamska et al. 2016; Perrotta et al. 2019). [O iii] is significant because it traces gases on galactic scales, at tens of kpc, and are low density forbidden transitions (Hamann et al. 2011; Vayner et al. 2021). Outflows at these galactic scales carry energy that could generate feedback in the host galaxy. This suite of properties found in ERQ spectra indicate more extreme physical conditions than what are found in typical quasar populations, and beyond orientation effects.

Understanding ERQs and their evolutionary nature has launched a multi-faceted study of their physical environments. ERQ host galaxies have been directly imaged with *Hubble Space Telescope* to look for signs of merger activity (Zakamska et al. 2019). Major merger activity was not found in most of their objects, but observations of high redshift quasars have added difficulty subtracting point-spread function in two dimensional imaging. Another approach is to study the kinematics and physical extent of the outflowing gas, specifically, the [O iii] emission (Perrotta et al. (2019); Vayner et al. (2021); Lau et al. in preparation). Past studies have found [O iii] outflows to be spatially compact, not extended to circumgalactic regions, and at kpc scales of the nuclear regions of host galaxies (Vayner et al. 2021). A third method of investigating ERQ environments is through their halo emission. The circumgalactic medium (CGM) has an important role in understanding the evolution of galaxies (Tumlinson et al. 2017), and is the site of interaction for outflows from galaxies and the inflows from the intergalactic medium.

High redshift quasars have been found to have large gas reservoirs in the CGM, observed in fluorescent Lyα emission, and have been interpreted as filaments or inflowing gas in cold-mode accretion (Borisova et al. 2016a; Arrigoni Battaia et al. 2019; Cai et al. 2019). ERQs are a well defined and uniform sample from BOSS, and make good targets for studying their Lyα halos for quasar evolution.

In this paper, we aim to investigate whether ERQs represent an earlier evolutionary stage compared to regular luminous blue quasars, which are characterized by strong rest-UV emission lines and blue color across the rest-frame mid-UV to Near-IR spectral range. With the embedded quasar evolution scheme, we investigate ERQs for evidence they are different or unusual from normal blue quasars at the same redshifts and luminosities. This could be evidence for feedback, but also signatures of more intense infall or chaotic mergers, more/less asymmetries, and/or suppressed Lyα halo emission due to the quasar obscuration. Detailed analysis of the Lyα emission from ERQs can provide key insights into this question.

Secondarily we want to investigate the spatial origin of a peculiar, and narrow, Lyα emission component frequently seen in spatially unresolved ERQ spectra. It often appears as a "spike" on top of the broad Lyα emission, and it's narrow width (FWHM $<$ 1,000 km s^{-1}) indicates the emission is far from the quasar's broad line region (BLR). The spike sometimes coincides with the rest frame of other narrow emission lines (e.g. He II and narrow [O III], Hamann et al. (2017) and Perrotta et al. (2019), respectively). We want to determine whether this sharp feature originates in the extended inner-halo region, as hypothesized in Hamann et al. (2017), and discussed or used in Perrotta et al. (2019) and Lau et al. (2022). This investigation is motivated from observations that many broad emission lines in ERQs are often blueshifted, and involved in outflow, that would

typically be at the systemic in other quasar populations (Hamann et al. 2017; Perrotta et al. 2019). This blueshifting would systemically bias automated redshift estimates generated in BOSS, making outflows appear weaker. If the source of the Lyα spike is far from the galactic center, where outflows would take place, and is extended in the galactic halo, then it would not be involved in strong outflows and would provide a better systemic redshift estimate. Confirming the narrow Lyα emission can be used as a better systemic redshift of ERQs also confirms outflows hypothesized in the discussions aforementioned, and helps constrain velocities for future work on ERQ outflows (Gillette et al. 2023a).

Our team already analyzed one Lyα halo from our sample that is the reddest known ERQ (J0006+1215, in Lau et al. (2022)), which displays an extremely fast [O III] λ5007 outflow at $\sim$6000 km s^{-1}(Perrotta et al. 2019). The Lyα halo spans $\sim$100 kpc, and the narrow Lyα emission spike in the quasar spectrum originates from the inner halo. It is kinematically quiet, with velocity dispersion of $\sim$300 km s^{-1} and no broadening above the dark matter circular velocity down to the spatially resolved limit $\sim$6 kpc from the quasar. Lau et al. (2022), hereafter L22, proposed that the He II λ1640/Lyα ratio of the inner halo and the asymmetry level of the overall halo in J0006+1215 are dissimilar to Type-II quasars, suggesting unique physical conditions for J0006+1215 that are beyond orientation differences from other quasar populations. We note the Type-I/II quasar classification dichotomy, because other studies find that Type-IIs tend to show more asymmetric halos, consistent with more edge-on views of the quasar. It also correlates strongly with the level of obscuration toward the nucleus Greene et al. (2014), and we want to distinguish ERQs from obscured quasar populations explained by orientation effects.

In this paper we analyze Lyα halos of a sample of ERQs, and compare them to those around other quasars as a unique population. It is organized as follows. Section 2 describes the selection method for ERQ observations, their data reduction, calibration, and post-processing. Section 3 describes the measured halo properties of ERQ sample, such as the extended line emission surrounding the quasar, and analysis results of size, morphology, surface brightness (SB), and kinematics of the extended emission. In Section 4 we discuss implications for quasar youth, feedback, and further for quasar studies. Section 5 concludes the paper. Throughout this paper we adopt a Λ-CDM cosmology with $H_0 = 69.6$ km s^{-1} Mpc^{-1}, $\Omega_M = 0.286$ and $\Omega_\Lambda = 0.714$, as adopted by the online cosmology calculator developed by Wright (2006). All magnitudes are on the AB system. Reported wavelengths are in vacuum and in the heliocentric frame.

2.2.1 Sample Selection

We select targets for our study from the sample of 205 ERQs in Hamann et al. (2017), and in the redshift range $2.0 \leq z \leq 3.6$, all have coverage of the Lyα feature at rest-frame 1215.7Å. ERQs showing a narrow Lyα emission in the profile of their BOSS spectra, by visual inspection, were prioritized during observing to determine if the emission originates from an extended halo. We also prioritize ERQs in Perrotta et al. (2019), which have [O III] measurements, which were shown to have color-correlated powerful outflows at tens of kpc scales, and may be more likely to show evidence of feedback in the halo. We also prefer the reddest available ERQs. We chose the best available targets subject to weather and scheduling constraints, and prioritize targets fitting several of the criteria above.

Table 2.1: ERQ properties in our program. z_{em} is from the SDSS DR12Q BOSS catalog emission-line measurements, $z_{\rm halo}$ is computed from the Lyα line emission from the extended halo. C IV FWHM is from emission line fitting done in Hamann et al. (2017). [O III] emission blueshift measurements, when available, are from Perrotta et al. (2019), and blueshifted from CO emission measurements by F. Hamann et al. (2023 in prep.), and discussed in Gillette et al. (2023a). Bolometric luminosity is estimated from the W3 magnitude. ERQ J0834+0159 was observed under cloudy conditions, and is omitted from analysis of Lyα halos.
Notes. [a] Quasars with their narrow Lyα component clipped from the quasar emission template. [b] Redshift approximated by Lyα line peak from an inner 1-arcsec aperture spectrum. [c] Blueshift relative to a redshift approximated by Lyα line peak from an inner 1-arcsec aperture spectrum.

ERQ Name	z_{em}	$z_{\rm halo}$	C IV FWHM (km s^{-1})	[O III] v_{98} (km s^{-1})	W3 (mag)	i–$W3$ (mag)	$L_{\rm bol}$ (erg/s)
J0006+1215[a]	2.31	2.3184	4540±200	−6224.99	14.1	8.0	7.58e+47
J0220+0137[a]	3.14	3.1375	2613±161	...	15.8	6.2	3.68e+47
J0834+0159	2.59	2.5882[b]	2863±65	−4426.08	14.9	6.0	4.98e+47
J1145+5742[a]	2.79	2.8747	9103±446	...	14.3	4.8	1.14e+48
J1232+0912	2.38	2.4034	4787±52	−7026.20	14.3	6.8	6.33e+47
J1451+0132[a]	2.77	2.8130	6231±156	...	14.7	5.7	6.78e+47
J1451+2338[a]	2.62	2.6348	4166±124	...	15.0	5.5	4.56e+47
J1652+1728[a]	2.94	2.9548	2403±45	−2534.00[c]	14.9	5.4	6.80e+47
J1705+2736	2.45	2.4461	1301±22	...	15.5	5.1	2.43e+47
J2215−0056	2.51	2.5074	4280±112	−3876.95	16.0	6.2	1.51e+47
J2254+2327	3.09	3.0825	4412±146	...	16.5	5.5	1.68e+47
J2323−0100	2.36	2.3831	3989±62	−6458.03	15.2	7.2	2.88e+47
Median	2.61	2.6348	4223	...	15.0	5.9	4.56e+47

Table 2.2: ERQ observing details for our program. ERQ J0834+0159 was observed under cloudy conditions, and is omitted from analysis of Lyα halos.

ERQ Name	RA (J2000)	Dec (J2000)	Observation Date	Exposure Time (s)
J0006+1215[a]	00:06:10.67	12:15:01.2	2019-10-02	4,200
J0220+0137[a]	02:20:52.11	01:37:11.1	2019-10-02	8,400
J0834+0159	08:34:48.48	01:59:21.2	2019-03-02	6,000
J1145+5742[a]	11:45:08.00	57:42:58.6	2019-03-02	10,800
J1232+0912	12:32:41.75	09:12:09.3	2020-05-26	4,800
J1451+0132[a]	14:51:13.61	01:32:34.1	2019-03-02	10,800
J1451+2338[a]	14:51:48.01	23:38:45.4	2020-05-26	8,400
J1652+1728[a]	16:52:02.61	17:28:52.3	2020-05-26	4,800.0
J1705+2736	17:05:58.56	27:36:24.7	2020-05-26	3,600
J2215−0056	22:15:24.03	−00:56:43.8	2019-10-02	8,400
J2254+2327	22:54:38.33	23:27:14.5	2018-10-05	10,800
J2323−0100	23:23:26.17	−01:00:33.1	2019-10-02	7,800

Table 2.3: ERQ measurements of the Lyα halo luminosity and morphology. Area covered and size are shown as lower limits when extended halo is detected to the edge of the FOV. Lyα halo luminosities are measured from modified PSF subtraction, as referenced in Section 2.2.4.

ERQ Name	Area Covered (kpc^2)	Maximum Linear Size (kpc)	Halo Luminosity (erg/s)	Peak to Quasar Distance (kpc)	Centroid to Quasar Distance (kpc)	$e_{\rm weight}$	$e_{\rm unweight}$
J0006+1215[a]	6851	140	5.00e+43	3.44	5.56	0.44	0.69
J0220+0137[a]	>5693	>104	6.26e+43	5.04	9.59	0.35	0.66
J1145+5742[a]	>10529	>148	9.97e+43	2.31	17.09	0.74	0.71
J1232+0912	6016	119	5.40e+43	6.83	6.17	0.72	0.64
J1451+0132[a]	>9970	>148	2.29e+44	0.00	4.00	0.43	0.59
J1451+2338[a]	>11645	>157	3.80e+44	5.29	2.87	0.57	0.59
J1652+1728[a]	>8596	>128	2.14e+44	2.30	3.72	0.46	0.49
J1705+2736	>6703	>122	2.37e+43	4.81	23.15	0.91	0.78
J2215−0056	3812	114	9.78e+42	28.91	21.50	0.87	0.85
J2254+2327	2181	80	9.36e+42	8.18	8.41	0.65	0.67
J2323−0100	>3640	>137	3.08e+42	9.97	19.95	0.86	0.65
Median	>6702	>128	5.40e+43	5.04	6.50	0.65	0.66

Finally, after applying our selection criteria to our four nights we present a total sample of 12 ERQs, with redshifts $2.31 \leq z \leq 3.14$. Half of them have the narrow component in their Lyα emission. The median reddening of the sample is i–$W3 \approx 5.9$, Table 2.1 contains basic sample properties.

2.2.2 Observations

We observed our final sample of 11 ERQs using the Keck Cosmic Web Imager (KCWI, Morrissey et al. 2018), on the Keck II telescope. KCWI is a wide field, integral field spectrograph optimized for observing low-surface brightness targets. It provides both spatial and spectral information for resolved targets, allowing us to make pseudo-narrow-band images and obtaining spectra from individual spatial-pixels, or "spaxels."

Observations were conducted over four nights from 2018 to 2020, with identical instrument configuration across the sample. Observation details are noted in Table 2.1. Conditions during observation often varied through any night, but our work had typical seeing FWHM of about (0.8-1.4) arcseconds. KCWI currently has only a blue filter, and we used the BL grating, which has the best efficiency and widest wavelength bandpass ($\Delta\lambda \approx$ 2,000Å). KCWI uses a "slicer" to slice the field of view into rows or columns before going to the grating. Slicers come in three different sizes to optimize field of view, spectral resolution, and spatial sampling. We used the medium slicer to have considerable field of view, spectral resolution comparable to SDSS, and sufficient spatial sampling. This configuration yields a field of view of 15.7 arcsec $\times$ 18.9 arcsec, corresponding to a physical scale of approximately 128 kpc $\times$ 154 kpc at our sample's median redshift ($z_{em} \approx 2.61$). With 24 slices, the instrument configuration provides a spatial sampling of 0.68 arcsec, and seeing limited, along the slices. Each exposure was dithered 0.35 arcsec across slices to sub-sample the long

spatial dimension of the output spaxels, which have sizes of 0.68 arcsec × 0.29 arcsec. The spectral resolution is $R = 1800$. The full spectral range is approximately 3500 to 5625Å, which is ample for coverage of the Lyα emission profile across a wide range of quasar redshifts, $2.0 \leq z \leq 3.6$. We used exposures of 20 minutes, optimally integrating for 2 to 3 hours total, and varied depending on target availability, observing conditions, and priority of the object. We calibrated using arclamps and spectroscopic standard stars at the beginning and end of each night.

2.2.3 Data Reduction & Post Processing

We adopted the data reduction and post-processing approaches described in detail in L22. Here we only provide a summary of the major steps. We used the KCWI Data Extraction and Reduction Pipeline (KDERP, https://github.com/Keck-DataReductionPipelines/KcwiDRP) written in the Interactive Data Language (IDL) for flat-fielding, cosmic-ray removal, and for the first-pass instrument noise removal and background subtraction. We made sure that no prominent skyline residuals are present near Lyα in each spectrum. We then used CWITools (O'Sullivan et al. 2020), and the IDL library IFSFIT (Rupke & To 2021), for the second-pass background subtraction and removing internally scattered light. Specifically, IFSFIT uses a spatially-unresolved quasar emission template, generated from a one arcsecond aperture around the object, and is scaled to subtract all emission from the quasar at every spaxel position. A key step that was customized for half of the sample was the quasar template which is subtracted to leave only halo emission in the residual, described in Section 2.2.4. We also used CWITools' simplified algorithm to subtract any foreground continuum sources convolved with the point spread function.

2.2.4 Narrow Halo Emission

L22 confirmed that the narrow Lyα "spike" emission in ERQ spectra originates in the halo. In Section 2.3.1 we further confirm this in the rest of our ERQ sample. This insight into the emission's origin allows us to treat the emission differently in processing the spectra and images. For objects with no spike the PSF spectral template removes all emission within the seeing disk resulting in a hollow at the quasar position in the SB map, like in blue quasar studies.

We followed the procedure for generating quasar spectral templates as described in L22, and made customisations to the quasar template for each ERQ identified to have narrow Lyα emission. We isolated the feature within the one arcsecond template by interpolating underneath the narrow line, effectively "clipping" it, and left the extended emission in the residual. Without the modification to these templates, this approach to PSF subtraction will not leave behind the narrow/exteneded component in the residual. Examples of this template interpolation is shown in Figure 2.1 (see also L22, where a straight line was used to interpolate). In cases where the spectral location and profile shape of the spike was more ambiguous, we compared extracted spectra from gradually larger aperture sizes. We confirmed the spike was the only emission that increases with larger aperture size, and interpolated underneath its narrow profile.

2.2.5 Line Variability

We inspected ERQ spectra for variability between our KCWI observations and the BOSS catalog. This inspection was performed to rule out dramatic variability, and to rule out extreme transient models of the peculiar ERQ spectral properties. The median time between observations is two years at rest frame of the median ERQ. In general, characteristics of line profiles do not signifi-

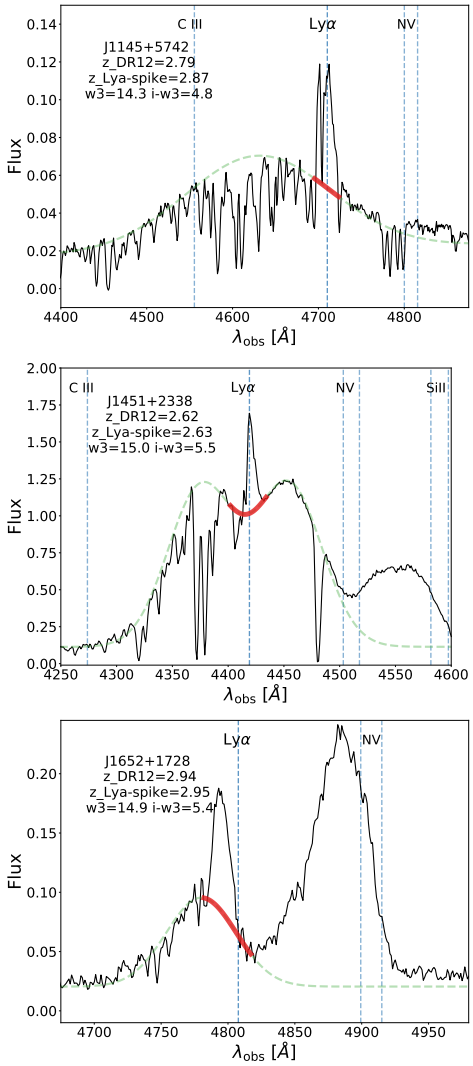

Figure 2.1: Example spectral templates extracted from an inner 1 arcsecond aperture spectra near Lyα of, from top to bottom, J1145+5742, J1451+2338, and J1652+1728. The unmodified spectrum is shown in black, the interpolation function is in dashed green, and the "clipped" narrow feature in the spectrum is replaced by the thick red line segment. All emission lines are labelled from the rest frame of the Lyα extended halo emission. Function fitting procedures would become convoluted by absorption in the Lyα forest, and so the interpolation function was hand-fit to account for smooth emission features and continuum on the red side of Lyα and deep absorption on the blue side. In the first panel, J1145+5742 has a straightforward and distinct separation between the broad and narrow emission components. The second panel shows J1451+2338, shown to have blended broad emission lines from Lyα and N v λ1240. The third panel of J1652+1728 also has unusual emission lines, and the blueshifted central emission of Lyα caused uncertainties in clipping the narrow emission. We do not assume this interpolation function describes any characteristics of the broad emission, but simply isolates the emission from the narrow component of Lyα.

cantly change between SDSS and our observations, less than about 35 per cent, and consistent with L22. Similarities between these observations indicate the unusual profile features that distinguish ERQs from typical quasars persist beyond two years in the quasar frame, and are consistent with other observations of ERQs from Hamann et al. (2017).

2.2.6 Sample Properties

Table 2.1 lists basic properties of the sample, measured redshift of the Lyα emission, and details of the observations. We include the SDSS BOSS catalog emission-line redshift measurements z_{em}, and $z_{\rm halo}$ computed from the extended Lyα halo emission centroid, without the quasar emission. We include C IV FWHM, measured from C IV λ1549 emission-line profile fitting done in Hamann et al. (2017), and when available [O III] λ5007 emission blueshift from Perrotta et al. (2019). We include catalog magnitudes and color ($W3$ and i–$W3$), and our computed bolometric luminosities ($L_{\rm bol}$). We apply galactic extinction corrections to all luminosity and SB measurements.

ERQs are heavily extincted in the visible and UV, but the amount of extinction is difficult to determine. In Hamann et al. (2017) it is estimated that the median SED is suppressed in ERQs by three magnitudes in the rest-frame UV, in comparison to normal blue quasars. Uncertain extinction in ERQs also makes bolometric luminosities difficult to determine. Therefore, we assume ERQs have intrinsic SEDs like typical blue quasars, and use their measured WISE $W3$ fluxes (assumed to be unaffected by extinction) to estimate the bolometric luminosities, similar to the ERQ luminosities computed by Perrotta et al. (2019).

We compare the medians quantities from our sample to medians from other surveys of blue quasars, discussion of these comparisons are in Section 2.3.4. One quasar, J0834+0159, was observed under cloudy conditions, and was omitted from analysis of Lyα halos. We do not have detection of other extended emission lines such as C IV λ1549 or He II λ1640 except for J0006+1215, which is discussed in L22.

2.2.7 Halo Detection

We used an optimal extraction algorithm for detecting diffuse emission in Lyα instead of pseudo narrowband images to obtain morphology and kinematics of the halo. This algorithm takes into account pixels of the three dimensional data cube, or "voxels," that are of good signal to noise (S/N > 2) and connected at sides, edges, or corners to each other. Our algorithm is described with more detail in L22, which followed algorithms in Borisova et al. (2016b); Arrigoni Battaia et al. (2019); Cai et al. (2019); Farina et al. (2019). Our surface brightness's 1σ limit, and root-mean-square value, are measured in a 1-arcsec aperture for a single 1-angstrom channel. Surface brightness maps probe the halo Lyα emission down to a median 1σ SB limit of 2.16×10^{-19} erg s^{-1} cm^{-2} arcsec^{-2}, across spatial scales from 40 kpc to >80 kpc from the quasars. Surface brightness root-mean-square has median of 2.26×10^{-19} erg s^{-1} cm^{-2} arcsec^{-2}, for a channel in rest-frame wavelengths between 1255 and 1275 Å, and where there are no prominent quasar emission lines.

2.3 Measurements & Results

To investigate the environment of ERQs, we measure basic properties of the Lyα halo emission, such as surface brightness, linear size, and velocity dispersion. Peculiarities in halo properties compared to blue quasars may be evidence ERQ inhabit a different quasar evolutionary phase.

Panels in Figure 2.2 show, from left to right, halo surface brightness, 1st velocity moment of the line flux distribution (i.e. velocity shift), velocity dispersion, circularly-averaged surface brightness (SB) radial profile, and spatially-integrated spectrum, for 11 of the 12 observed ERQs. J0834+0159 was observed under cloudy conditions, and is not included in the Figure 2.2 and subsequent tables. Tables 2 - 4 list a variety of properties measured from these maps.

2.3.1 Morphology & Brightness Maps

Morphology measurements such as extent and asymmetry may give insights into the gaseous environment of the quasar, and could be influenced by large scale structure, the presence of merger activity, and quasar luminosity.

Morphology of ERQ Lyα halos varies across the sample, with some halos extending to the edge of the FOV (> 60-70 kpc), and others compact near the central quasar (~40 kpc). These Lyα halos also show varying asymmetry. We present Lyα sB maps in the first column of Figure 2.2. One unique aspect of this project is showing continuous halo emission down to zero projected distance from the quasar, and thus the six ERQs with Lyα spikes do not show a hollow due to our quasar PSF subtraction (Section 2.2.4).

Table 2.3 presents the measured projected distance from the quasar to the Lyα halo emission peak, and to the halo centroid. The median distance from quasar to peak in our sample is $r_{\rm peak}$ = 5.0 kpc, and the median distance from quasar to halo centroid is $r_{\rm centroid}$ = 6.5 kpc. Uncertainty in these projected distances is about half a pixel in size, or ~1 kpc. The position of the Lyα halo centroid is used in analysis of spatial asymmetry in this section, and the position of the halo peak is used in analysis of aperture kinematics in Section 2.3.2.

Six of the halos extend beyond the FOV, and >55 kpc from the central quasar. Our sample has a median maximum linear size >128 kpc, and median halo luminosity 5.40×10^{43} erg s^{-1}.

We quantify the asymmetry level of the morphology of the Lyα halo with the elliptical eccentricity parameters $e_{\rm weight}$ and $e_{\rm unweight}$ (identical to L22). We define $e_{\rm weight}$ using flux-weighted second-order spatial moments with respect to the Lyα halo centroid, and follow the formula in O'Sullivan & Chen (2020). $e_{\rm unweight}$ uses flux-unweighted spatial moments with respect to the quasar position. Values of $e \approx 0$ correspond to circular morphologies, and values near 1 correspond to being more elliptical. Parameter $e_{\rm weight}$ is defined as $e_{\rm weight} = \sqrt{1 - \alpha^2_{\rm weight}}$, where the flux-weighted eccentricity parameter $\alpha_{\rm weight}$ is defined in Arrigoni Battaia et al. (2019) or Cai et al. (2019). $e_{\rm weight}$ tends to characterize central regions of the halo with high SB. Conversely, $e_{\rm unweight}$ is defined as $e_{\rm unweight} = \sqrt{1 - \alpha^2_{\rm unweight}}$, where the flux unweighted eccentricity parameter $\alpha_{\rm unweight}$ is defined in den Brok et al. (2020) or Mackenzie et al. (2021). $e_{\rm unweight}$ better describes the large-scale shape of the diffuse halo surrounding the quasar position.

Large differences between $e_{\rm weight}$ and $e_{\rm unweight}$ could indicate significant changes from inner halo to extended regions that could be affected by filamentary structures. For example, J1145+5742 has a luminous Lyα halo that extends East from the quasar position, and is visibly

asymmetric about the halo centroid, with a measured $e_{\rm weight} \approx 0.74$. Asymmetric extending of the halo away from the quasar position is also reflected in the large $e_{\rm unweight} \approx 0.71$. An unusual case is J2323−0100, which displays an asymmetric halo with a patch of emission to the North-West that causes the Lyα halo centroid to be offset. This offset away from the luminous bulk of halo emission results in a large $e_{\rm weight} \approx 0.86$. Considering the more diffuse mission around the quasar position, the asymmetry is more moderate, and thus has lower $e_{\rm unweight} \approx 0.65$. Median eccentricities for the optimally extracted halos (11 objects) are $e_{\rm weight} = 0.65$ and $e_{\rm unweight} = 0.66$. $e_{\rm unweight}$ values larger than $e_{\rm weight}$ could reflect the sample generally having a more circularly symmetric inner halo, where the flux is strongest, versus the slightly more asymmetric outer halo. These median eccentricity values are comparable to each other, but are given further context by comparing values to other quasar samples in Section 2.3.4.

To characterize the radial extent of the Lyα halo, we calculate the circularly averaged SB radial profiles for the ERQ sample (Figure 2.2, 4th column). While optimally extracted line maps yield measurements of morphology and kinematics, they do not allow direct comparison with other samples because other surveys used pseudo-narrowband imaging to compute their radial profiles. Therefore, we choose to generate a pseudo-narrowband image with fixed width to recover all possible fluxes in extended regions. Using a similar method to other studies, we adopt a fixed wavelength width of $\pm 1,000$ km s^{-1}centered at the Lyα rest wavelength. For the full sample of ERQs, the median SB in the innermost annulus (2−4 kpc) is 1.53×10^{-14} erg s^{-1} cm^{-2} arcsec^{-2}, and 1.61×10^{-16} erg s^{-1} cm^{-2} arcsec^{-2} in the most distant annulus (32−63 kpc). Six of the 11 ERQs which have modified PSF subtraction, due to the presence of a Lyα spike in their spectra, have an inner annulus (2−4 kpc) median SB 11.4×10^{-14} erg s^{-1} cm^{-2} arcsec^{-2}, and most distant annulus

(32−63 kpc) median SB 4.69 $\times 10^{-16}$ erg s^{-1} cm^{-2} arcsec^{-2}. We calculate the averaged SB at each radial distance measured by annuli centered on the quasar position for each ERQ, as well as the full sample median (Table 2.4). We compute a full sample SB median omitting the inner region data in order to compare these ERQ radial profiles with the spike to other samples, which cannot perform modified PSF subtraction. To demonstrate the potential difference between our quasars and other samples, we compute the median radial profile of the sub-sample of six ERQs, where a Lyα spike is present in the spectra and modified PSF subtraction was performed. SB of ERQs with detected Lyα emission increases monotonically as the radial distance decreases, indicating that the innermost regions are the most luminous part of these halo. ERQs with the Lyα spike emission demonstrate the most centrally concentrated emission.

We use an exponential fit to the binned radial profiles, $\mathrm{SB}_{\mathrm{Ly}\alpha}(r) = C_e \exp(-r/r_h)$, where C_e is the normalization, r is the projected distance from the quasar, and r_h the scale length of the profile. Figure 2.2 shows the fits of this model in the fourth column, and appear to reasonably describe the radial SB profile. For individual ERQs, a steep decline in SB near their inner regions (<4kpc) appear only for ERQs with quasar PSF subtraction that did not involve clipping the Lyα spike. Offset between the profile fit and data in the outer regions (>32kpc, eg. J1451+0132 and J1652+1728) are generally from ERQs with an asymmetric shape in the Lyα halo at large scales. These profiles are better fit by exponential functions than power laws, and show that SB steeply declines at large distances from the quasar. Table 2.4 presents averaged SB at each annular bin and exponential fit parameters. Our full sample median exponential scale length is $r_h = 9.4$ kpc, and the median of the six ERQ with a Lyα spike have $r_h = 8.7$ kpc. Generally, ERQ Lyα halos are more

centrally concentrated than blue quasar samples, and ERQs that have the Lyα spike are the most compact of our sample. Section 2.3.4 will have further discussion of quasar population comparisons.

2.3.2 Kinematics

Here we describe our kinematic measurements of the halos in our sample. Because of the multi-dimensional measurements of integral field spectroscopy, we can present the kinematics in both the integrated halo emission and spatially-resolved spectra.

Figure 2.2's fifth column shows the spatially integrated spectra and a single Gaussian fit to the Lyα halo emission. We define zero velocity by the emission centroid of the spatially-integrated halo, without clipping the narrow-emission spike from the spectral template. For the case of J2215−0056, we integrate the halo including the extended object to the north. Across the sample our integrated-halo emission spectra generally have similar narrow shapes, with a median spatially-integrated spectrum velocity dispersion of 293 km s^{-1}. J1145+5742 has narrow absorption that is blueshifted from the centroid in its Lyα halo spectrum. But in spite of the absorption, the fit centroid is consistent with the Lyα halo emission peak. For J1652+1728, the Gaussian fit captures the line width for approximating dispersion, but the narrow Lyα halo emission in the central region is blueshifted relative the outer halo, blueshifting the total spatially-integrated spectrum. This centrally concentrated blueshifting, which is seen in J1652+1728's 1st moment velocity map, is also seen in the Lyα emission profile from the central arcsec aperture in Figure 2.1 & 2.4. Blueshifted central emission causes uncertainties in what to clip as halo emission when subtracting the quasar.

Table 2.4: ERQ Lyα halo circularly averaged surface brightness radial profiles. The first five columns are data points for radial profiles in Figure 2.2. For modeling the radial profiles, the inner radius (2-4)kpc is not included when there is no inner halo clipped from the quasar PSF spectral-template, shown in parentheses. The last two columns are parameters from exponential-profiles fit to the radial profile data. Median-errors shown are the standard deviation of the values that compose the median.

ERQ Name	Radii Brightness (2-4) kpc (erg/s/cm^2/arcsec^2)	Radii Brightness (4-8) kpc (erg/s/cm^2/arcsec^2)	Radii Brightness (8-16) kpc (erg/s/cm^2/arcsec^2)	Radii Brightness (16-32) kpc (erg/s/cm^2/arcsec^2)	Radii Brightness (32-63) kpc (erg/s/cm^2/arcsec^2)
J0006+1215[a]	1.63e-14	1.22e-14	5.88e-15	1.48e-15	1.78e-16
J0220+0137[a]	1.43e-14	1.28e-14	7.68e-15	1.93e-15	−4.76e-17
J1145+5742[a]	2.16e-14	1.60e-14	7.09e-15	2.49e-15	7.98e-16
J1232+0912	(1.03e-15)	9.25e-15	6.75e-15	2.60e-15	1.61e-16
J1451+0132[a]	2.10e-13	8.23e-14	1.53e-14	3.85e-15	3.13e-16
J1451+2338[a]	8.46e-14	8.59e-14	4.01e-14	9.42e-15	1.22e-15
J1652+1728[a]	1.46e-13	7.26e-14	1.92e-14	4.96e-15	6.25e-16
J1705+2736	(6.69e-15)	2.39e-15	1.50e-15	7.85e-16	7.91e-17
J2215−0056	(1.23e-16)	1.33e-15	6.67e-16	4.69e-16	8.05e-17
J2254+2327	(3.15e-15)	7.91e-15	2.24e-15	5.39e-16	−2.10e-16
J2323−0100	(−1.59e-16)	4.14e-16	3.77e-16	1.28e-16	−2.48e-17
Median	1.53e-14	1.22e-14	6.75e-15	1.93e-15	1.61e-16

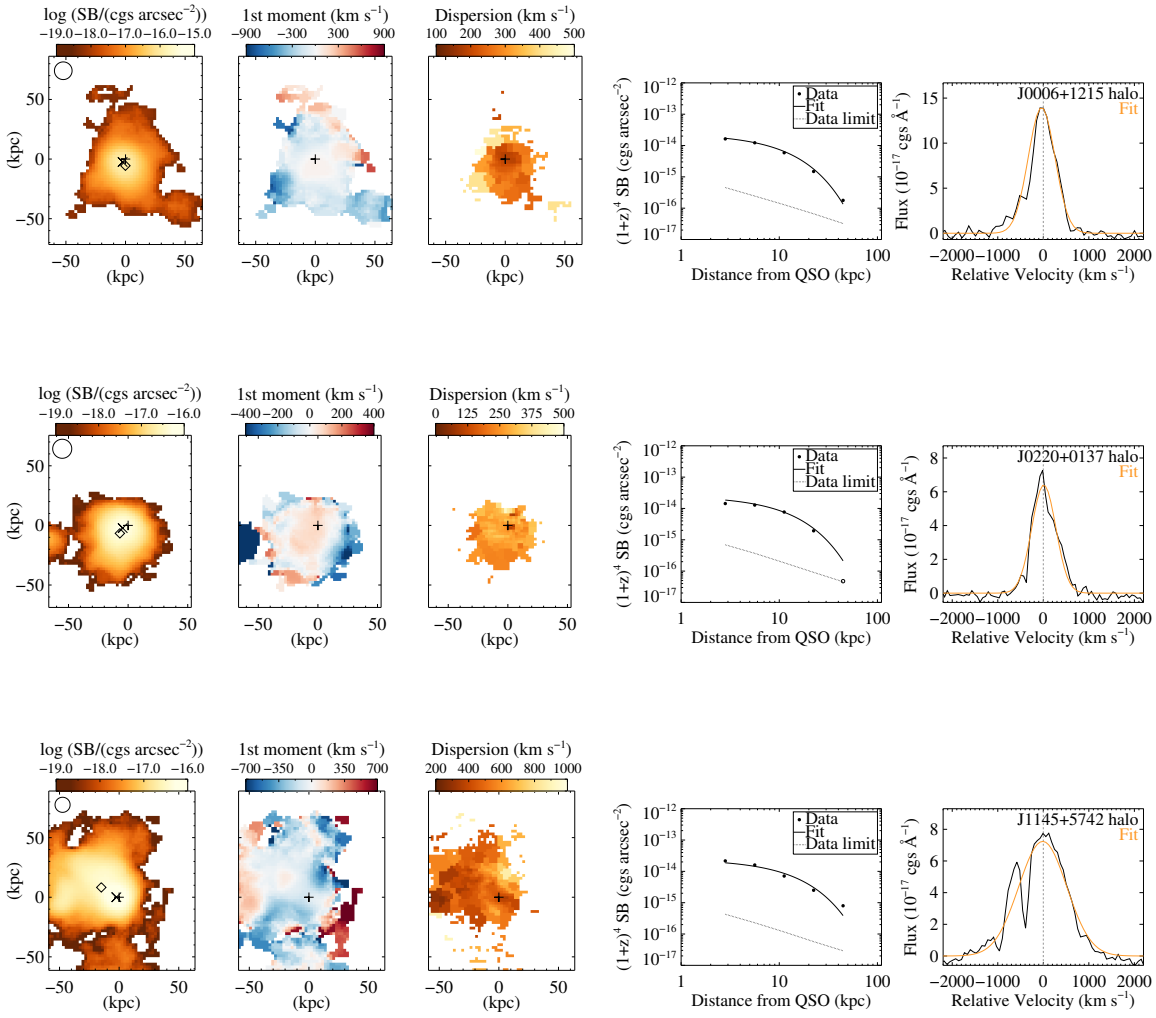

Figure 2.2: Full sample of ERQ Lyα halos after subtracting the quasar, and the best available measurements, where the Lyα spike was isolated in six quasar spectra before subtraction. First column shows the optimally extracted halo, second is the 1st moment halo velocity map, third is Voronoi binned velocity dispersion, fourth is the circularly averaged surface brightness radial profile, and the fifth is the total integrated Lyα halo spectrum. For all 2D maps, the plus is the location of the quasar. For the surface brightness panels the PSF size is indicated as a circle in the upper left corner, the diamond is the centroid of halo emission, the cross symbol is the location of peak Lyα halo emission when the Lyα spike is left in the residual map. For the surface brightness radial profiles hollow circles represent negative values that were included for profile fitting, and plotted as absolute values. They have also been corrected for cosmological dimming for comparison to other samples. The integrated halo spectrum shows a Gaussian that was fit to determine the overall halo velocity dispersion. Zero velocity is defined as the centroid of integrated halo emission, without removing the Lyα spike in quasar subtraction. J0220+0137 has a cloud in the eastern edge of the FOV which is likely a foreground source not physically related to the quasar, and is omitted in measuring Lyα halo emission.

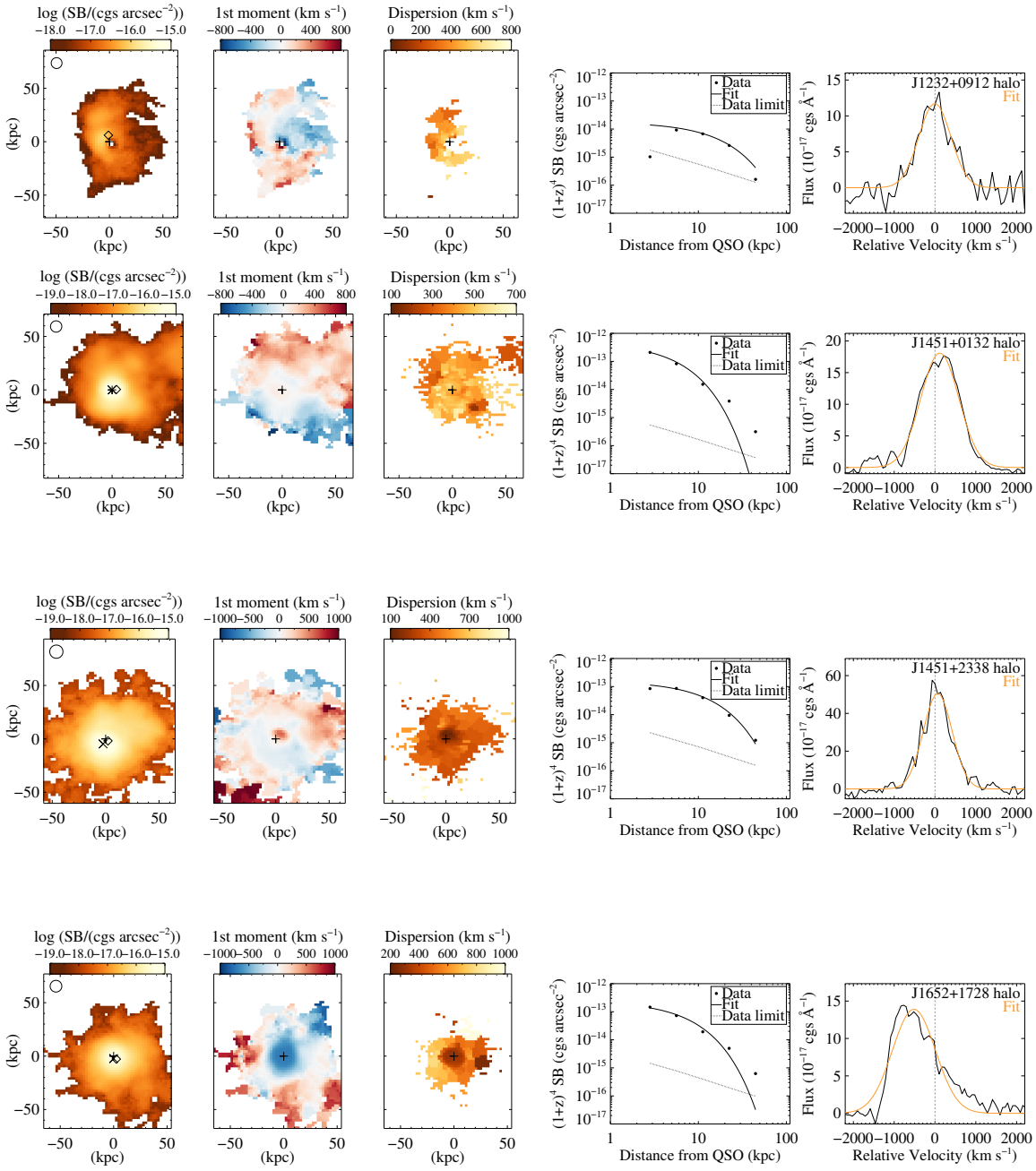

Figure 2.2: *continued.* J1652+1728's integrated halo centroid is offset from zero velocity because we define zero from the outer halo.

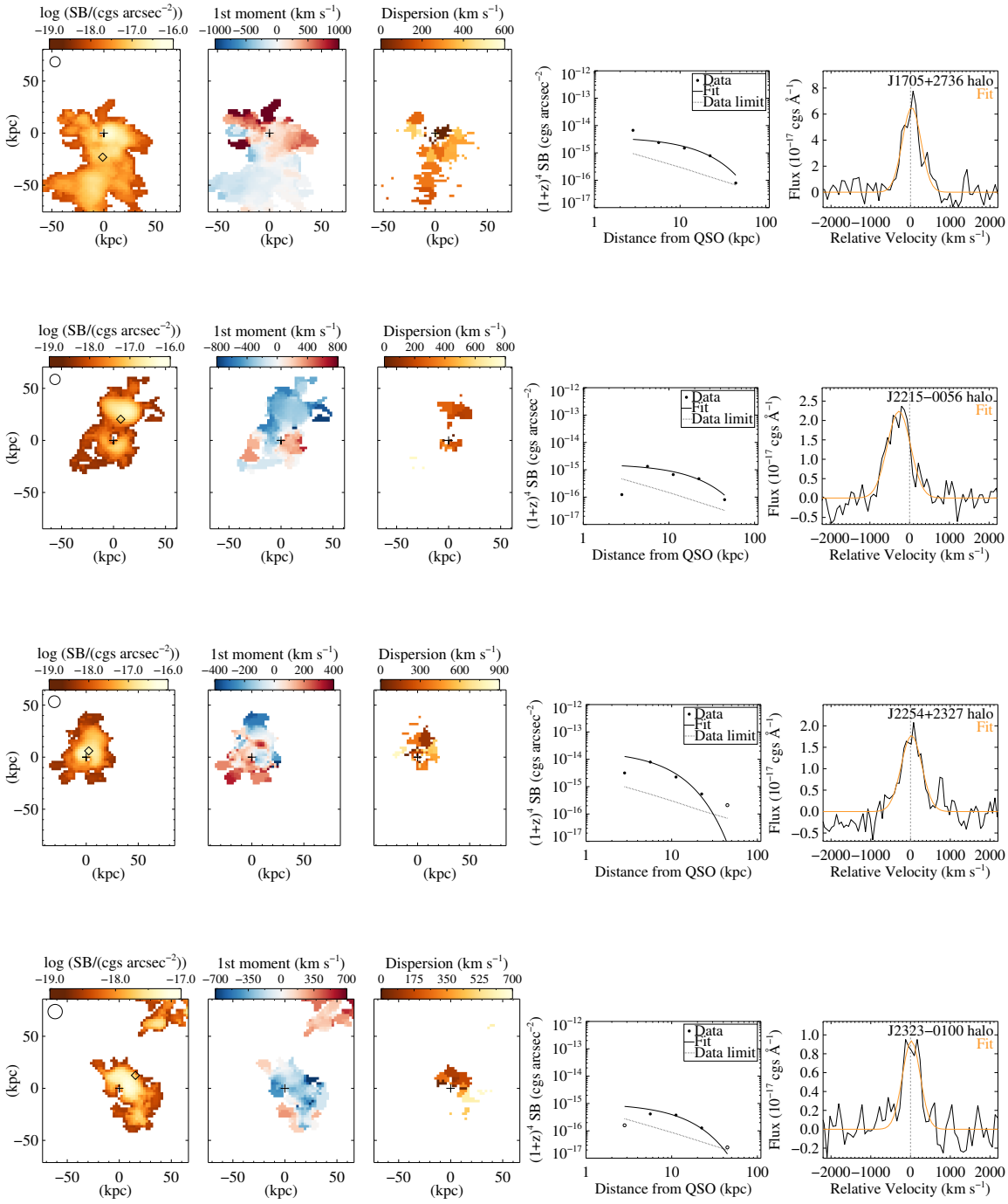

Figure 2.2: *continued.* J2215−0056 has a cloud in the north of the quasar which appears to be associated with the quasar as part of the same large scale structure, and blueshifts the spatially-integrated halo spectra. The associated object is omitted in measuring the ERQ's total Lyα halo emission.

Table 2.5: Lyα halo radial profile fit parameters from exponential-profile fit to the data. Median-errors shown are the standard deviation of the values that compose the median.

ERQ Name	Exponential Amplitude (erg/s/cm^2/arcsec^2)	Exponential Scale Length (kpc)
J0006+1215[a]	(2.36 ± 0.04)e-14	8.6 ± 0.1
J0220+0137[a]	(2.50 ± 0.05)e-14	9.4 ± 0.1
J1145+5742[a]	(2.43 ± 0.02)e-14	10.8 ± 0.1
J1232+0912	(1.77 ± 0.11)e-14	11.9 ± 0.5
J1451+0132[a]	(4.68 ± 0.02)e-13	3.51 ± 0.01
J1451+2338[a]	(1.57 ± 0.02)e-13	8.7 ± 0.1
J1652+1728[a]	(2.41 ± 0.03)e-13	5.01 ± 0.04
J1705+2736	(3.82 ± 0.52)e-15	13.9 ± 1.3
J2215−0056	(1.64 ± 0.17)e-15	16.9 ± 1.4
J2254+2327	(2.07 ± 0.22)e-14	5.7 ± 0.3
J2323−0100	(1.02 ± 0.19)e-15	10.5 ± 1.4
Median	(2.36 ± 0.14)e-14	9.4 ± 3.7

Table 2.6's fifth column shows the resulting velocity dispersion from a Gaussian fit to the integrated halo emission.

Figure 2.3 displays evidence of an extended Lyα emitter (LAE) whose emission centroid coincides with absorption in the quasar spectrum. The centroid of the LAE is ~30 kpc projected distance from the halo peak, and spectroscopically < -500 km s^{-1}from the redshift measured by the Lyα halo. At higher redshifts ($3 < z < 4.5$) LAEs with similar velocity offset and clustering are suggested to be star-forming galaxies orbiting in the quasar halo potential (Fossati et al. 2021). It is uncertain if the extended emitter is powered by quasar radiation.

We describe kinematics at each spatial position around the quasar in 2D maps. Figure 2.2's second column shows velocity centroid maps, which are the 1st-moments in velocity space of the flux distribution at each spatial position. Our velocity maps use the same detection region and PSF from the SB maps. We measured relatively low velocity shifts of the halos, at hundreds of km s^{-1}, and do not exhibit energetic outflows of thousands of km s^{-1}.

Table 2.6: Halo kinematics measured from several methods from different columns in Figure 2.2. Measurements in the first column refers to the standard deviation of the 1st velocity-moments, computed from the emission line flux distribution at each spaxel. The second and third column refer to dispersion as computed by a single Gaussian fit to each Voronoi-bin in the velocity dispersion map. 2nd velocity-moments are not computed because there is not enough signal to reliably compute higher velocity-moments. The final column shows results from fitting a single Gaussian to the total integrated halo.

ERQ Name	Spatial Standard Deviation of Velocity Centroid (km s^{-1})	Spatial Median of Velocity Dispersion (km s^{-1})	Spatial Standard Deviation of Velocity Dispersion (km s^{-1})	Spatially-Integrated Velocity Dispersion (km s^{-1})
J0006+1215[a]	238	275	73	293
J0220+0137[a]	456	259	44	264
J1145+5742[a]	288	491	124	526
J1232+0912	231	424	114	393
J1451+0132[a]	264	420	82	467
J1451+2338[a]	331	401	112	354
J1652+1728[a]	393	542	194	526
J1705+2736	424	251	108	235
J2215−0056	301	220	122	292
J2254+2327	195	374	216	261
J2323−0100	280	266	201	225
Median	288	374	114	293

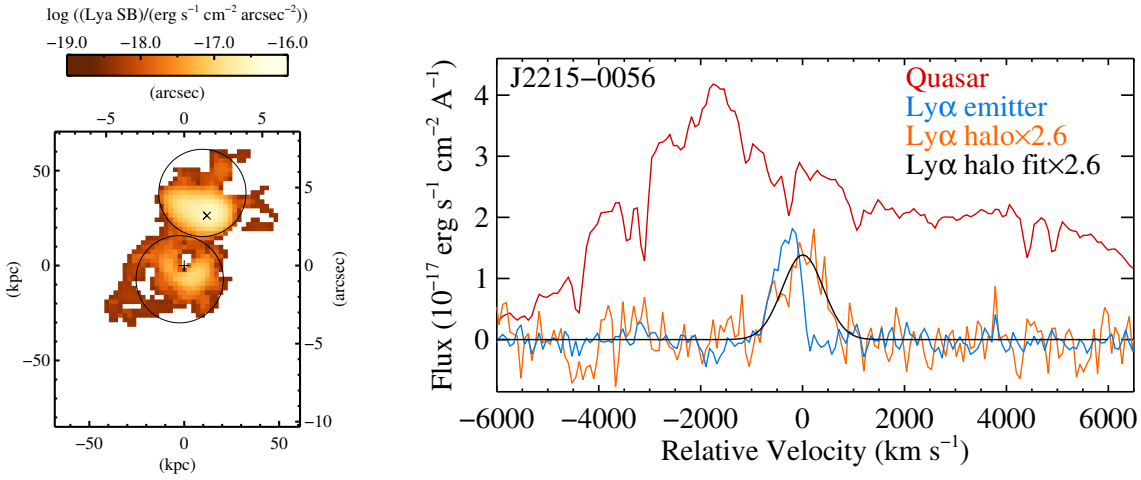

Figure 2.3: Aperture spectra of J2215−0056's halo and the associated Lyα emitter (LAE). The left panel displays the same SB map from Fig. 2.2, over-plotted with the apertures used to generate emission spectra. The plus symbol is the location of the quasar, and the cross symbol is the location of peak brightness for the LAE. The aperture used to extract the halo emission includes the quasar position, but is offset to avoid the LAE. The second aperture above the quasar is used to generate the LAE spectrum. The right panel is the quasar spectra for J2215−0056, the extracted aperture spectra from the left panel, and a singe Gaussian fit to the halo emission. In black is J2215−0056's quasar spectrum, generated using a 1 arcsecond aperture from the non-PSF subtracted data, blue is the LAE emission, orange is the aperture spectrum of Lyα halo emission, and black is a Gaussian fit to the halo emission. Lyα halo emission is scaled with a constant for visualization and comparison to the other spectra. There is sharp and narrow absorption in the quasar spectrum that visibly aligns with the LAE spectrum centroid. Our extracted halo emission may also display absorption at the same spectral location. There is no strong emission detected near the boundary of these emitters, nor is there a smooth and continuous transition from the halo emission profile to the LAE profile, to suggest there is a luminous arm directly connecting the objects.

Table 2.6 lists the spatial velocity-centroid standard deviation for each ERQ, other computed quantities of velocity dispersion, and their median. The first column is the standard deviation of the 1st velocity-moment centroid, with a sample median of 288 km s^{-1}. Second is the median velocity dispersion for each object, from the Voronoi-binned velocity dispersion maps in Figure 2.2, and their respective standard deviation in the third column. Our sample median of the spatial velocity dispersion and its standard deviation are 374 and 114 km s^{-1}respectively. Finally we show the dispersion of the Gaussian-fit to the spatially integrated Lyα halo emission, with a median of 293 km s^{-1}. Discussion and analysis of these quantities is in Section 2.4.5.

Our data do not have sufficient signal-to-noise ratios to measure halo velocity dispersion using second velocity moments (see L22 for more discussion). We instead use Gaussian fits to a Voronoi-binned map (see Rupke et al. (2019)). Figure 2.2's third column shows the final Lyα Gaussian velocity dispersion maps. These maps are generally smaller than the other maps of SB and velocity shift, but as an independent detection method they confirm the general morphology of the extended halo. In the case of J2215−0056, the northern emitting region has unusually uniform dispersion across its area, unlike any other extended emission cloud we detect. It is not clear if this Lyα emitter is a distinct object. For J2215−0056 we determine the systemic redshift by extracting the extended halo excluding the extended object. The remaining ERQ Lyα halos show relatively low dispersion across their maps, in the hundreds of km s^{-1}.

Some ERQs show a velocity gradient from one edge of the halo to the other of ∼1,000 km s^{-1} (e.g., J1232+0912 and J1451+0132), and the coherent transition from redshift to blueshift helps confirm the measured velocities are valid. A rotating disc of ∼100 kpc size is not expected to have formed by $z \sim 2$ (e.g., DeFelippis et al. 2020; Huscher et al. 2021). One ERQ, J0220+0137, has

a kinematically distinct cloud at the eastern boundary of the FOV, ~65 kpc from the quasar, and shifted in velocity space about −1,500 km s^{-1}from the Lyα halo redshift. The kinematic separation makes it unlikely to be of the quasar halo diffuse gas, and it is omitted in measuring the Lyα halo emission. ERQs J1451+2338 and J1652+1728 have a noticeable circular patch at the center of their 1st velocity-moment map, and are likely the residual from imperfect quasar subtraction caused by complexities in their Lyα profile.

2.3.3 Blueshifted Absorption

Figure 2.4 shows aperture and annular spectra of selected ERQs, to further understand the spatial and spectral distribution of Lyα emission and absorption features. One ERQ shows definite blueshifted absorption, J1145+5742, similar to what was found in J0006+1215, by L22. J1145+5742 has strong absorption features in its integrated spectra, and consistently shows deep and narrow absorption in apertures across the FOV, out to ~50 kpc, blueshifted at −400 km s^{-1}. In its inner halo spectrum, only within ~25 kpc, there is blueshifted absorption at about −950 km s^{-1}. J1451+0132 has blueshifted absorption in its emission profile of the innermost and spatially unresolved inner halo, at ~800 km s^{-1}and ~1250 km s^{-1}, but not in the outer halo profile. These blueshifted absorption features resemble those of spatially resolved Lyα halo spectra that require outflows (e.g., Li et al. 2020).

J1652+2736 has more unique profile features. It has primarily blueshifted central halo emission from apertures within 15−20 kpc of the quasar (about −900 km s^{-1}), and has gradually redshifted and more symmetric Lyα halo emission at larger annular radii. Its aperture spectra reveal that the asymmetric emission profile in the integrated Lyα halo is not from blueshifted absorption, but from the central halo emission being blueshifted, relative to the extended halo.

Our data show evidence of multi-component emission, and likely also affected by absorption. Overall, we do not find evidence for strong absorption in the Lyα halo emission profiles. The intrinsic emission profile of Lyα is not known for these quasars in order to model the level of absorption (e.g., Wang et al. 2021), and analysis of the environment which may cause absorption is beyond the scope of this work.

2.3.4 Comparisons to Blue Quasars

We have a full sample of eleven ERQ Lyα halos. One of the main goals of our study is to compare the Lyα halos around ERQs to Type-I blue quasars roughly matched to the ERQs in redshift and luminosity ($\geq 10^{47}$ ergs s^{-1}, at cosmic noon). Our focus is on Type-I quasars, but we also include Type-IIs for some of the comparisons, as described below. Our median ERQ luminosity of $L_{\rm bol} = 5 \times 10^{47}$erg s^{-1} and $z = 2.61$ is only slightly more luminous than other samples we compare. We use the same method described in Section 2.2.6 to recalculate all of the blue quasar sample luminosities for consistency. Combining the four blue quasar samples, they have a range of medians $L_{\rm bol} \approx 1.0 - 4.0 \times 10^{47}$erg s^{-1} and $z \approx 2.3 - 3.2$, totaling 108 quasars (Cai et al. 2019; Arrigoni Battaia et al. 2019; Borisova et al. 2016a; Mackenzie et al. 2021).

We recalculate all of the blue quasar sample luminosities in the same way as ERQs, using W3 photometry to estimate bolometric luminosities (see Section 2.2.6).

Our comparison samples are the following. We take the quasar sample from Cai et al. (2019), consisting of 16 blue quasars of median $z = 2.3$, and $L_{\rm bol} = 10^{47.2}$erg s^{-1}. We take the 61 blue quasars from Arrigoni Battaia et al. (2019), with median $z = 3.2$ and $L_{\rm bol} = 10^{47.4}$erg s^{-1}. Borisova et al. (2016a) sample consists of 19 luminous blue quasars of median $z = 3.2$ and median bolometric

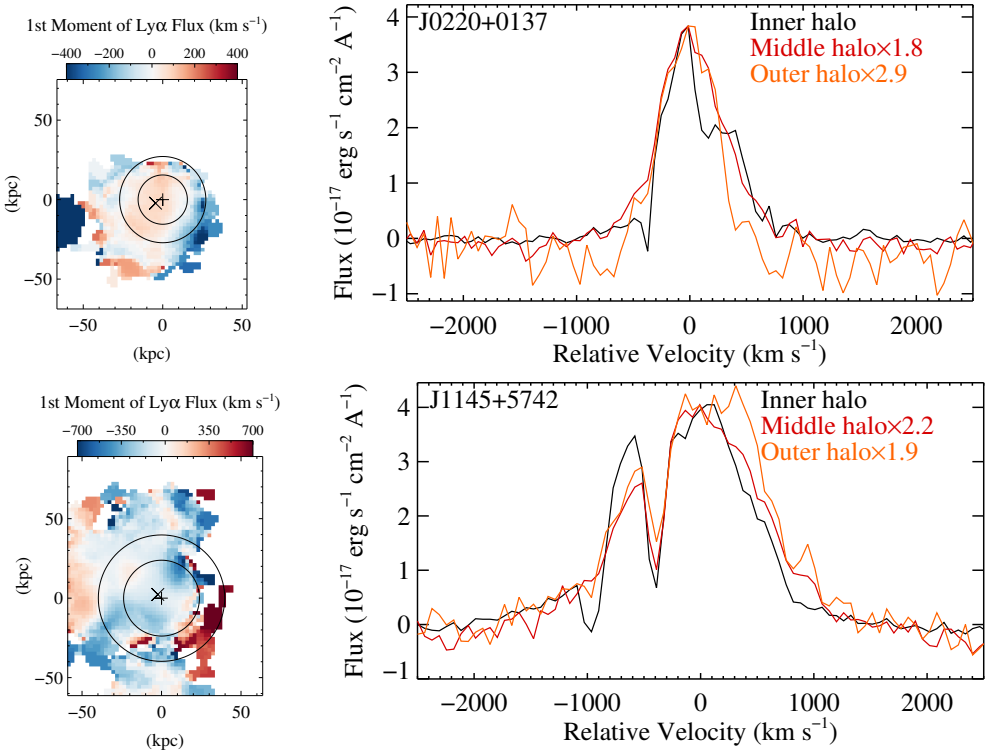

Figure 2.4: Aperture spectra of Lyα halo emission for J0220+0137 and J1145+5742. The left column displays the same 1st moment velocity map from Fig. 2.2, over-plotted with the apertures used to generate Lyα emission spectra. The plus symbol is the location of the quasar, and the cross symbol is the peak of the Lyα halo emission. For J0220+0137 & J1145+5742, circular aperture boundaries are drawn to define three regions, one innermost region, a middle transition region, and an outer halo region, which includes all emission outside the circular apertures. J0220+0132 is an example of a complex profile that is revealed after it's divided into apertures, instead of the smoothed emission features in 's integrated halo spectra. A flat emission spectrum between 100-400 km s^{-1}is seen in the innermost halo ($\leq$~20 kpc), perhaps by a combination of multi-component gas kinematics and/or absorption, and is otherwise lost in the total integrated halo spectrum shown in Fig. 2.2. J1145+5742 displays strong absorption at −400 km s^{-1}across the ~120 kpc span of the halo, and weaker absorption at −950 km s^{-1}across $\leq$~50 kpc. Lyα's emission profile shape remains consistent across the ~120 kpc span of the halo.

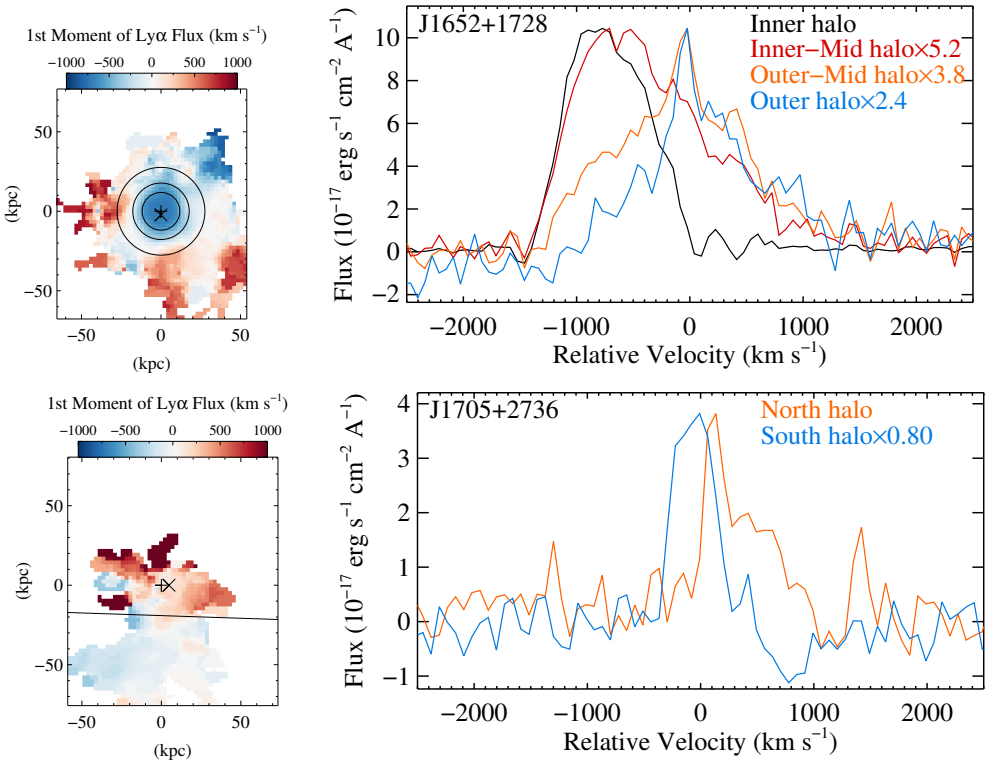

Figure 2.4: *continued.* Aperture spectra of Lyα halo emission for J1652+1728, and J1705+2736. J1652+1728 has an additional subdivision to show a quiescent circular region of the middle halo (~20 kpc), which lacks clumpy inflows/outflows. For J1705+2736, the halo is bisected into a northern and southern region for analysis. The right panel is the corresponding quasar's Lyα emission spectra from each halo region, and each spectra is scaled with a constant for visualization and comparison to the other regions' emission profile. J1652+1728's Lyα emission profile displays a rapid transition beyond ~20 kpc from the quasar, and becomes sharper peaked and symmetrically broader at its base. This symmetric broadening is likely from the patches of red and blueshifted clumps in the outer regions of the velocity map. The inner halo region's peak emission is blueshifted to ~900 km s^{-1}, and displays absorption at the redshift of the peak outer-halo emission. J1705+2736 shows moderate blueshifting in the southern lobe of the Lyα halo, and becomes more narrow. The northern halo emission profile may be asymmetrically broadened on the red side by redshifted clumps at the outer boundary of the halo.

luminosity $10^{47.6}$ erg s^{-1}. Mackenzie et al. (2021) have 12 blue quasars of median $z = 3.2$, and are on the fainter side of these samples, with median $L_{\rm bol} = 10^{47.0}$erg s^{-1}. den Brok et al. (2020) sample consists of four Type-II quasars of median $z = 3.4$ and median $L_{\rm bol} = 10^{46.7}$erg s^{-1}. We verify that the intrinsic bolometric luminosities estimated based on mid-IR luminosities are similar to those estimated with X-ray luminosities, and the correction factors modeled in Shen et al. (2020). A final Type-II quasar from Sanderson et al. (2021) is at $z = 3.2$, which is a mid-IR-only source not detected in the optical.

Figure 2.5 shows the relationship between the halo luminosity and the bolometric luminosity of the quasar. In order to make these comparisons, we verified that masking or not masking the inner 1-arcsecond yields similar halo luminosities, within about 10 per cent of the total halo luminosity. We also assessed changes in computed halo luminosity with or without Lyα spike clipping. Four of six ERQs with a spike showed an increase in computed halo luminosity of 20−40 percent. Halo luminosities of J1451+0132 & J1652+1728 more than doubled, each increasing by factors of ∼2.25. When subtracting the emission of the quasar, the shape of the spectral template that is subtracted is important for determining the residual halo emission. Halo emission is not as distinct in typical blue quasar spectra, and does not change the spectral template shape (ref. Sections 2.2.3 & 2.2.4, and Figure 2.1). Most of ERQ Lyα halo emission is concentrated in the inner halo regions near the quasar PSF, so modifications to the spike are more important for ERQ Lyα halo luminosity.

L22 took extensive care in choosing these blue quasar samples for comparing halo measurements to ERQs (see Section 3.5.1 in L22). All surveys considered were performed using 8-10 meter class telescopes. Parameters most affected by data sensitivity are size and asymmetry, which is why we use two measurements for quantifying asymmetry (see Section 2.4.6). It was noted in Arrigoni Battaia et al. (2019) that the size of blue quasar nebulae did not increase significantly with longer exposure time.

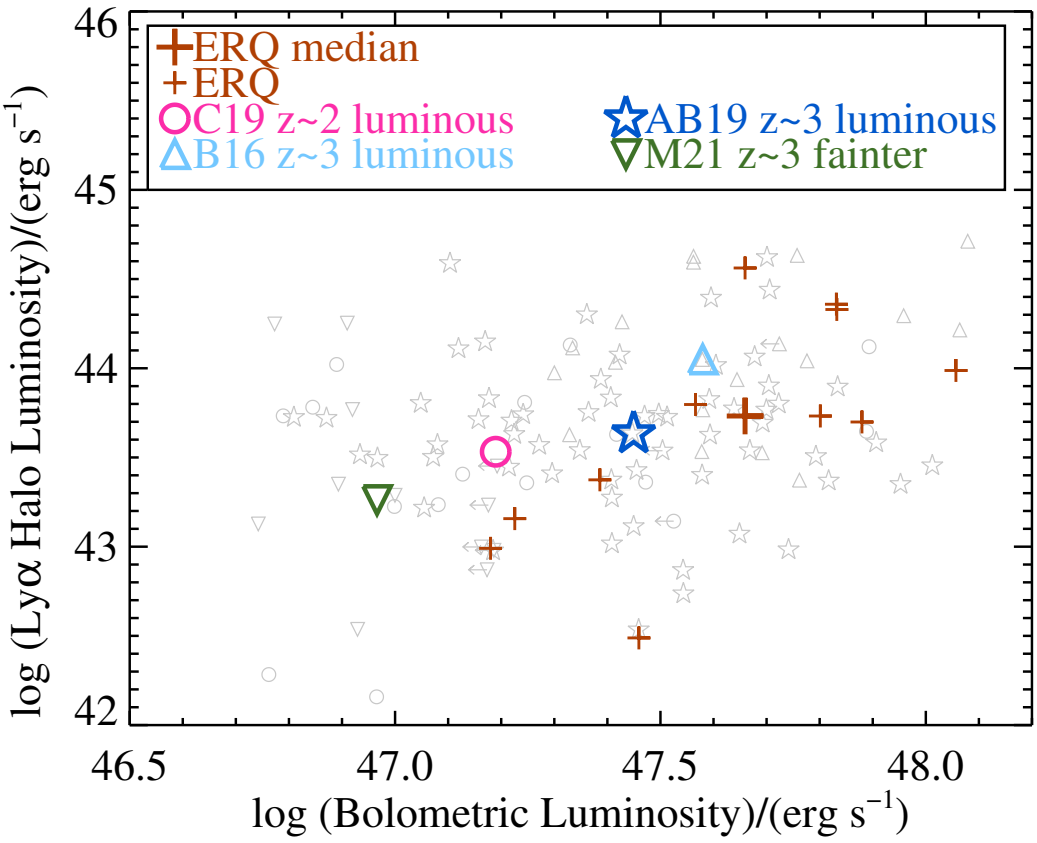

Figure 2.5: Computed logarithmic bolometric luminosity vs logarithmic Lyα halo luminosity of various literature samples and our ERQs. Upper and lower limits are shown with arrows. Brown pluses are the individual ERQs, and the large brown plus is the median of our sample. Blue quasar samples have median values shown as the large pink circle, dark blue star, light blue triangle, and the dark green downward triangle symbol. Individual quasars from other samples shown as small gray symbols matching their median symbol. There is significant overlap of individual quasars in our sample and luminous blue quasar samples. The median of these samples shows a positive luminosity trend for bolometric luminosity and Lyα halo luminosity across all samples.

Our ERQ median is $L_{\rm halo} = 5.40 \times 10^{43}$ergs s^{-1}, where the luminous blue quasar populations have medians in the range $L_{\rm halo} \approx 5-10\times10^{43}$ergs s^{-1}. L22 noted that the Lyα halo luminosity around the reddest quasar in our sample, J0006+1215, is roughly three times lower than expected from the matched blue quasar samples. In our larger sample, the second reddest ERQ, J2323−0100, stands out for having the lowest halo luminosity, roughly 10 times lower than expected from the blue quasars (see Table 2.3 and Fig. 2.5). However, the full range of ERQ halo luminosities in our study falls within the range of those for blue quasars. We also find that the ERQs follow a weak trend for larger halo luminosity around quasars with larger bolometric luminosity that was noted previously in blue quasars by Mackenzie et al. (2021).

Figure 2.6 shows the maximum linear size vs bolometric luminosity. Many of the ERQs are shown with only lower limits on their maximum halo size, because they exceed the field of view of KCWI (see also Table 2.3 and Section 2.3.1). We compare samples from Borisova et al. (2016a), Arrigoni Battaia et al. (2019), Cai et al. (2019), and Mackenzie et al. (2021). For Arrigoni Battaia et al. (2019) we estimate a maximum linear size for each quasar from the sum of maximal radial extent for the halo plus $\sqrt{(\text{covered area})/\pi}$. We report the maximum linear size as lower limits when the halo SB map extends to the edge of the FOV. Similarly to the luminosity trend, ERQs populate the high-luminosity region of a positive trend with the maximum linear size of Lyα halos and bolometric luminosities.

Figure 2.7 shows the surface brightness radial profile of ERQs pseudo-narrowband images, the median radial profiles of ERQs and several blue quasar samples, and the median exponential scale length of each quasar sample. Each point on the radial curve shows the average SB of an annulus centered on the quasar. Table 2.4 presents the data for our sample. An important feature we

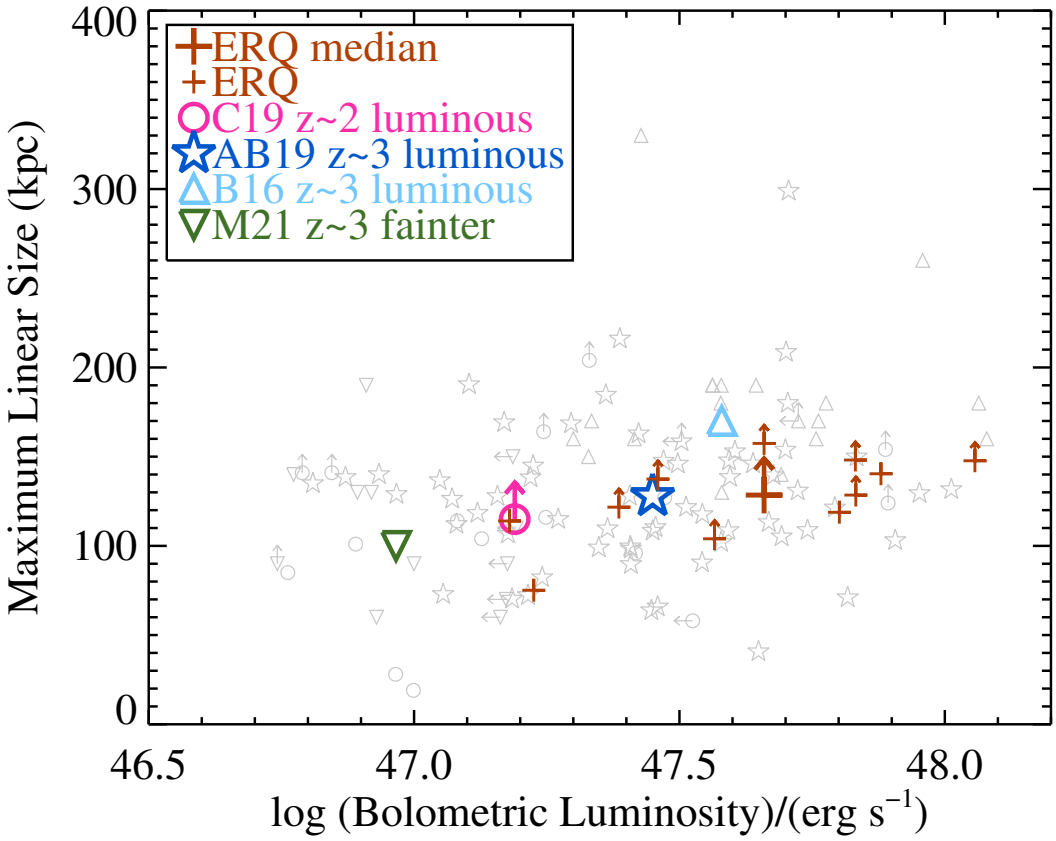

Figure 2.6: Computed logarithmic bolometric luminosity vs maximum linear size of the halo, using identical color and symbol legend as Figure 2.5. Lower limits are shown for medians computed from samples that contain halos extending to the edge of the field of view. There is overlap of individual quasars with other samples, and a weak positive luminosity trend can be seen across the medians of the samples.

take advantage of is that obscuration behaves as a coronagraph, and allows probing of the inner-most regions of the halo. Six ERQs have had their quasar emission subtracted without the Lyα spike, and we measure their SB at smaller projected distances from the quasar than the blue quasar samples. For comparison, we take the median SB radial profile from Borisova et al. (2016a), Arrigoni Battaia et al. (2019), and Cai et al. (2019). The Borisova et al. (2016a) radial profile is obtained from Marino et al. (2019). All samples have comparable size of the point-spread function corresponding to a FWHM of 1.4 arcsec or 12 kpc. For our ERQ sample we present two median radial profiles. One median is for ERQs which can probe to zero projected distance, and the other is omitting the central 1-arcsecond region (~4 kpc radius), for comparison to other quasar studies that do not have the Lyα spike.

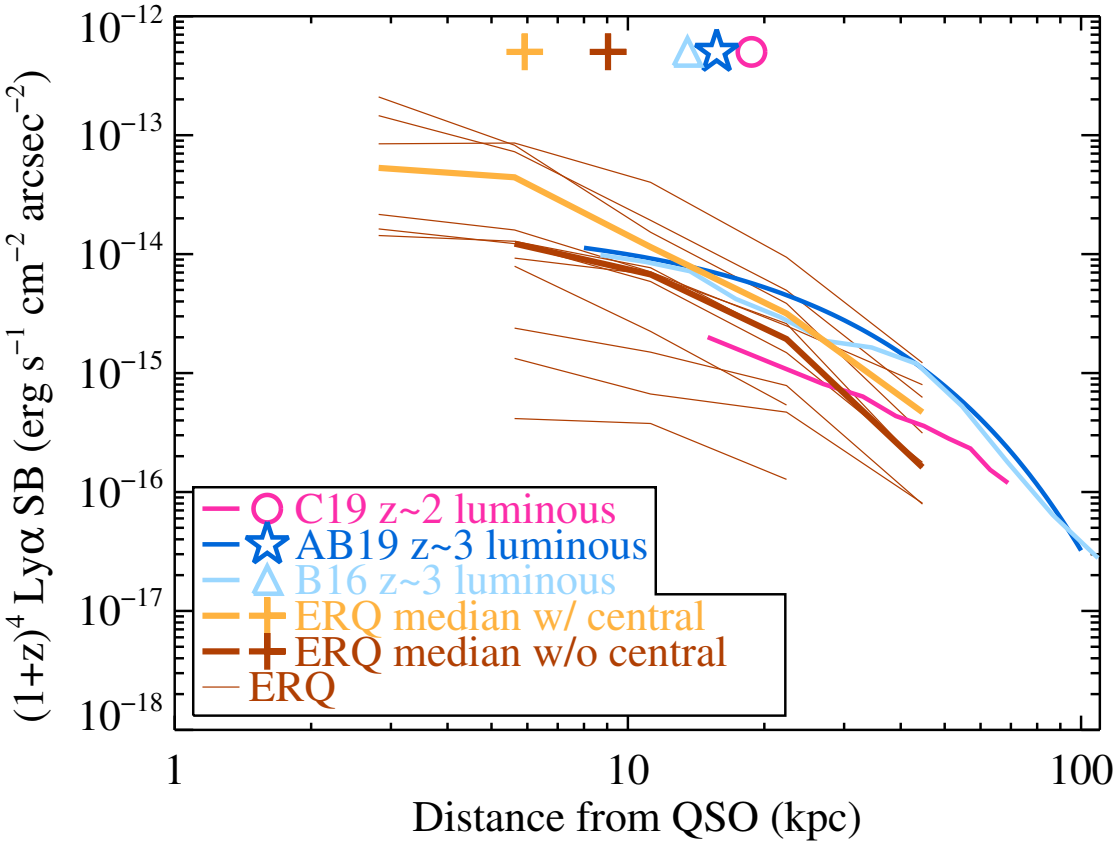

Figure 2.7: Circularly averaged surface brightness radial profiles of our sample of ERQs in comparison with other samples of blue quasars at comparable redshift and luminosity. The bold brown line is the ERQ sample median at each surface brightness bin for which there is detected halo emission. Thin brown lines are the individual ERQs. Other colors correspond to the other samples of blue quasars, pink, blue, and light blue for Cai et al. (2019), Arrigoni Battaia et al. (2019), and Borisova et al. (2016b), respectively. Across the top of the figure shows the exponential scale lengths, color coded to match each sample. Notice that the scale lengths of ERQs are shorter than blue quasar samples, and thus have profiles that fall off more rapidly at large distances. Also notice that ERQs with higher surface brightness tend to have detectable Lyα-spike halo emission down to the central projected radius from the quasar. Negative values of surface brightness from Fig. 2.2 are not shown in this figure. All surface brightnesses are corrected for cosmological dimming.

Along the top of Figure 2.7 we also present the exponential scale length fit to the median radial profiles. We fit an exponential function defined in Section 2.3.1 to the median SB radial profile, and record fit values in Table 2.4. Exponential scale length probes the brighter inner halo region, in contrast to the maximum linear size which depends on more diffuse low-SB emission. Our full sample's median radial profile, omitting the innermost bin (0−4 kpc) for comparison with blue quasar samples, has a scale lenth r_h = 9.0 kpc. Median profile scale lengths for other blue quasar samples are 13.5, 15.7, and 18.7 kpc for Borisova et al. (2016a), Arrigoni Battaia et al. (2019), and Cai et al. (2019), respectively. For ERQs with a Lyα spike we can probe deeper to the inner halo regions, at projected distance 0−4 kpc, because of modified PSF subtraction (ref. Sections 2.2.3 & 2.2.4). Considering only the ERQs with a Lyα spike, we can compute a scale length of their median profile r_h = 5.9 kpc. ERQs are generally more luminous than blue quasars, and there should be a natural tendency for more luminous quasars to have larger halos, as everything scales with higher luminosity. Despite this intuitive tendency, ERQ Lyα halos are characteristically more compact in their inner regions than those of luminous blue quasars.

Figure 2.8 compares ERQ Lyα halo spatially-integrated velocity dispersion vs bolometric luminosity with those from blue quasars which have measured spatially integrated velocity dispersion in the literature. We did not have enough signal to compute 2nd-moment velocity dispersions for the halo maps. Our ERQ velocity dispersions for direct comparison are computed from the Gaussian fits to the total integrated halo spectrum, shown in the last column of Figure 2.2, and are tabulated in the last column of Table 2.6. Other samples compute a 2nd-moment velocity dispersion, but Cai et al. (2019) also reports a velocity dispersion from spatially integrated velocity dispersion for the integrated halo spectrum, which we can directly compare. Line fitting of the integrated spectrum

is a more robust dispersion measurement than moment maps (see discussion in O'Sullivan et al. (2020)). Our ERQ sample's median integrated Lyα halo dispersion is 293 km s^{-1}. Cai et al. (2019) measured their sample median of 269 km s^{-1}. We see the halo velocity dispersion of ERQs follow the distribution of the luminous blue quasars of Cai et al. (2019). Both distributions generally follow a trend for larger dispersion in more luminous quasars.

Finally, Figure 2.9 presents morphology of halos vs bolometric luminosity, with two different eccentricity parameters. Different surveys used different parameters to characterize morphology for their population. We present ERQs with both of these parameters computed to compare with as many as possible. We take $e_{\rm unweight}$ values from, Borisova et al. (2016a), den Brok et al. (2020), Mackenzie et al. (2021), and Sanderson et al. (2021). We take the computed $e_{\rm weight}$ from Arrigoni Battaia et al. (2019) and Cai et al. (2019). Their $e_{\rm weight}$ is calculated with a 1-arcsecond region centered on the quasar masked to avoid residuals from point spread function subtraction. All samples we compare also mask the central 1-arcsecond region for their computed $e_{\rm weight}$ or $e_{\rm unweight}$, except for den Brok et al. (2020) and Sanderson et al. (2021). The two samples with no masking are so obscured they did not need point spread function subtraction to measure the halo.

For our data in Figure 2.9, we also mask the inner 1-arcsecond of the quasar for plotted measurements, for fair comparison with other surveys which did not probe the inner halo as we have. Table 2.3 presents our best possible eccentricity measurements, without the inner 1-arcsecond masked. Without masking, our ERQ sample has median weighted and unweighted eccentricities of $e_{\rm weight} = 0.65$ and $e_{\rm unweight} = 0.66$. We give these values context by comparing them to other typical quasar values available in the literature.

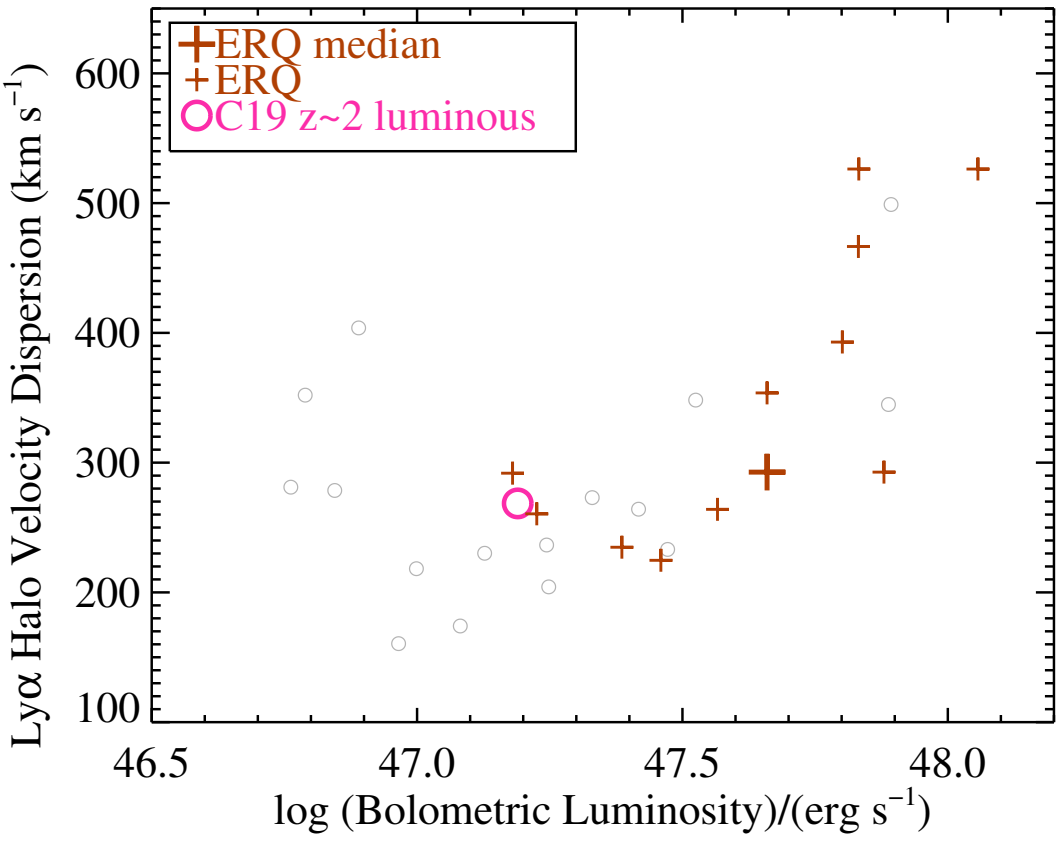

Figure 2.8: Comparison of logarithmic bolometric luminosity vs spatially integrated Lyα halo velocity dispersion for samples which it was measured, using identical legend as Figure 2.5. Halo velocity dispersion for this comparison is taken from a Gaussian fit to the spatially integrated halo spectrum, shown as the last column in Figure 2.2. Cai et al. (2019) is the only blue quasar survey from the blue quasar surveys we have considered in this paper also computed integrated halo velocity dispersion. There is a positive luminosity trend among individual quasars, but the trend is uncertain for the two sample medians available for this analysis.

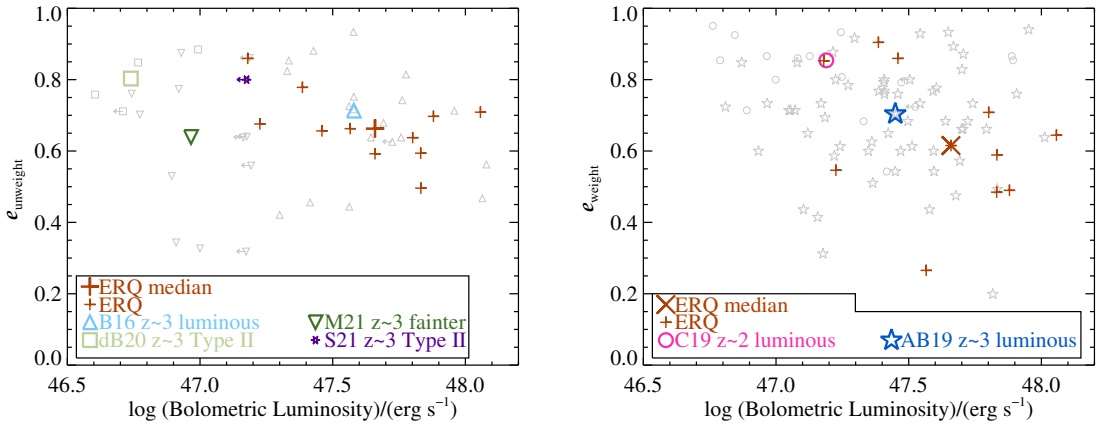

Figure 2.9: Logarithmic bolometric luminosity vs Lyα halo eccentricity, flux weighted and unweighted, for samples which have the respective measurements to compare. In addition to the identical symbols as Figure 2.5, Type-II quasars from den Brok et al. (2020) are shown in box symbols with their median shown as the large light green box, and an upper limit of an individual Type-II in Sanderson et al. (2021) is shown as a purple star. Eccentricity of zero is circular, and values near one are more elliptical. Plotted ERQ eccentricity values are computed with the central 1 arcsecond masked to compare with the other samples that use standard PSF subtraction, and Table 2.3 shows the eccentricity values calculated without masking the central 1 arcsecond. Flux-unweighted eccentricity is a measure of the outer halo shape, whereas the flux-weighted eccentricity is more strongly influenced by the brighter inner halo regions. In the flux unweighted plot there is some separation between the populations of Type-I and Type-II quasar samples, which is more clear in the median symbols.

Flux unweighted eccentricity is insensitive to strong central emission, and thus can describe morphology at large scales. Blue quasar samples have $e_{\rm unweight} \approx 0.7$, and are comparable to the less luminous population seen in Mackenzie et al. (2021). Our ERQs tend to have morphologies like blue Type-I quasar samples.

There is significant scatter in $e_{\rm weight}$ measurements among each sample, but medians of these populations show ERQs have more circular symmetry to other blue quasar Lyα halo surveys. Blue quasar samples have $e_{\rm weight} \approx 0.7 - 0.9$. Luminous quasar medians are larger than the ERQ median and most individual ERQs, tabulated in Table 2.3.

We include Type-II quasars in this morphology comparison, because other studies find that Type-IIs tend to show more asymmetric halos, consistent with more edge-on views of the quasar asymmetric illumination patterns in the normal Type-I/II dichotomy (den Brok et al. 2020). Samples of Type-II quasars have an unweighted eccentricity as high as $e_{\rm unweight} \approx 0.8$ (den Brok et al. 2020; Sorini et al. 2021). The ERQ in our sample with narrowest C IV emission line FWHM, J1705+2736, is similar to the other Type-IIs, and has the largest unweighted eccentricity in our sample with $e_{\rm unweight} = 0.78$. J1705+2736 also has the largest flux weighted eccentricity of our sample, and greater than of most of the Type-I blue quasars, with $e_{\rm weight} = 0.91$.

2.4 Discussion

ERQs could represent a brief transition phase in galactic and quasar evolution, characterized by an obscured galactic/quasar environment and potentially extreme feedback via outflows (see Section 2.2). Our main goal is to determine if ERQs differ from normal blue quasars in significant ways that might identify them as a distinct, and potentially more youthful, galactic/quasar population. We obtained Keck KCWI data for 11 ERQs to measure their basic Lyα halo properties. In this section we will discuss our results for the full sample.

2.4.1 Quasar Systemic Redshift & Future Work

Systemic redshifts are uniquely difficult to determine for ERQs due to frequent blueshifted/fast-outflowing emission-lines that are typically used as redshift indicators, such as [O III] λ5007 and broad emission lines (Hamann et al. 2017; Perrotta et al. 2019; **?**). Our study confirms the result in L22 that the narrow Lyα spike present in aperture spectra of some ERQs are the same redshift and emission profile as the inner halo emission, and therefore this spike also forms in the inner halo and is a good indicator of ERQ systemic redshifts. This result is true for J1652+1728, in spite of the innermost halo being blueshifted relative to the outer regions, and JWST (Gardner et al. 2006) results show there are multiple emission components with different kinematics (Wylezalek et al. 2022; Vayner et al. 2023). L22 used the Lyα spike redshift in the reddest ERQ, J0006+1215, to show the centroid of the broad C IV λ1549 emission line is blueshifted by 2240 km s^{-1}. Hamann et al. (2017) provides other examples of large broad emission-line blueshifts in ERQs based on the Lyα spike, claiming that large blueshifts are more common in ERQs than luminous blue quasars. We present a more complete discussion of blueshifts and their implications for ERQ outflows in Gillette et al. 2023a.

2.4.2 Circularly Symmetric and Compact Halos

Overall we find that ERQs and blue quasars both exhibit a wide range of Lyα halo properties and there is considerable overlap between these samples. The main differences identified by our study are in the halo morphologies. In particular, the ERQs tend to have 1) more compact and centrally concentrated SB profiles, and 2) more circularly symmetric central regions. Fig. 2.7 shows other samples which have circularly averaged SB radial profiles measured have median exponential

scale lengths between 13.5 and 18.7 kpc, and the scale length of the median profile of our full sample is 9.0 kpc. When considering only ERQs that exhibit a Lyα spike, the median profile's exponential scale length is only 6.0 kpc. Fig. 2.9 shows the flux-weighted elliptical eccentricities of our sample are much smaller, probing the inner halo, and meaning more circularly symmetric.

Reasons for ERQs having more compact and more circular morphology are unclear. They are possibly related to a younger evolution stage than blue quasars, for example, if the outflows from ERQs (e.g. Perrotta et al. 2019; Gillette et al. 2023a) have not had time yet to distort and disperse the gas in their inner halo. Compact and circular morphology also supports the argument that ERQs do have Type-I orientation in spite of their obscuration.

2.4.3 Type-I versus Type-II Quasars

We can gain insights into the dust distribution around ERQs from the halo morphology being more similar to Type-I blue quasar samples than Type-II samples. Previous studies have shown that Type-IIs tend to have more asymmetric Lyα halos, consistent with Type-IIs having a more edge-on view of the asymmetric (bipolar) radiation pattern of quasars in the standard Type-I/II dichotomy (Antonucci 1993; Urry & Padovani 1995; Netzer 2015; den Brok et al. 2020).

Gas distribution asymmetry is evident in the eccentricity parameters plotted in Fig. 2.9, although the sample sizes are small and there is considerable overlap in values between samples. ERQs tend to have more symmetric halo morphologies than Type-I blue quasars, making them even more different from the Type-IIs.

One ERQ in our sample, J1705+2736, has considerable asymmetry in its outer Lyα halo morphology, and has an asymmetric and luminous arm that extends >70 kpc from the quasar. J1705+2736 has substantially narrower FWHM(C IV) than the other ERQs, similar to other Type-II

quasars, although FWHM(C IV) alone is known not to be a good discriminator for Type-I versus Type-II classification (Greene et al. 2014; Hamann et al. 2017). Fig. 2.4 shows J1705+2736's extended emission, that is uniformly blueshifted from the central halo by about -100 km s^{-1}, and out to >70 kpc in the southern direction.

Thus it appears that the large line-of-sight extinctions toward ERQs cannot be attributed to viewing effects analogous to Type-IIs in the simplified picture of Type-IIs versus Type-I quasars. Our conclusion that ERQs are more similar to Type-I's is supported by the finding in L22 that the He II/Lyα line ratio in the ERQ J0006+1215 (the only ERQ for which those lines are measured) is more similar to Type-I blue quasars than Type-IIs (see section 4.5 in L22 for more discussion).

2.4.4 No Evidence of Halo Feedback

Figure 2.8 reveals ERQs appear to follow the same trend as blue quasars for larger velocity dispersions around quasars with larger bolometric luminosity. Overall the halos are kinematically quiet, with integrated velocity dispersion in the range 225−526 km s^{-1}, similar to matched blue quasars.

We compare these velocity dispersions with emission-line broadening expected from the orbital motions of gas in the host galaxy's dark matter halo. Dispersion velocities greater than what could be expected from gas dominated by the influence of dark matter may be evidence of feedback by the host galaxy/quasar. We assume a dark matter halo profile from Navarro et al. (1997), and halo concentration parameter of 4, from the COLOSSUS software and references therein.[1] We then use the halotools software to calculate the circular velocity for an upper limit for the projected 1D

[1] https://bdiemer.bitbucket.io/colossus/halo_concentration.html

velocity.[2] Our sample is on the high end of quasar luminosities, and further studies have found that obscured quasars and hyperluminous quasars may on average reside in more massive halos, typically $10^{13} h^{-1} M_{\odot}$ (DiPompeo et al. 2017; Geach et al. 2019). Using this dark matter halo mass estimate we find σ_{1D} = 379 km s^{-1}, corresponding to a 1D circular velocity of 536 km s^{-1}. Therefore, halo gas with line-of-sight velocity much greater than 379 km s^{-1}could be considered fast moving, and may be disrupted by, or possibly involved in, an outflow.

Table 2.6 presents our integrated Lyα halo dispersion. Velocity dispersions of our sample have a median dispersion of 293 km s^{-1}, are within a few hundred km s^{-1}of each other, and none are above the fast moving circular velocity estimate. Quiet kinematics do not rule out the possibility of youth in ERQs, because they may have had less time for energetic outflows to extend outward to generate feedback in the inner halo.

Across the sample we generally do not find Lyα halo emission-line broadening above the expected dark matter halo velocities down to ~0.7 arcsec or ~6 kpc radius. Episodic lifetimes of quasars are typically $10^5 - 10^7$ yrs (e.g., Khrykin et al. 2021). Our median velocity dispersion is roughly ~400 km s^{-1}, a typical Lyα halo velocity in the blue quasar samples, and can at most only travel to ~4 kpc. Therefore Lyα emission on circumgalactic scales may not be outflowing due to the present quasar episode. Spatially resolved velocity dispersion beyond 20−30 kpc is more commonly measured in ERQs with a Lyα spike. These more extended halos gradually decrease velocity dispersion toward the edges, away from the quasar. Instances of extended clouds (eg. J1145+5742 and J1451+0132) also show a decrease in dispersion farther along the extended arm, but J0006+1215 shows increasing dispersion with increasing distance along its extended arm. We

[2] https://halotools.readthedocs.io/en/latest/api/halotools.empirical_models.NFWProfile.html

do not find evidence for large velocity dispersion in the Lyα halos that may be caused by outflows and feedback effects from the central quasar, but an absence of fast outflows in our sample has no implications on the quasar evolutionary stage.

In conclusion, the quiet kinematics, and the compact and circular symmetry discussed in Section 2.4.2, are evidence against feedback being present at CGM halo scales, now or in the past.

2.4.5 General Halo Properties

If ERQs are in younger host galaxies, then they may have different ionizing escape fractions compared to typical blue quasars. If the galaxy is dusty, then the escape fraction could be lower. But if the dust distributions are clumpy, then they may have substantial ionization escape fractions. Luminosities of the Lyα halos are comparable to typical luminous blue quasars of similar redshift in Fig. 2.5. We also see in Fig. 2.6 that ERQ halo linear size is within the size distributions in other samples of luminous quasars. The median ERQ halo luminosity is offset roughly two times lower than expected from the blue quasar data, but this does not appear significant given the small sample size and the width of the halo luminosity distributions spanning nearly a factor of 100. Thus the appearance of narrow Lyα emission spikes in ERQ spectra can be attributed to extinction toward the central quasar, and not from unusually bright halo emission, relative to the central quasars.

If the Lyα halo emissions are powered by hydrogen-ionizing radiation from the central quasars, the similar halo luminosities between ERQs and blue quasars might indicate that similar fractions of the H-ionizing photons emitted by the quasars escape to the circumgalactic medium in ERQs. This similarity is notable because of the much larger line-of-sight extinctions observed in ERQs, estimated to be typically ~3 mags or a factor of ~16 in the near UV around 1500 Å to 2000 Å (Hamann et al. 2017). One possible explanation is that other lines-of-sight toward ERQs have

lower extinctions than we observe, allowing their ionizing photons to escape in quantities similar to blue quasars. Another possibility is that the dust distributions are clumpy and inhomogeneous, which can permit larger UV photon escape fractions than expected from the extinctions along direct lines of sight to the central source, due to scattering. The general notion that dust scattering plays an important role is consistent with the large UV polarizations found in some ERQs by Alexandroff et al. (2018); however, they attribute their results to a particular axisymmetric scattering geometry that might conflict with our finding that ERQs tend to have circularly symmetric halos, resembling Type-I blue quasars (Section 2.4.3).

An important caveat to keep in mind for the $L_{\rm halo}$ comparisons is that Lyα halos around quasars are generally believed to be at least partly matter bounded, meaning that the observed luminosities depend at least partly on the amount of halo gas available for ionisation, not simply on the flux or escape fraction of ionising photons emitted by the quasar. ERQs show a weaker than expected Lyα halo luminosity for their bolometric luminosity, which could be evidence of matter bounded halo emission (Dempsey & Zakamska 2018, also Fig. 2.5). In an ionization bounded scenario we expect the luminosity of the halo to scale linearly with bolometric luminosity, but when a halo is matter bounded there is no dependence. However, real quasars can show a weak dependence of the halo properties on the bolometric luminosity, and any relation between Lyα halo luminosities and extinction toward the quasars will also be weak.

A unique feature of our study is that extreme obscuration allows us to map the 2D halo emissions all the way down to the quasar positions, and possibly down to galactic emission, in roughly half of our ERQ sample. ERQs that exhibit the Lyα spike show similar inner halo characteristics as J0006+1215 in L22, but vary in their outer region symmetry and morphology beyond 20−30 kpc

from the emission peak. ERQs without the spike are most luminous around the central region of the quasar, and tend to be less extended to outer regions beyond 30−40 kpc from the halo emission peak (see Fig. 2.2).

2.4.6 Multi-component Emission

In several ERQs with spatially resolved measurements, a transition at ∼20−30 kpc from the quasar frequently occurs (e.g., a drop off in SB, change in blueshift, or velocity dispersion). This transition leads us to define a boundary of inner-halo and outer-halo Lyα emission. This boundary could be evidence of a 2-component halo structure of compact and extended gas (e.g., J1145+5742 and J1652+1728). L22 showed a halo transition phase 20−30 kpc from the position of ERQ J0006+1215, defining an inner and outer halo component. The inner region is more coherent, circularly symmetric, and has quiet gas kinematics, and the outer region has more asymmetric and disrupted kinematics. One possibility is that the outer halo is inflowing CGM gas, and the inner halo is dominated by outflow (see section 4.2 in L22 for more discussion). This is further supported in multi-component JWST observations of J1652+1728, which found complex gas kinematics and outflows on kpc scales (Vayner et al. 2023). Figure 2.4 shows aperture spectra of ERQs with distinct inner and outer halo emission regions that show different kinematics from each other.

Many of our ERQ Lyα halos show a smooth gradient in their velocity shift from one side of the halo to the other, with zero velocity centered near the halo emission peak. None have extreme velocities consistent with powerful outflow. In cosmological radiation-hydrodynamic simulations from Costa et al. (2022) quasar driven outflows on circumgalactic scales move ∼1,000 km s^{-1}, and are also less dense than most Lyα emitting gas.

In summary, our comparison of ERQ Lyα halo properties to blue quasars has revealed many similarities, and some contrasting characteristics that distinguish them from simple orientation effects. Extended morphology of halos around ERQs appear similar to those of blue quasars, but the inner halo is more circularly compact. Future work with larger samples and/or deeper maps could help resolve the evolution/youth question. Further exploration into ERQs as an evolutionary stage (eg., Perrotta et al. 2023 and Hamann et al. 2023) will investigate the host galaxies for comparison to blue quasars.

2.5 Conclusions

We present a sample of 11 ERQs observed with KCWI Integral Field Spectroscopy, which have median redshift $z = 2.6$, a median color of i–$W3 = 5.9$ mag, and median bolometric luminosity $L_{\rm bol} \approx 5 \times 10^{47}$ erg s^{-1}. Except for one ERQ observed under cloudy conditions, all have detected Lyα halos, and have a median halo luminosity $L_{\rm halo} = 5.83 \times 10^{43}$ erg s^{-1}.

The median of Lyα emission's maximum linear size is >128 kpc, and exponential scale length of the circularly averaged SB radial profile median is 9.0 kpc. Morphology is generally circular around the inner halo regions, with a median flux-weighted eccentricity of $e_{\rm weight} = 0.65$ and unweighted $e_{\rm unweight} = 0.66$. One ERQ in our sample, J1705+2736, that has substantially narrower emission line widths, has the most asymmetric morphology in its outer halo with $e_{\rm unweight} = 0.78$, and compared to the rest of the ERQ sample has the most asymmetric inner halo with $e_{\rm weight} = 0.91$.

Kinematics of the halos are relatively calm, with velocity shifts of the Lyα emission centroid to be in the hundreds of km s^{-1}, and much weaker than the shifts found in [O III] for ERQs in the thousands of km s^{-1}by Perrotta et al. (2019). Velocity maps are coherent, with some showing

a gradual gradient from red to blue velocity shifts across the halo. Dispersion of the halo emission is also quiet, with a spatial median dispersion of 374 km s^{-1}, and standard deviation of 114 km s^{-1}.

Our measured quantities of size, luminosity, blueshift, and dispersion show ERQs are mostly similar to those obtained in blue quasar surveys. ERQs generally follow luminosity trends that are seen across faint to luminous blue quasar samples for halo linear-size, luminosity, and velocity dispersion. However, ERQs do stand apart from similarly luminous blue quasars in that their halos are more circularly compact.

Most of the statements and inferences about ERQ populations made in L22 are supported by this work with the addition of 10 other Lyα halos, summarized below:

- We do not see a color correlation with Lyα luminosity or kinematics across our sample.
- At circumgalactic scales we do not find clear evidence of feedback based on the circularly symmetric inner halos and low velocity dispersions (see Sections 2.4.2 & 2.4.4).
- Lyα halo velocity dispersions are mostly consistent with circular velocities of halo gas at a typical dark matter halo mass (see Section 2.4.4).
- Our sample's illumination patterns are similar to other blue quasars based on Lyα halo morphologies, characterized by elliptical eccentricity parameters (see Section 2.3.4).
- ERQ halos are more circularly concentrated, and could mean they have had less time to extend by outflows from the innermost unresolved regions (see Section 2.4.2).
- Obscuration acting as a chronograph allows for measurements of narrow Lyα emission lines, and these lines can be used as systemic redshift estimators for constraining broad line emission blueshifts and outflows (see Section 2.4.1).

Chapter 3

Paper II: Accurate Systemic Redshifts and Outflow Speeds for Extremely Red Quasars (ERQs)

3.1 Abstract

Extremely Red Quasars (ERQs) are thought to represent a brief episode of young quasar and galactic evolution characterized by rapid outflows and obscured growth due to dusty environments. We use new redshift measurements from CO and narrow Lyα emission-lines to better constrain outflow velocities from previous line measurements. We present sample of 82 ERQs, and the analysis confirms that ERQs have a higher incidence of large C IV blueshifts, accompanied by large Rest Equivalent Width (REW) and narrower line Full-Width at Half-Maximum (FWHM) than blue quasars. We find that strong blueshifts (>2000 km s^{-1}) are present in 12/54 (22.2%) of ERQs with

the most robust redshift indicators. At least 4 out of 15 ERQs in the sample also have blueshifts in their Hβ and low-ionization UV lines ranging from -500 to -1500 km s^{-1}. ERQs with strong C IV blueshifts are substantially offset in C IV REW and FWHM from typical blue quasars in the same velocity range. ERQs have average values of REW = 124Å and FWHM = 5274 km s^{-1}, while blue quasars have REW = 24Å and FWHM = 6973 km s^{-1}. The extreme nature of the outflows in ERQs might explain some of their other spectral properties, such as the large C IV REWs and peculiar wingless profiles owing to more extended broad-line regions participating in outflows. The physical reasons for the extreme outflow properties of ERQs are unclear; however, larger Eddington ratios and/or softer ionizing spectra incident on the outflow gas cannot be ruled out.

3.2 Introduction

Quasars are supermassive black holes rapidly growing by accretion of infalling material at the center of their host galaxy. Accretion can coincide with streams of infalling gas, or galactic assembly, at high redshift. Merger activity, or infalling gas, may be the triggers supplying matter for starbursts and quasar activity (Hopkins et al. 2006, 2008; Somerville et al. 2008; Kereš et al. 2009; Dekel et al. 2009; Faucher-Giguère & Kereš 2011; Fumagalli et al. 2014; Glikman et al. 2015). This rapid accretion can coincide with outflows, generating feedback, and potentially influence the galaxy's formation (Costa et al. 2014; Nelson et al. 2015; Suresh et al. 2019). A possible evolutionary scheme is where the central black hole initially grows in obscurity until feedback generates outflows, and clears the obscuring interstellar material, revealing a normal blue quasar (Sanders et al. 1988; Di Matteo et al. 2005; Hopkins et al. 2006, 2008, 2016; Rupke & Veilleux 2011, 2013; Liu et al. 2013; Stacey et al. 2022).

Red quasars are important for testing the hypothesis that obscured quasars may be in a young, and short-lived, phase in their evolution. Young quasars may be reddened by dust created in a major starburst inside the galaxies, triggered by a merger or cold-mode accretion, as they transform in to blue/unobscured quasars. Red quasars are often selected based on combinations of UV/optical, infrared, or radio emission properties, and may show signs of youth such as high accretion rates, more infall from the intergalactic medium, or powerful outflows (Richards et al. 2003; Glikman et al. 2007; Klindt et al. 2019; Fawcett et al. 2020; Rosario et al. 2020; Calistro-Rivera et al. 2021; Glikman et al. 2022). Studies of red/obscured quasars have found many to be in mergers or high-accretion phases (Glikman et al. 2015; Wu et al. 2018; Zakamska et al. 2019).

Extremely red quasars (ERQs) are a unique quasar population selected from the Baryon Oscillation Spectroscopic Survey (BOSS, Pâris et al. 2017a) in the Sloan Digital Sky Survey-III (SDSS, Eisenstein et al. 2011) and the ALLWISE data release (Cutri et al. 2011, 2013) of the Wide-field Infrared Survey Explorer (WISE, Wright et al. 2010a), based on red rest-UV to mid-IR colors, i–$W3$>4.6 (AB magnitudes Ross et al. 2015; Hamann et al. 2017). They are of particular interest because of a suite of other spectral properties connected to their extreme red colors, namely, unusually strong C IV λ1549 emission lines with peculiar wingless profiles and frequent large blueshift, a high incidence of broad C IV outflow absorption lines, and exceptionally fast outflows measured in [O III] λ4959,5007 (Hamann et al. 2017; Perrotta et al. 2019). All of these features might be explained by exceptionally powerful accretion-disk outflows. For example, these outflows might create spatially-extended C IV broad emission line regions, resulting in large C IV rest equivalent widths (REWs). Additionally, these outflows may also feed into the fast, lower-density [O III] outflows farther away (Zakamska et al. 2016; Hamann et al. 2017; Perrotta et al. 2019). This evidence for prodigious

outflows, combined with the extreme dust reddening, make ERQs prime candidates for quasars driving feedback to their host galaxies during the early stages of massive galaxy evolution.

An essential ingredient for understanding quasar outflows, and the exotic properties of ERQs in particular, is accurate systemic redshifts to define the outflow speeds and kinetic energies. The most accurate redshift indicators are narrow emission lines, like [O III] λ5007, that form in the extended galactic or circumgalactic environments of quasars. When these lines are not available, Hβ and various low-ionization broad emission lines in the UV, such as Mg II λ2800, O I λ1304, can be useful for normal quasars because they are less likely to be blueshifted (i.e., participating in outflows) than high-ionization emission lines like C IV (e.g. Shen et al. 2008; Shen et al. 2016b; Li et al. 2017).

However, these redshift indicators are often problematic for ERQs because outflow signatures are more common and more extreme throughout their spectra. In particular, their [O III] lines are typically very broad and blueshifted with no distinct narrow components that might form in the extended/galactic environments (Zakamska et al. 2016; Perrotta et al. 2019). ERQ low-ionization broad emission lines often have large measurement uncertainties due to noisy spectra, and they might be affected by large blueshifts/outflow speeds throughout the broad emission-line region (including more than just the high-ionization gas, see Section 3.4 below).

In this paper, we provide reliable systemic redshifts for a sample of 82 ERQs that have existing measurements of CO in their host galaxies (Hamann et al. 2023 in preparation) and/or narrow Lyα emission lines (Lau et al. 2022; Gillette et al. 2023b, and this work) that form in their extended circumgalactic and/or halo environments. CO from the host galaxy will have emission centroids more closely coinciding with the central black hole velocity (Hamann et al. in prep.).

We then use these data to derive blueshifts/outflow speeds for the ERQ C IV λ1549 broad emission lines and, whenever possible, reassess the [O III] λ5007 outflow speeds reported by (Zakamska et al. 2016; Perrotta et al. 2019, and by Lau et al. in prep.). Our findings provide more accurate results, but support previous claims that ERQs have an unusually high frequency of fast/powerful outflows in these emission line regions, e.g., compared to normal blue quasars at similar redshifts and luminosities.

This paper is organized as follows. Section 3.3 describes selection criteria for quasars from catalog spectra and their redshifts. Section 3.4 describes our revised C IV and [O III] emission-line blueshifts and outflows. Section 3.5 discusses and summarizes correlations in measured parameters and emission features, such as blueshift, emission strength, and line width. Throughout this paper we adopt a Λ-CDM cosmology with H_0 = 69.6 km s^{-1} Mpc^{-1}, Ω_M = 0.286 and Ω_Λ = 0.714, as adopted by the online cosmology calculator developed by Wright (2006). All magnitudes are on the AB system. Reported wavelengths are in vacuum and in the heliocentric frame.

3.3 Sample Selection & Systemic Redshifts

The parent sample for our study is the 205 ERQs selected to have i–$W3$ >4.6 in the combined BOSS survey Hamann et al. (2017). Those authors provide detailed data for the C IV emission lines, including velocity shifts relative to the BOSS DR12 catalogue redshifts (see Appendix A in Hamann et al. 2017). The DR12 redshifts derive from automated fits to the BOSS spectra, plus algorithmic corrections based on nominal line blueshifts, using lines that can be off by hundreds or >1000 km s^{-1} for quasars like ERQs with unusual emission-line properties Hamann et al. (2017).

For the present study, we select ERQs from Hamann et al. (2017) that have other, more reliable measurements of the quasar systemic redshifts. These include 14 ERQs with ALMA sub-mm CO(4-3) emission-line measurements by Hamann et al. (2023 in prep.), 6 ERQs with KCWI (integrated field spectroscopy) of the extended Lyα halos by Gillette et al. (2023b), and 54 ERQs with narrow Lyα emission spikes in their BOSS spectra caused by halo emission. For some of our analysis, we also include 8 ERQs that have well-measured Mg II emission lines in their BOSS spectra, as measured by Gillette & Hamann (2023).

Table 3.1 and 3.2 lists some basic catalogue properties and measurements for the total sample of 82 ERQs. The total ERQ sample has median color i–$W3 \approx 5.3$ and redshifts in the range $1.8 \leq z \leq 3.7$. The subsample of 20 ERQs with $z_{\rm best}$ from either CO or Lyα-halo has median color i–$W3 \approx 5.7$, while the 54 ERQs with only a Lyα-spike redshift have median color i–$W3 \approx 5.1$. The small color difference between these two subsamples can be attributed to two factors beyond counting statistics in the samples sizes: 1) our preference for redder ERQs in the ALMA CO and KCWI Lyα-halo observations, and 2) redder ERQs having fainter rest-UV fluxes that lead to noisier BOSS spectra and greater difficulty in identifying a narrow Lyα-spike for our study (Section 3.3).

We include a large comparison sample of 39,909 typical quasars from the SDSS survey with systemic redshifts measured from the Mg II λ2800 broad emission lines (Gillette & Hamann 2023). Mg II provides reasonably accurate systemic redshifts for normal blue quasars (Richards et al. 2002). For example, Shen et al. (2008) report that, in a large sample of SDSS quasars, the Mg II line has average blueshift relative to [O III] of -97 km s^{-1} and a dispersion in the measured shifts of 269 km s^{-1}. The sample with Mg II measurements are from emission-line profile fitting to SDSS BOSS spectra, which is done with similar methodology as described in Hamann et al. (2017), and with care

taken to exclude bad data with custom signal-to-noise measurements and rejection criteria. Mg II emission is fit with a symmetric Gaussian or double-Gaussian profile, after the Fe II complex near Mg II is removed using a Fe II emission template.C IV blueshifts are determined for the blue quasar sample by calculating the velocity shift of its centroid from the Mg II profile centroid. The typical blue quasars have median redshift $z \approx 2.2$, luminosity $L \approx 8.89 \times 10^{45}$ erg s^{-1}, and i–$W3 \approx 2.4$. A detailed description and results of the fitting in the blue quasar sample is presented in Gillette & Hamann (2023).

3.3.1 Systemic Redshift Priorities

Some ERQs in our sample have available more than one of the systemic redshift indicators mentioned above. We choose a single value of $z_{\rm best}$ for each quasar based on the following priorities. The CO(4-3) emission line has highest priority because it forms (primarily) in dense molecular clouds inside the host galaxies. Although there can be gas motions within the galaxies, we expect the CO line centroids to have velocities similar to the central black holes/quasars (see Hamann et al. 2023 in prep. for discussion). Thus we adopt the CO line centroids provided by Hamann et al. (2023, in prep.), measured from spatially-integrated spectra, for $z_{\rm best}$ when available.

Second priority for $z_{\rm best}$, if a CO(4-3) measurement is not available, is a narrow Lyα emission line arising from the spatially-resolved ERQ halo/circumgalactic medium (as measured from Keck-KCWI observations by Lau et al. 2022; Gillette et al. 2023b). CO is trusted more-so than Lyα indicators to minimize the possible uncertainty of asymmetric bulk motions of the halo,

Table 3.1: ERQ Sample Color and Redshift Indicators. z_{em} is from the SDSS DR12Q BOSS catalogue emission-line measurement. $W3$ magnitude, and i–$W2$ color are from WISE and BOSS. $z_{\rm best}$ is the best estimate of the reference systemic redshift based on either CO (from Hamann et al. 2023 in prep.), narrow Lyα emission lines in the extended ERQ halos (from Gillette et al. 2023b), or narrow Lyα emission-line "spikes" as measured here (Section 2) from the BOSS spectra.
Notes. [a] ERQ's BOSS spectra show strong Mg II or O I emission as well as having a CO or Lyα redshift indicator.

ERQ Name	z_{em}	W3 (mag)	i–$W3$ (mag)	$z_{\rm best}$	$z_{\rm best}$ indicator
J000610.67+121501.2	2.3099	14.09	8.01	2.3183	CO
J002400.67−081110.2	2.0633	16.19	4.63	2.0638	Mg II
J005233.24−055653.5	2.3542	16.00	6.37	2.3631	CO
J011601.43−050503.9	3.1825	15.53	6.24	3.1875	Lyα-Spike
J015222.58+323152.7	2.7859	15.76	5.39	2.7925	Lyα-Spike
J022052.11+013711.1	3.1376	15.75	6.24	3.1375	Lyα-Halo
J080547.66+454159.0	2.3258	15.51	6.32	2.3127	Lyα-Spike
J082224.01+583932.8	2.5469	15.37	4.81	2.5667	Lyα-Spike
J082536.31+200040.3	2.0938	16.77	4.74	2.0881	Lyα-Spike
J082653.42+054247.3	2.5734	15.18	6.01	2.5780	CO
J083200.20+161500.3	2.4472	14.98	6.74	2.4249	CO
J083448.48+015921.1	2.5942	14.86	5.99	2.5850	CO
J084447.66+462338.7	2.2168	15.15	5.96	2.2226	Lyα-Spike
J085039.50+515831.0	1.8914	15.62	4.97	1.9003	Mg II
J085229.65+524730.8	2.2674	16.48	4.74	2.2526	Lyα-Spike
J090014.07+532148.7	2.1098	17.00	7.31	2.1042	Mg II
J090306.18+234909.8	2.2635	16.91	5.02	2.2686	Mg II
J091303.90+234435.2	2.4195	16.41	5.31	2.4335	Lyα-Spike
J092049.59+282200.9	2.2959	15.95	4.83	2.2976	Lyα-Spike
J092604.08+524652.9	2.3467	17.13	4.71	2.3516	Lyα-Spike
J093638.41+101930.3	2.4531	15.42	6.17	2.4523	Lyα-Spike
J095033.51+211729.1	2.7447	16.33	5.52	2.7430	Lyα-Spike
J101326.23+611219.9	3.7028	15.17	5.91	3.7061	Lyα-Spike
J101533.65+631752.6	2.2255	16.39	5.48	2.2337	Lyα-Spike
J102353.44+580004.9	2.5972	15.97	5.11	2.5996	Lyα-Spike
J104718.35+484433.8	2.2751	15.57	5.30	2.2767	Lyα-Spike
J104754.58+621300.5	2.5361	16.25	5.08	2.5566	Lyα-Spike
J110202.68−000752.7	2.6261	17.05	4.87	2.6261	Lyα-Spike
J111346.10+185451.9	2.5160	17.07	4.62	2.5188	Lyα-Spike
J111516.33+194950.4	2.7924	17.04	4.96	2.7989	Lyα-Spike
J111729.56+462331.2	2.1317	15.55	6.26	2.1309	Lyα-Spike
J112124.55+570529.6	2.3834	14.98	5.07	2.3885	Lyα-Spike
J113721.46+142728.8[a]	2.3008	15.13	4.87	2.3025	CO
J113834.68+473250.0[a]	2.3105	15.85	6.09	2.3146	Lyα-Spike

Table 3.1: *continued.*

ERQ Name	z_{em}	W3 (mag)	i–$W3$ (mag)	$z_{\rm best}$	$z_{\rm best}$ indicator
J113931.09+460614.3	1.8202	15.30	6.44	1.8182	Mg II
J114508.00+574258.6	2.7904	14.27	4.84	2.8747	Lyα-Halo
J121253.47+595801.2	2.5841	15.85	4.95	2.5619	Lyα-Spike
J121704.70+023417.1	2.4163	15.43	5.59	2.4280	CO
J122000.68+064045.3	2.7963	16.57	4.88	2.7732	Lyα-Spike
J123241.73+091209.3	2.3814	14.39	6.76	2.4050	CO
J124106.97+295220.8	2.7935	16.49	5.35	2.7976	Lyα-Spike
J124738.40+501517.7	2.3858	16.53	4.97	2.4014	Lyα-Spike
J125019.46+630638.6	2.4016	16.42	5.47	2.4049	Lyα-Spike
J125944.55+240708.3	2.1660	16.04	4.60	2.1665	Mg II
J130114.46+131207.4	2.7867	16.26	5.11	2.7892	Lyα-Spike
J130630.66+584734.7	2.2970	16.71	5.01	2.2986	Lyα-Spike
J130936.14+560111.3	2.5687	15.47	6.45	2.5794	Lyα-Spike
J131047.78+322518.3	3.0168	15.05	5.26	3.0164	Lyα-Spike
J131330.67+625957.2	2.3681	17.50	4.67	2.3714	Lyα-Spike
J131351.23+345405.3	1.9718	15.17	4.64	1.9706	Mg II
J131628.32+045316.2	2.1446	15.55	5.74	2.1598	CO
J131833.76+261746.9	2.2721	16.39	4.91	2.2746	Lyα-Spike
J132654.95−000530.1	3.3241	15.17	4.75	3.3068	Lyα-Spike
J133611.79+404522.8	2.0793	14.10	6.51	2.0882	Mg II
J134254.45+093059.3[a]	2.3430	15.92	4.90	2.3470	CO
J134417.34+445459.4	3.0359	15.54	6.78	3.0408	Lyα-Spike
J134800.13−025006.4	2.2495	15.91	5.70	2.2374	CO
J135557.60+144733.1[a]	2.7037	15.71	4.71	2.6880	Lyα-Spike
J135608.32+073017.2	2.2691	16.52	5.08	2.2716	Lyα-Spike
J143159.76+173032.6	2.3765	16.02	5.82	2.3880	Lyα-Spike
J143853.61+371035.3	2.3931	15.81	5.50	2.3981	Mg II
J144932.66+235437.2	2.3428	16.79	4.73	2.3453	Lyα-Spike
J145113.61+013234.1	2.7734	14.77	5.67	2.8130	Lyα-Halo
J145148.01+233845.4	2.6214	15.01	5.51	2.6348	Lyα-Halo
J150117.07+231730.9	3.0254	16.20	5.90	3.0204	Lyα-Spike
J152941.01+464517.6	2.4201	15.92	4.82	2.4189	Lyα-Spike
J153108.10+213725.1	2.5689	16.92	5.23	2.5639	Lyα-Spike
J153446.26+515933.8	2.2650	17.01	4.73	2.2658	Lyα-Spike
J154243.87+102001.5	3.2150	15.62	6.58	3.2166	Lyα-Spike
J154743.78+615431.1	2.8682	16.81	4.89	2.8674	Lyα-Spike
J154831.92+311951.4	2.7364	16.91	4.82	2.7462	Lyα-Spike
J155725.27+260252.7	2.8201	16.91	4.92	2.8217	Lyα-Spike
J164725.72+522948.6	2.7193	16.40	5.23	2.7206	Lyα-Spike

Table 3.1: *continued.*

ERQ Name	z_{em}	W3 (mag)	$i-W3$ (mag)	$z_{\rm best}$	$z_{\rm best}$ indicator
J165202.64+172852.3	2.9425	14.91	5.39	2.9548	Lyα-Halo
J170558.64+273624.7	2.4483	15.48	5.13	2.4461	Lyα-Halo
J171420.38+414815.7	2.3419	16.65	4.70	2.3303	Lyα-Spike
J211329.61+001841.7	1.9961	16.08	7.05	1.9998	Lyα-Spike
J220337.79+121955.3	2.6229	15.50	6.21	2.6229	Lyα-Spike
J221524.00−005643.8	2.5086	16.06	6.17	2.5093	CO
J222307.12+085701.7[a]	2.2890	15.65	5.60	2.2902	CO
J223754.52+065026.6	2.6088	16.17	5.79	2.6117	Lyα-Spike
J232326.17−010033.1	2.3561	15.22	7.19	2.3805	CO

Table 3.2: ERQ Sample Emission Profile Properties and Kinematics. C IV REW, Full-Width at Half-Maximum (FWHM), and Blueshifts are from emission-line profile fitting done in Hamann et al. (2017). [O III] λ5007 emission blueshift measurements are from Perrotta et al. (2019), when available, and blueshifted from the reference systemic.
Notes. [b] [O III] v_{98} blueshift determined from Keck-OSIRIS observations by Lau et al. (in prep.).

ERQ Name	C IV REW (Å)	C IV FWHM (km s^{-1})	C IV shift (km s^{-1})	[O III] v_{98} (km s^{-1})
J000610.67+121501.2	107	4540	−2260	−5959
J002400.67−081110.2	53	2042	108	-
J005233.24−055653.5	188	2451	−1469	-
J011601.43−050503.9	94	2291	−1240	-
J015222.58+323152.7	136	3677	−980	-
J022052.11+013711.1	328	2613	−576	-
J080547.66+454159.0	109	2667	−524	−4982
J082224.01+583932.8	65	5474	−3246	-
J082536.31+200040.3	211	3265	−473	-
J082653.42+054247.3	205	2434	−369	−3420
J083200.20+161500.3	300	3082	−297	−5258
J083448.48+015921.1	209	2863	198	−4426
J084447.66+462338.7	161	1656	−225	-
J085039.50+515831.0	65	1145	−1062	-
J085229.65+524730.8	64	1291	−322	-
J090014.07+532148.7	47	4296	−756	-
J090306.18+234909.8	144	2481	−372	-
J091303.90+234435.2	145	2190	−448	−2099
J092049.59+282200.9	197	1048	−99	-
J092604.08+524652.9	86	3053	−634	-
J093638.41+101930.3	172	1271	196	-
J095033.51+211729.1	272	1387	86	-
J101326.23+611219.9	281	5133	−2945	-
J101533.65+631752.6	130	2012	−394	-
J102353.44+580004.9	116	2107	−120	-
J104718.35+484433.8	158	2521	−33	-
J104754.58+621300.5	105	5081	−2382	-
J110202.68−000752.7	121	3767	−311	-
J111346.10+185451.9	127	986	−125	-
J111516.33+194950.4	247	1739	−197	-
J111729.56+462331.2	395	3053	−390	-
J112124.55+570529.6	28	1780	−392	-
J113721.46+142728.8[a]	98	4734	−2158	-
J113834.68+473250.0[a]	177	3296	−1202	−3928
J113931.09+460614.3	47	1239	110	-
J114508.00+574258.6	38	9103	−8655	-

Table 3.2: *continued.*

ERQ Name	C IV REW (Å)	C IV FWHM (km s^{-1})	C IV shift (km s^{-1})	[O III] v_{98} (km s^{-1})
J121253.47+595801.2	107	1402	181	-
J121704.70+023417.1	181	2604	−850	−2640
J122000.68+064045.3	113	1047	63	-
J123241.73+091209.3	225	4787	−3526	−7026
J124106.97+295220.8	138	2600	−1382	-
J124738.40+501517.7	135	3268	−909	-
J125019.46+630638.6	242	1881	0	-
J125944.55+240708.3	46	4284	−115	-
J130114.46+131207.4	186	1877	−347	-
J130630.66+584734.7	331	1133	−30	-
J130936.14+560111.3	161	3630	−519	-
J131047.78+322518.3	226	2794	−914	-
J131330.67+625957.2	82	1589	49	-
J131351.23+345405.3	18	2397	−98	-
J131628.32+045316.2	63	3010	−898	-
J131833.76+261746.9	150	1280	−23	-
J132654.95−000530.1	77	1607	−56	-
J133611.79+404522.8	20	6154	−2724	-
J134254.45+093059.3[a]	66	3246	−1558	−4779
J134417.34+445459.4	310	2871	−1152	-
J134800.13−025006.4	87	3654	−1059	−4221
J135557.60+144733.1[a]	118	2958	−252	-
J135608.32+073017.2	110	2043	117	−1767
J143159.76+173032.6	177	2084	−170	-
J143853.61+371035.3	29	3115	−137	-
J144932.66+235437.2	98	1352	95	-
J145113.61+013234.1	87	6231	−3376	-
J145148.01+233845.4	89	4166	−3040	-
J150117.07+231730.9	231	4035	−1940	-
J152941.01+464517.6	159	1896	151	-
J153108.10+213725.1	213	2767	−253	-
J153446.26+515933.8	127	1156	95	-
J154243.87+102001.5	114	3901	−2303	-
J154743.78+615431.1	128	1177	10	-
J154831.92+311951.4	127	3050	−1151	-
J155725.27+260252.7	56	1182	−1	-
J164725.72+522948.6	124	1905	−29	-
J165202.64+172852.3	125	2403	−1285	−2534
J170558.64+273624.7	157	1301	267	-

Table 3.2: *continued.*

ERQ Name	C IV REW (Å)	C IV FWHM (km s^{-1})	C IV shift (km s^{-1})	[O III] v_{98} (km s^{-1})
J171420.38+414815.7	130	3816	−816	-
J211329.61+001841.7	171	1565	−226	-
J220337.79+121955.3	266	1070	110	-
J221524.00−005643.8	153	4280	−1394	−3877
J222307.12+085701.7[a]	77	3661	−1130	−7760[b]
J223754.52+065026.6	141	1391	−11	-
J232326.17−010033.1	256	3989	−2756	−6458

relative to the quasar. Redshifts determined this way are denoted by "Lyα-halo" in the $z_{\rm best}$ indicator column in Table 3.1. We specifically derive redshifts from the spatially-averaged Lyα emission from extended regions around the ERQs that exclude the central ~1 arcsecond diameter. Excluding the central regions is a precaution to avoid potential i) rapid gas flows near the galactic nucleus, and ii) Lyα absorption features appearing along direct sight lines toward the central quasar.

One important result from our studies of ERQ halos with Keck-KCWI (Lau et al. 2022; Gillette et al. 2023b) was to confirm the speculation by Hamann et al. (2017) that the narrow Lyα emission spikes seen (with surprising frequency) in aperture spectra of ERQs form in their inner halos. In particular, the narrow Lyα spikes in aperture spectra consistently have profiles and redshifts very similar to the spatially-resolved halo emission in the KCWI data.

Our third priority for $z_{\rm best}$ values, when neither CO nor spatially-resolved Lyα data are available, are a narrow Lyα spike in aperture spectra of the ERQs. Lau et al. (2022) discussed ERQ J000610+121501 is a good example of the spike indicating quasar redshift, where a distinct narrow Lyα spike in aperture spectra clearly forms in the inner halo, and confirmed by mapping data from Keck-KCWI. Gillette et al. (2023b) discusses a wider range of cases, and include some where aperture spectra show the profile of narrow Lyα spike emitted from the halo blends smoothly into the broad Lyα emission line of the quasar. We selected the 59 ERQs from Hamann et al. (2017) with Lyα spikes attributable to halo emission based on the appearance of a single narrow emission peak with FWHM $<$ 1,000 km s^{-1} that is well-measured above the noise and shows no indications of overlying Lyα absorption that might distort the emission spike profile. The centroids of these spikes provide $z_{\rm best}$. Although we give these $z_{\rm best}$ values a lower priority than estimates from spatially-resolved Lyα halo data, their typical uncertainties are $\leq$~200 km s^{-1}based on both the line

measurement accuracies and our experience comparing these Lyα spikes to spatially-resolved Lyα emission from ERQ halos (Lau et al. 2022; Gillette et al. 2023b). Quasars with $z_{\rm best}$ determined this way are denoted by "Lyα-spike" in Table 3.1.

Lowest priority are the eight ERQs with $z_{\rm best}$ measurements from their low-ionization Mg II λ2800 broad emission lines (from a large general study of quasar emission-line blueshifts by Gillette & Hamann 2023). We consider these to be the least reliable redshifts because, unlike normal blue quasars, the low-ionization emission lines in ERQs can also be involved fast outflows leading to large blueshifts (see Hamann et al. 2018, also Section 3.5 below). None of these quasars with well-measured Mg II lines also have CO or Lyα measures. We note five quasars with CO, or Lyα, redshifts and also low-ionization lines with have visibly obvious peak/centroids in Mg II, indicated in Table 3.1. We calculate offset between redshift indicators, and found 14 ERQs with both CO and Lyαhalo or spike redshift measurements. Four ERQs have CO and Lyα halo measurements, with average shift and scatter of -1206 km s^{-1} and 253 km s^{-1}. Ten ERQs have both CO and a Lyα spike, with average shift and scatter -958 km s^{-1} and 1067 km s^{-1}. These offsets are in the typical range of Lyα halo peak velocity shifts, relative to systemic, seen in large surveys of blue quasars (e.g., Arrigoni Battaia et al. 2019; Cai et al. 2019).

3.3.2 Potential Biases

Before discussing emission blueshifts, we consider potential biases in the properties of our ERQ subsamples. The ALMA CO and KCWI Lyα-halo observations both tended to favor ERQs with large C IV REWs ($\gtrsim$100 Å) and relatively broad C IV profiles (FWHM $\gtrsim$ 2000 km s^{-1}). This represents the majority of ERQs having exotic spectral line/outflow properties (Section 1 of Hamann et al. 2017; Perrotta et al. 2019). We also tried to include sources with the reddest i–$W3$

colors among ERQs. Altogether, however, these samples span a wide range of ERQs because we wanted to examine a range, and because observational constraints tended to randomize the samples with respect to C IV properties (e.g., source brightness limits, scheduling constraints, and requirements for low declinations and a very narrow redshift range (near ~2.4) for the ALMA CO observations). Therefore, while these samples do intentionally include some of the most extreme ERQs, e.g., J123241+091209 and J232326−010033 with fast [O III] outflows (Zakamska et al. 2016; Perrotta et al. 2019) and J114508+574258 with a previously-known large C IV blueshift (Hamann et al. 2017), they should be overall approximately representative of the majority of ERQs with FWHM(C IV) $\gtrsim$ 2000 km s^{-1}. We also note that any remaining tendency for large C IV REWs in these sample might, if anything, favor small C IV blueshifts because large C IV REWs are known to correlate strongly with small blueshifts in the general quasar population (Richards et al. 2011; Coatman et al. 2016, 2019; Rankine et al. 2020; Temple et al. 2023, Gillette & Hamann 2023, also Section 3.4.1).

There is, however, a substantial bias in the sample of 59 ERQs selected to have a narrow Lyα spike in their BOSS spectra. There are two reasons for this. First, selecting for a narrow spike in Lyα strongly favors ERQs whose entire Lyα profile is narrow and whose other "broad" emission lines, including C IV λ1549, are also unusually narrow (e.g., compared to the average for ERQs). Second, narrow C IV emission lines correlate strongly with smaller C IV blueshifts (Figure 3.1, also Richards et al. 2011; Coatman et al. 2016, 2019; Rankine et al. 2020; Temple et al. 2023, and Gillette & Hamann 2023). The net effect is that this sample is biased towards both narrower C IV lines and smaller C IV blueshifts than the general ERQ population.

Hamann et al. (2017) hypothesizes there is significant uncertainty in using typical emission lines (such as low-ionization lines) to determine ERQ redshift, and that they are potentially co-moving within an outflow. Therefore, Mg II may be less reliable as a redshift indicator for ERQs, and could be biased in the 8 ERQs that it is utilized. For the normal blue quasars we are using to compare in this study, Mg II is considered a more robust indicator of systemic redshift (Richards et al. 2002; Richards et al. 2011; Hewett & Wild 2010; Shen et al. 2008; Shen et al. 2016b). Further discussion of using Mg II to obtain systemic redshifts for these blue quasars is reported in Gillette & Hamann (2023).

3.4 Emission-line Blueshifts & Outflow Speeds

3.4.1 C IV Blueshifts

Table 3.2 lists C IV blueshift velocities relative to $z_{\rm best}$ for every ERQ in our sample. We use the C IV emission-line wavelengths preferred by Hamann et al. (2017), namely, the midpoint in the fitted line profiles at their half-maximum heights, and a rest wavelength equal to the average for the doublet, 1549Å. Midpoint wavelengths are the same as the centroid for symmetric profiles, but they avoid possible asymmetries, blueshifted absorption or noise problems in the line wings that would affect the centroid values. Using the parameters reported in our study, it is possible to estimate the true C IV outflow speeds from the blueshifts of the line centroids, plus half of the measured FWHM, minus half of the C IV doublet separation (250 km s^{-1}). Here we report blueshifts of the C IV profile centroid to provide conservative approximations of outflow velocity, and compare them with other outflow measurements in Section 3.4.3.

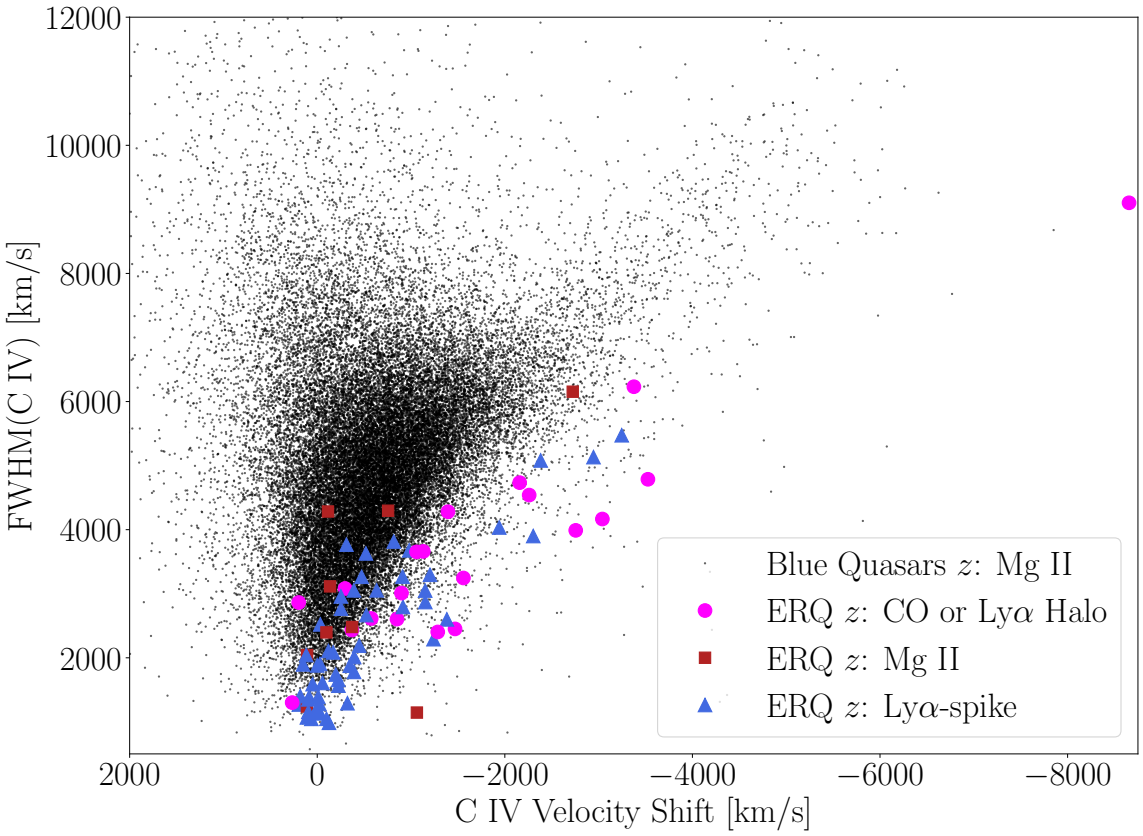

Figure 3.1: C IV FWHM vs velocity shift of ERQs with the best systemic redshift estimations and blue quasars. Pink dots indicates ERQs with systemic redshift estimates from either CO from ALMA or Lyα Halo from KCWI, red squares for ERQ redshifts estimates with Mg II from BOSS, and blue triangles for ERQ redshifts estimates from narrow Lyα from BOSS.

Figures 3.1 and 3.2 plot the C IV blueshifts versus FWHM(C IV) and REW(C IV), respectively, for ERQs compared to the normal blue quasar sample (Section 3.3). To provide clarity, REW measures the overall intensity of the emission profile in relation to the continuum. On the other hand, FWHM is width of the emission profile at the point where it is half its maximum height. Notice that the "Lyα-spike" sample of ERQs strongly favors narrow C IV emission lines (Figure 1). This is not representative of the ERQs overall in (Hamann et al. 2017, see also Section 2). However, if we consider only sources with FWHM(C IV) $\geq$ 2000 km s^{-1} in the Lyα-spike sample (orange triangles in Figure 3.2), the distribution of C IV blueshifts in that subsample, and its behavior in the 3-dimensional space that includes FWHM(C IV) and REW(C IV), closely resemble the ERQs in the CO and Lyα-halo samples (which all have FWHM(C IV) $\geq$ 2000 km s^{-1}).

Figure 3.3 and 3.4 compare the C IV blueshift and REW distributions, respectively, of ERQs to the blue quasar sample. The ERQs in these figures are from the combined sample of 74 sources with $z_{\rm best}$ from either CO, Lyα-halo, or a Lyα-spike with the additional constraint FWHM(C IV) $\geq$ 2000 km s^{-1}.

We can see from these figures that ERQs stand out from normal/blue quasars in several ways. First, ERQs have large C IV blueshifts at much larger REW(C IV) and somewhat smaller FWHM(C IV) than normal blue quasars (Figures 3.2 and 3.1, respectively). It is well known that large C IV blueshifts correlate strongly with small C IV REWs (Figure 3.2) and large FWHMs (Figure 3.1) in normal blue quasars (Richards et al. 2011; Coatman et al. 2016, 2019; Rankine et al. 2020; Temple et al. 2020, 2023; Gillette & Hamann 2023). The ERQs behave differently. They also exhibit a trend for larger blueshifts tied to larger FWHMs (seen in Figure 3.1) but, for any given blueshift,

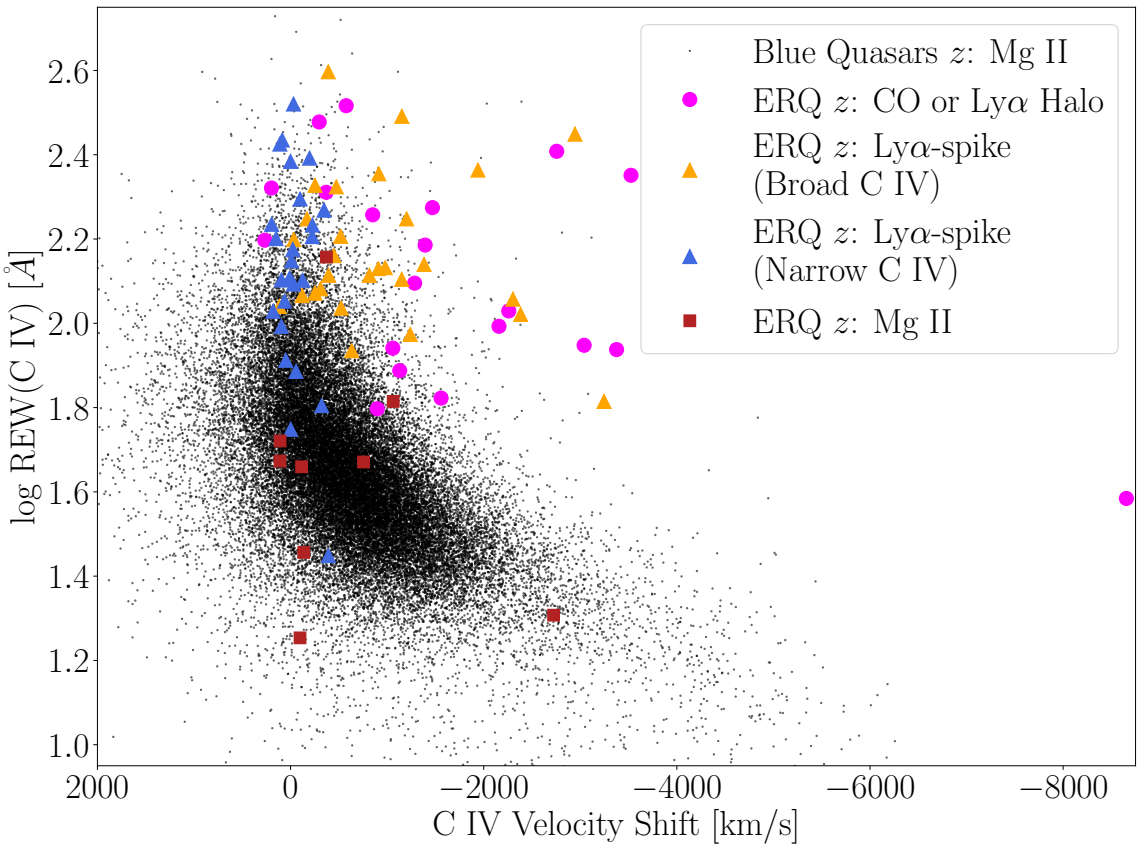

Figure 3.2: C IV REW vs velocity shift of ERQs with the best systemic redshift estimations and blue quasars. We use the same notation as Figure 3.1, except we separate the group with Lyα-spike measurements in to a broad-C IV (FWHM $\geq$2000 km s^{-1}) and narrow-C IV (FWHM <2000 km s^{-1}). Broad-C IV ERQs can show strongly blueshifted emission, while the narrow-C IV ERQs are typically more weakly blueshifted.

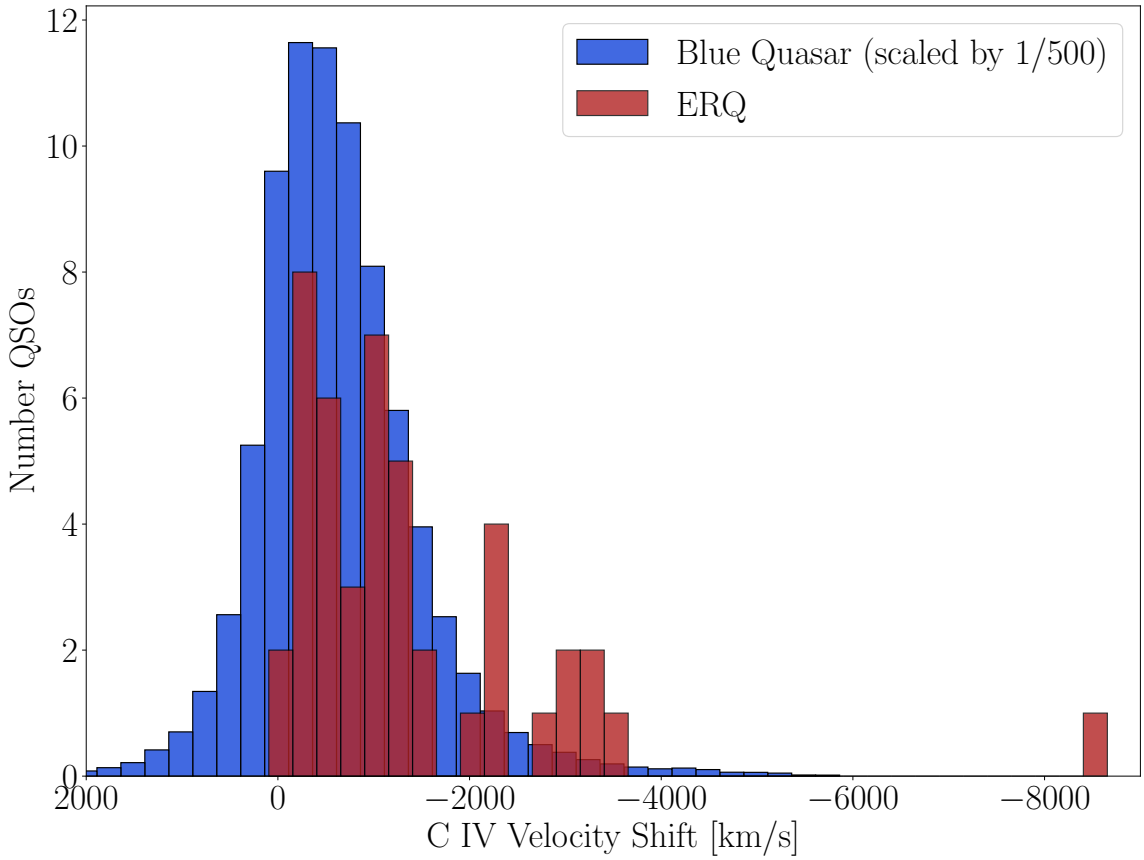

Figure 3.3: C IV velocity shifts for blue quasars and all ERQs that have reliable systemic redshift estimations from CO or Lyα, but excluding ERQs with narrow C IV profiles. We scale the much larger blue quasar distribution to compare with our sample. ERQs have a much higher fraction of high velocity C IV blueshifts than the normal blue quasar population.

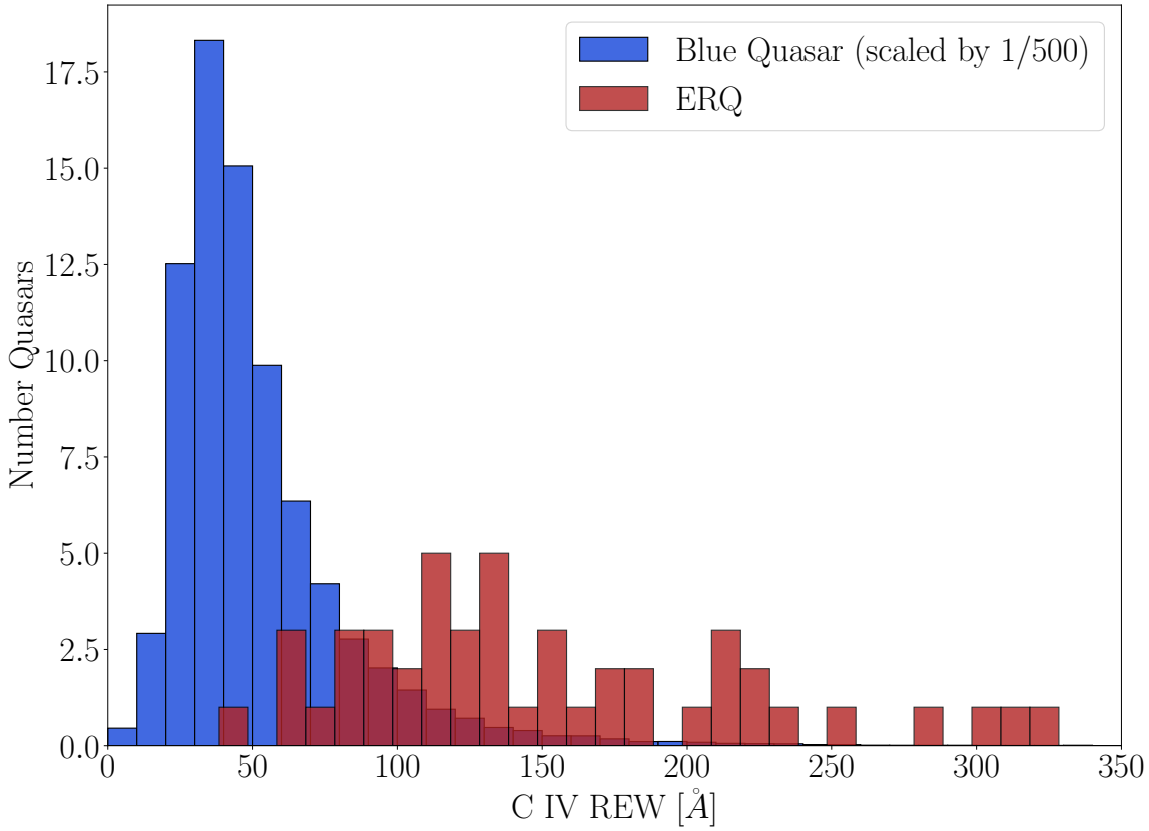

Figure 3.4: C IV REW for blue quasars and all ERQs that have reliable systemic redshift estimations from CO or Lyα, but excluding ERQs with narrow C IV profiles. We scale the much larger blue quasar distribution to compare with our sample. ERQs have considerably larger C IV REW than the normal blue quasar population.

the ERQ population is offset toward smaller FWHMs. J114508+574258 is the ERQ with the largest C IV blueshift, at −8655 km s^{-1} (Table 3.2), and has one of the smallest C IV REWs and largest FWHMs among all ERQs (Hamann et al. 2017). These properties are consistent with the direction of the trends in blue quasars. However, the C IV line in J114508+574258 is substantially broader and at least 4 times larger in REW than expected from trends in blue quasars (Figures 3.1 and 3.2). The ERQ samples overall are dramatically offset toward larger REWs than blue quasars, especially at large blueshifts. For example, for quasars with C IV blueshifts >2000 km s^{-1}, the average REW among ERQs is 124Å compared to only 24Å for the blue quasar sample.

Another important difference is the larger fraction of ERQs with large blueshifts compared to the blue quasar population (Figure 3.3). For example, if we consider all ERQs with well-measured $z_{\rm best}$ in our study (excluding only those based on Mg II), the fraction with blueshifts ≥2000 km s^{-1} is 12 out of 82, or 14.6 per cent. If we further exclude sources with FWHM(C IV) < 2000 km s^{-1} from our Lyα-spike sample, to be more representative of the majority of ERQs in Hamann et al. (2017), we find that 12 out of 54 (22.2 per cent) have blueshifts >2000 km s^{-1}. In contrast, only 0.2 per cent of the 39909 blue quasars in our comparison sample have blueshifts in this range. Richards et al. (2011) find a similar number, with only 21 (about 0.1 per cent) out of 15,779 quasars having blueshift ≥ 2000 km s^{-1} in their SDSS sample.

3.4.2 Revised [O III] Outflow Speeds

Table 1 provides recomputed [O III] outflow velocities, v_{98} when available, using our improved systemic redshifts. The [O III] data are from Perrotta et al. (2019) except for one quasar, J222307+085701, for which we present an [O III] measurement for the first time (from Lau et al. in prep.). Systemic redshifts used previously by Perrotta et al. (2019) are based on the best redshift

indicator available at that time, namely, either Hβ, low-ionization UV emission lines, or distinct narrow components in the [O III] (see their Table 1). Although not discussed explicitly by those authors, a few of the redshifts based on “low-ions" also considered a narrow core in the Lyα emission line, if one was present, similar to our analysis in Section 3.3.

Out of 15 ERQs with [O III] data from Perrotta et al. (2019) in our samples, 10 have revised redshifts different from the previous values by $\lesssim$200 km s^{-1}. This is generally good agreement for the purpose of studying high-speed quasar outflows. However, 4 have larger revised redshifts by $\gtrsim$500 km s^{-1} and 3 of those have larger revised redshifts by $\gtrsim$1000 km s^{-1}. This implies substantially larger outflow speeds than the previous estimates. In the 4 ERQs with the largest changes, the [O III] v_{98} values jumped from $-$2034 to $-$2534 km s^{-1} in J165202+172852, from $-$5480 to $-$6458 km s^{-1} in J232326$-$010033, from $-$2872 to $-$3877 km s^{-1} in J221524$-$005643, and from $-$5580 to $-$7026 km s^{-1} in J123241+091209 (cf. Table 1 here and Table 4 in Perrotta et al. 2019). All 4 of these ERQs with the largest shifts do not have narrow emission features in the quasar spectra, such that the previous redshift estimates came from Hβ or low-ionization UV emission lines.

Five quasars with CO, or Lyα, redshifts and low-ionization lines with have visibly obvious peak/centroids in Mg II or O I. We measure velocity shifts of these low-ionization lines with respect to the most reliable emission lines available. These ERQs include J113721+142728, J113834+473250, J134254+093059, J135557+144733, and J222307+085701, with respective relative velocities of $-$218, $-$62, 145, 278, and $-$285km s^{-1}. We discuss implications of these velocity shifts in Section 3.5.

One ERQ in our study with [O III] data from Perrotta et al. (2019), J083448+015921, has a revised redshift that is lower by 653 km s^{-1}. This revision changes the v_{98} estimate from -5079km s^{-1} in Perrotta et al. (2019) to -4426 km s^{-1} here. This is surprising because both the CO(4-3) emission line and the low-ionization UV lines in the quasar spectrum, notably O I λ1304, appear reasonably strong and well-measured. Perrotta et al. (2019) do not provide uncertainties on their redshift estimates, but a visual inspection suggests that they should be <200 km s^{-1} (at 3σ). The formal uncertainty in the CO measurement be Hamann et al. (2023 in prep.) is 7.3 km s^{-1}. It seems unlikely that the redshift difference is caused by infall in the low-ionization broad emission lines relative to the quasar. We conclude that it might be due to a real kinematic offset between the quasar and the molecular gas emitting CO(4-3) in the quasar's host galaxy.

3.4.3 CIV vs [OIII] Outflow Comparisons

Now we can compare the independently measured emission line velocities of C IV and [O III], using our improved systemic redshift values. However, a fundamental difference is that our C IV blueshift velocity is measured from the line profile center, and [O III] v_{98} is measured from the far blue wing of the profile.

The line emitting gas can be moving a wide range of angles relative to our line of sight. Consequently, the connection between observed blueshifts and outflow velocities relies on the specific model used. The blueshifts derived from C IV emission-line centroids serve as conservative lower limits of the true flow speeds. In simplified scenarios involving primarily radial motion and negligible additional line broadening factors, the most accurate estimate of outflow velocities is derived from the most significant blueshifts within the blue wing of the observed line profiles. A case in point is the utilization of the v_{98} parameter as demonstrated by Perrotta et al. (2019).

Figure 3.5 illustrates that large C IV REW and large [O III] v_{98} are both strongly tied to red i–$W3$ colors. These are fundamental peculiar properties of ERQs that set them apart form both normal blue quasars and other red quasar samples (see, Hamann et al. 2017; Perrotta et al. 2019, for more discussion).

Figure 3.6 shows that large [O III] v_{98} is strongly tied to red i–$W3$ color (as described in, Perrotta et al. 2019), with a weaker and more complex relationship to C IV blueshift. Notably, the largest C IV blueshifts (>2000 km s^{-1}) also have the largest [O III] v_{98} values. Although there are only four ERQs with C IV blueshifts >2000 km s^{-1} in the sample, they all have [O III] v_{98} > 5000 km s^{-1}. Three of theses are also among the reddest ERQs in the sample. At smaller C IV blueshifts (<2000 km s^{-1}) the relationship of [O III] v_{98} to C IV blueshift is much weaker. ERQs are offset from blue quasars in having much larger v_{98}, but only slightly larger C IV blueshifts on average.

As demonstrated in Figures 3.1 and 3.2 , there is a noticeable overlap in the range of C IV blueshifts between ERQs and typical blue quasars. However, two key distinctions emerge 1) a higher fraction of ERQs (bias-free) ERQs have high blueshifts compared to blue quasars, and 2) these occur at unusually large REWs, unlike high blueshifts in the normal blue quasar population.

3.5 Summary & Discussion

We present a sample of 82 ERQs that have improved estimates for redshift in order to better constrain outflow velocities from comparisons to previous line measurements. These comparisons are subject to selection biases (see Section 3.3.2), but overall we confirm ERQs have a higher incidence of large C IV blueshifts accompanied by large REWs and smaller line widths than blue

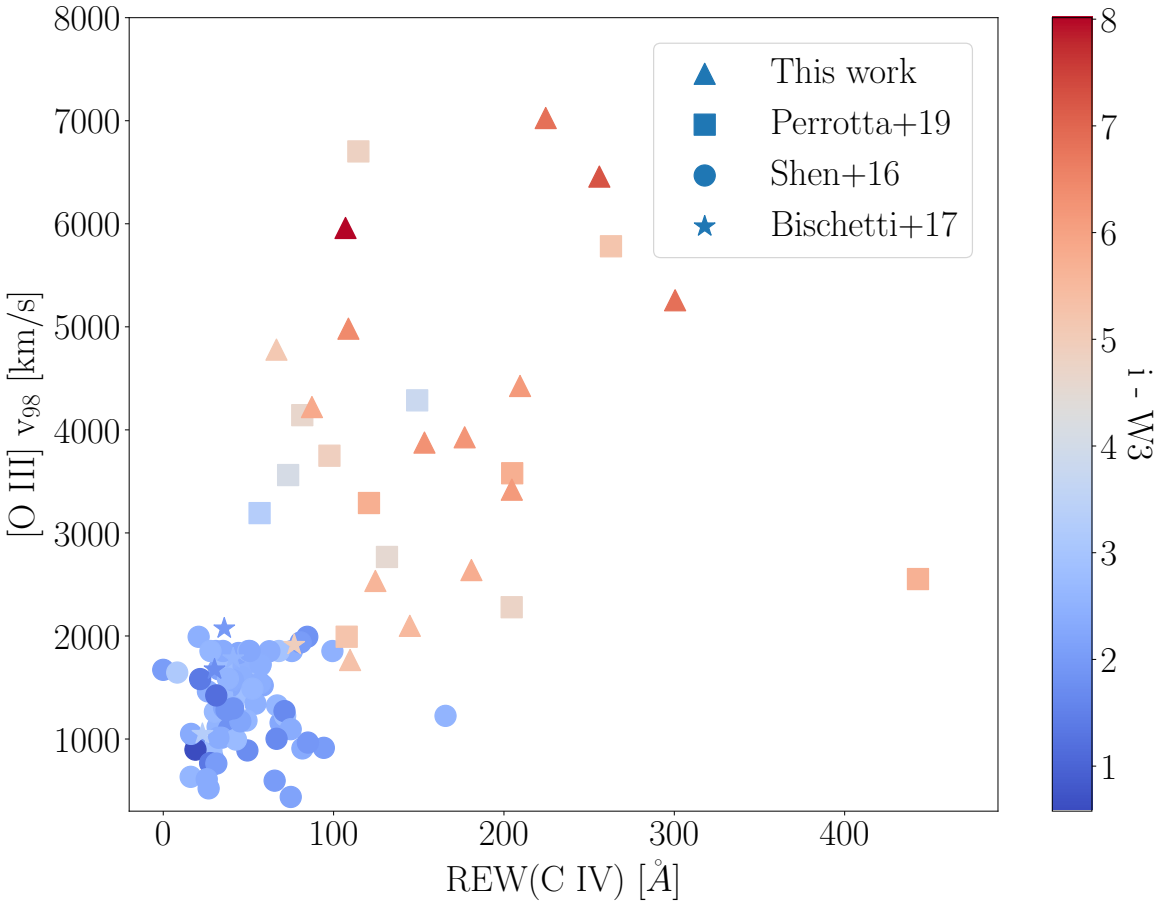

Figure 3.5: C IV REW vs [O III] v_{98} for 15 of our ERQs which have improved redshift measurements, and comparison blue quasar samples. We include the blue quasar samples that were used for comparison to ERQs in Perrotta et al. (2019), of similar redshift and luminosity to the ERQs. Triangle markers are the ERQs with revised redshift indicators, squares are ERQs from Perrotta et al. (2019) without revised redshifts, and finally circles and stars are normal blue quasars from Shen et al. (2016b) and Bischetti, M. et al. (2017) (discussion of the comparison quasars in Perrotta et al. 2019). All the symbols are color coded to indicate their i–$W3$ color.

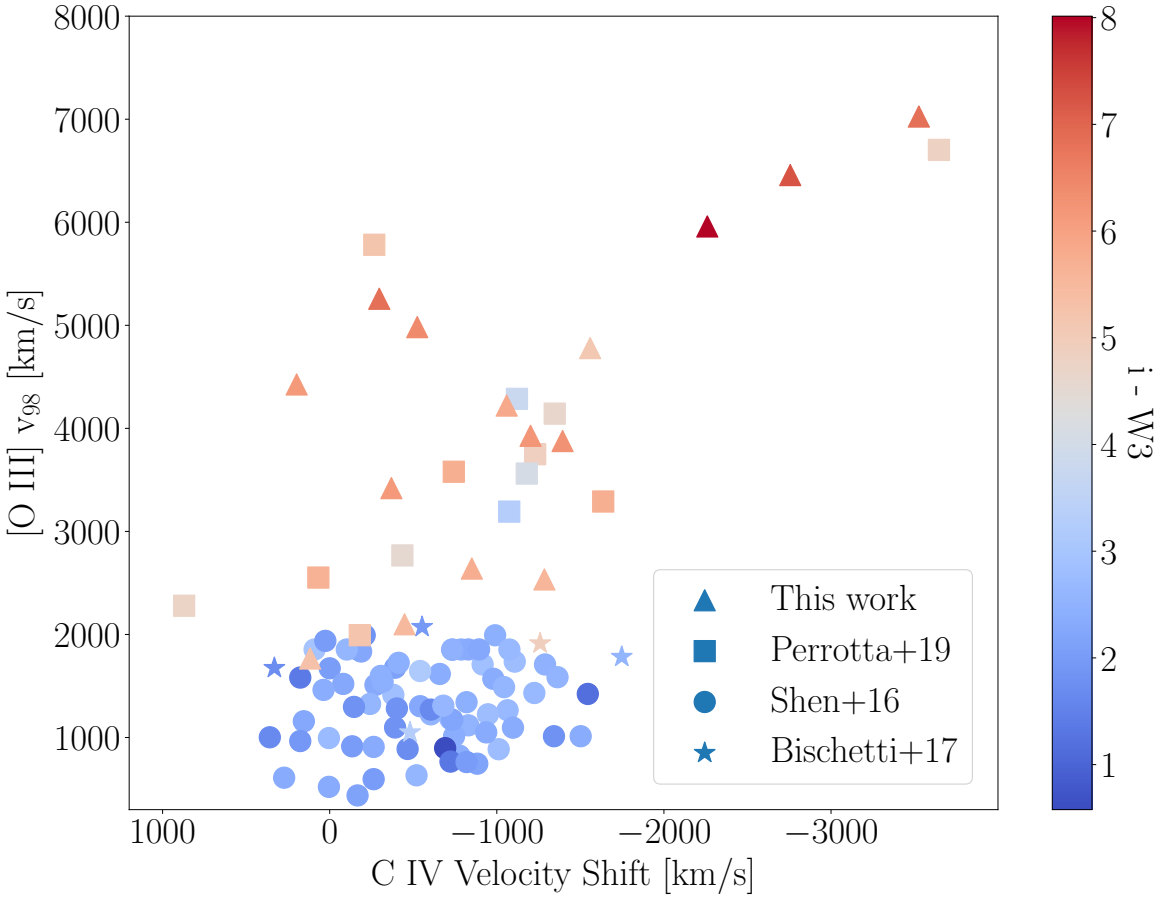

Figure 3.6: C IV blueshift velocity vs [O III] v_{98} for the same quasars, markers, and colors as in Figure 3.5. There are four ERQs with exceptionally fast [O III] v_{98} (>5000 km s^{-1}) and large C IV blueshift velocity (>2000 km s^{-1}).

quasars. Blueshifts >2000 km s^{-1} are present in 12/54 (22.2 per cent) of ERQs with the most robust z indicators. ERQs with blueshifts >2000 km s^{-1} are substantially offset in C IV REW and FWHM from typical blue quasars in the same velocity range, with ERQ averages of REW = 124Å and FWHM = 5274km s^{-1}, compared to blue quasar averages REW = 24Å and FWHM = 6973km s^{-1}.

Our systemic redshifts compared to the previous estimates by Perrotta et al. (2019) already identifies 4 out of 15 ERQs in our sample with blueshifts in their Hβ and low-ionization UV lines ranging from -500 to -1500 km s^{-1}. This is a lower limit to the true fraction of ERQs with large blueshifts in these lines because some of the estimates in Perrotta et al. (2019) relied on narrow emission spikes in [O III], which agree well with our redshift estimates because they also form in extended environments around the quasars. Thus it appears that a significant fraction of ERQs have large blueshifts throughout their broad emission-line regions. This property of ERQs differs from the situation in normal blue quasars, where fast outflows in the broad emission-line regions are both much rarer than ERQs and primarily limited to the high-ionization gas emissions (e.g., C IV, Richards et al. 2011; Coatman et al. 2019; Rankine et al. 2020).

The extreme outflows in ERQs could explain certain aspects of their spectral traits. For instance, these outflows might contribute to the significant C IV REWs. This could be due to broader emission-line regions with greater coverage, resulting in more reprocessing of continuum light originating from the central quasars. Additionally, the distinctive C IV profiles lacking prominent wings could be a result of their formation predominantly within outflows, rather than in gas near the inner accretion disk as typically found in virialized conditions (Hamann et al. 2017). It is also interesting to consider that the exceptionally fast [O III] winds in ERQs might be an outer, lower-density extension to the broad emission-line outflows.

It remains unclear why ERQs tend to have faster/more powerful outflows than normal blue quasars, but there are two factors that might contribute. One is higher Eddington ratios, which can provide a greater radiative driving force compared to gravity. Another is softer UV continuum, where the weaker far-UV flux helps to maintain moderate ionization levels and substantial opacities in the outflow for radiative driving to be seen in the near-UV. There is strong observational evidence for both of these factors leading to faster outflows in normal blue quasars. For example, the He II λ1640 emission-line REW roughly measures the ionizing flux at energies $h\nu > 54$ eV relative to the near-UV continuum, on which the line sits, inversely correlates with larger C IV emission-line blueshifts (Richards et al. 2011; Rankine et al. 2020; Temple et al. 2023; Gillette & Hamann 2023) and faster C IV broad absorption-line (BAL) outflows (Baskin et al. 2013; Hamann et al. 2018; Rankine et al. 2020). This inverse relation is consistent with softer UV spectra playing an important role in outflows, and is indicated in hyper-luminous blue quasars (Vietri, G. et al. 2018). It has been shown that larger Eddington ratios can also correlate with larger C IV blueshifts (Baskin & Laor 2005; Coatman et al. 2016; Rankine et al. 2020; Temple et al. 2023; Gillette & Hamann 2023).

More work is needed to determine if these trends also apply to ERQs and, moreover, if their extreme outflows result from them being at an extreme end of the trends found in blue quasars (e.g., with larger Eddington ratios or softer UV continua). Previous studies have found no significant trend in [O III] outflow speed with Eddington ratio (as measured from Hβ) among ERQs (see Figure 7 in Perrotta et al. 2019). Unfortunately, there are unique obstacles to testing these trends for ERQs. One is that their emission-line REWs are anomalously large, and He II is at least partly involved in that tendency (see Figure 8 in Hamann et al. 2017), which could confuse the relationship of this line with larger C IV blueshifts. Another challenge is that Eddington ratios require black hole mass estimates,

which are derived normally from one of the broad emission lines like Mg II. We have shown above that ERQ lines like Mg II could have kinematics dominated by outflows, instead of virial motions in the local gravity, and thus making them unreliable for black hole mass determinations. Furthermore, obtaining bolometric luminosities necessary for Eddington ratios poses a greater challenge for ERQs compared to normal blue quasars, because their intrinsic SEDs are potentially atypical. Nonetheless, we confirm the extreme properties of ERQ outflows, which motivates future efforts to understand what is the cause of their extreme nature and potential impacts on the host galaxy.

Chapter 4

Paper III: BOSS Quasar Outflows Traced by C IV

4.1 Abstract

We investigate possible factors that drive fast quasar outflows using a sample of 39,249 quasars at median redshift $\langle z \rangle \approx 2.17$. Unique to this study, the quasar redshifts are re-measured based on the Mg II emission line, allowing for exploration of unprecedented outflow velocities (>6000 km s^{-1}) while maintaining statistical significance and uniformity. We measure reliable C IV blueshifts for 1178 quasars with velocities >2500 km s^{-1}. From those, 255(13) quasars have blueshifts above 4000(6000) km s^{-1}, with the highest C IV velocity $\approx$ 7000 km s^{-1}. Several correlations are observed, where higher C IV blueshifts in general are in quasars with broader, weaker C IV emission profiles, weak He II emission, larger Eddington ratios, and bluer UV continuum slope across the rest-frame UV to Near-IR. Analysis reveals two primary factors contributing to faster

outflows: higher Eddington ratios, and softer far-UV continuum (hν >54.4 eV). We find supporting evidence that radiative line-driving may generate extreme outflow velocities, influenced by multiple factors as suggested by the aforementioned correlations. This evidence highlights the importance of considering a multi-dimensional parameter space in future studies when analyzing large C IV blueshifts to determine the fundamental causes of outflows.

4.2 Introduction

High-z quasars are associated with formation and growth of massive galaxies, and it is believed that the feedback from these quasars plays a crucial role in regulating both galaxy growth and star formation processes (Hopkins et al. 2008, 2016; Wylezalek & Zakamska 2016; Veilleux et al. 2016; Rupke et al. 2017; Baron et al. 2017; Vayner et al. 2021). However, the physical nature and driving mechanism(s) of quasar outflows remain poorly understood. We need, in particular, better empirical constraints on the quasar properties and physical conditions that correlate with a higher incidence, greater speeds, or more powerful outflows.

Quasar outflows are often studied via blueshifted broad absorption lines (BALs) and their narrower cousins, mini-BALs, in rest-frame UV spectra (Weymann et al. 1991; Hamann & Sabra 2004; Baskin et al. 2013; Muzahid et al. 2013; Hamann et al. 2018; Chen et al. 2019). Another approach is to use the blueshifts in their broad emission-lines (BELs). These strategies are complementary, but the BELs offer unique advantages. One is that the location of BEL regions is known from reverb studies to be unambiguously near the central engines, at radial distances of roughly 0.01 to 0.1 pc in luminous quasars (Netzer 2020, and references therein). Thus, emission lines provide specific constraints on quasar outflow models. Another advantage is that emission-line

studies are less sensitive to orientation and time-dependent effects than absorption lines, which can only measure the gas/outflow structures that happen to lie along our line of sight to the continuum source during the observing epoch. Specific values of emission blueshift can vary depending on the sample and selection criteria, previous studies have found typical blueshifts ranging from a few thousand km s^{-1} in BELs, to tens of thousands of km s^{-1} for BALs (e.g., Richards et al. 2011; Coatman et al. 2019; Temple et al. 2020; Rankine et al. 2020).

We do not know the geometry with certainty, but strongly blueshifted profiles from high ionization lines suggest the emission comes from a wind that is moving toward us, with the receding component blocked by the optically thick accretion disk. Intermediate and lower ionization lines may be emitted by gas in the accretion disk atmosphere, or a low-velocity base of the wind (Leighly & Moore 2004; Leighly 2004; Casebeer et al. 2006; Richards et al. 2011; Hamann et al. 2017; Rankine et al. 2020; Temple et al. 2023).

Investigating these line shifts require accurate systemic redshift of the quasar. In many quasar blueshift studies the systemic redshift is estimated by fitting of multiple emission lines simultaneously, which are assumed to be at or near their rest wavelength (Richards et al. 2011; Coatman et al. 2016, 2019; Rankine et al. 2020; Temple et al. 2020, 2023). Many studies estimate redshift using emission-lines or emission-templates that may include higher ion lines. High ion lines like C IV λ1549 can be blueshifted from systemic by several hundreds of km s^{-1} (Gaskell 1982; Richards et al. 2002). The best indicators are narrow emission lines arising from the extended host galaxies and halo environments. Efforts have been undertaken to establish accurate redshifts for select quasar populations in order to better constrain extreme outflow velocities (e.g., Gillette et al. 2023a).

Low-ion BELs such as Mg II, O I λ1304, and C II λ1335 are also generally good indicators of quasar redshifts, e.g., with small or negligible offsets relative to narrow [O II] and [O III] emission lines. Mg II is estimated to be near the systemic redshift when compared to these other lines in high redshift quasars (Richards et al. 2002), and is much more reliable than high-ion lines like C IV. A mean shift between Mg II - C IV has been shown of ~920 ± 750 km s^{-1} (Ref. appendix in, Shen et al. 2007).

For this work, we present a sample of Mg II emission-line measurements for 39,249 quasars from BOSS DR12. We then use these data to study the blueshifts in the C IV BEL compared to a wide variety of other quasar properties that can be measured or derived from this dataset. This study differs from previous work by determining redshifts only from careful fitting of the Mg II line, allowing us to explore an unprecedented range of outflow velocities uniformly, and maintain a statistically significant sample size. We can then focus more sharply on trends in other lines and quasar properties that correlate with blueshifts.

In this paper we analyze blueshifted emissions of C IV, and compare their emission profiles and UV features to understand what correlates with strong outflows. It is organized as follows. Section 2 describes criteria for selecting quasars from catalogue spectra. Section 3 describes our methods and measurements of blueshift, Mg II line features, and black hole mass. Section 4 describes correlations in measured parameters of UV emission features, such as blueshift, emission line widths, Eddington ratio, and spectral shape. Section 5 we discuss implications for quasar outflows. Section 6 concludes the paper. Throughout this paper we adopt a Λ-CDM cosmology with H_0 = 69.6 km s^{-1} Mpc^{-1}, $\Omega_{\rm M}$ = 0.286 and Ω_Λ = 0.714, as adopted by the online cosmology calculator developed by Wright (2006). All magnitudes are on the AB system. Reported wavelengths are in vacuum and in the heliocentric frame.

4.3 Quasar Samples and Data Sets

We started from a C IV emission-line sample of 173,636 quasars, measured by (Hamann et al. 2017), from the Baryon Oscillations Survey (BOSS) from the Sloan Digital Sky Survey Data Release 12 (hereafter DR12Q; Pâris et al. 2014, 2017b). We limit our study to Type 1 sources based on the crude distinction FWHM(C IV) $\geq$ 2000 km s^{-1} following previous studies by Alexandroff et al. (2013) and Ross et al. (2015). This was done to avoid contamination by Type 2 quasars unless C IV FWHM is explicitly used for comparison to other parameters. Sample selection criteria and quasar totals are summarized in Table 4.1. Other subsamples after the "full" sample use additional constraints as described in the sections noted. Figure 4.1 shows redshift and luminosity distributions. To ensure C IV and Mg II spectral coverage we are limited to the redshift range $1.50 \leq z \leq 2.46$. By our quality standards, outlines in Section 4.4.1, we have 39,249 quasars with a median redshift of $\langle z \rangle \approx 2.17$.

Sample name	Selection criteria	Number	Section ref.
DR12Q	-	297,301	
Hamann+17	$2.0 < z_e < 3.4$ i mag in DR12Q well-measured C IV	173,636	
Full Sample	C IV FWHM $\geq$2000 km s^{-1} well-measured Mg II	39,249	4.3
BH Mass	well-measured Mg II wings	38,966	4.4.3, 4.5.3
Composite Sample	3.1e45 $< L_{\rm bol} <$ 2.5e46 erg s^{-1}	29,460	4.5.2
Color Sample	r & z mag in DR12Q $1.8 < z_e < 3.4$	32,365	4.5.4
	$W1$-detected cc_flags = 0000	25,134	4.5.4
High blueshift C IV	$>$ 4,000 km s^{-1} $>$ 6,000 km s^{-1}	255 13	4.5.5

Table 4.1: Selection criteria and total quasars for our full quasar sample, and subsamples.

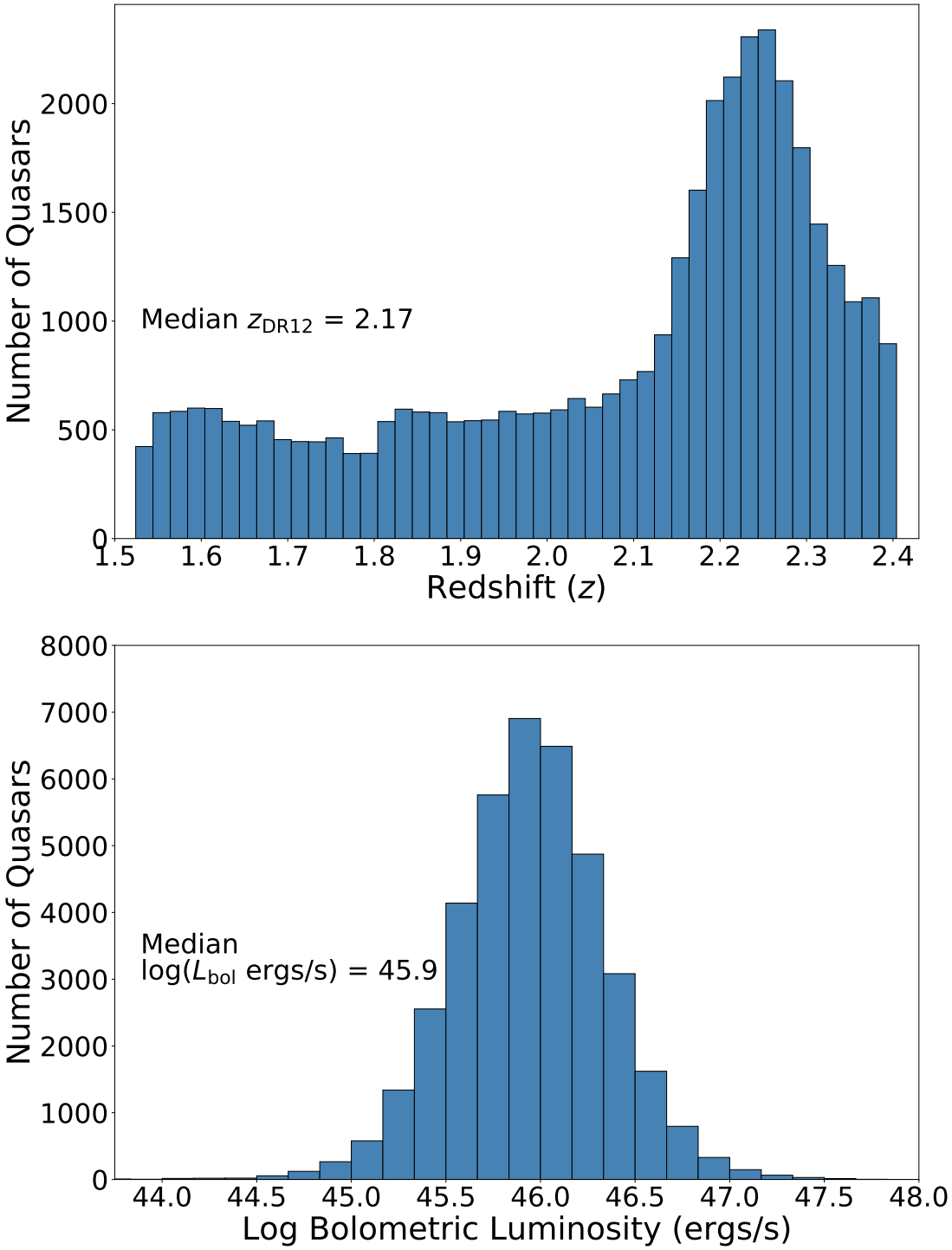

Figure 4.1: Redshifts and computed Bolometric luminosities for our full sample. *Top:* Redshift distribution as provided from DR12Q. *Bottom:* Bolometric luminosities computed from monochromatic luminosities as described in Section 4.4.3.

For more accurate luminosity estimation from BOSS, a flux correction for atmospheric differential refraction was applied from Margala et al. (2016) when available, and otherwise applied a correction from Harris et al. (2016). We computed monochromatic luminosity (λL_λ) using a fitted power law continuum local to Mg II near 2800Å. This local continuum was extrapolated for the monochromatic flux at 3000Åto compute $L(3000) = 4\pi D_L^2 \lambda f_\lambda$. Where D_L is the luminosity distance, and f_λ is the flux at wavelength lam. Bolometric luminosity ($L_{\rm bol}$) was determined using a monochromatic Bolometric correction factor $k_{\rm bol} \times L(3000) = L_{\rm bol}$, where $k_{\rm bol} = 25 \times \left[L(3000)/10^{42}\ {\rm erg\ s^{-1}}\right]^{-0.2}$. This method of correction factor makes considerations for a luminosity-dependent spectral energy distribution over a broad range of black hole masses, accretion rates, and spin, calibrated by Netzer (2019). We did not do a reddening correction for luminosity, which we note in our analysis in Section 4.5.4.

4.4 Measurements

In this study we use a dynamic fitting algorithm on every spectra in the Hamann et al. (2017) set to measure line-emission features in the rest frame UV continuum, even for low signal to noise. Specifically, we used the Mg II emission-line peaks for systemic redshift, after we applied several Gaussian models for fitting the emission profile, and subtracted a broadened Fe II template. We assume the Mg II doublet emission is one to one ratio, and the emission cloud itself is optically thick ($\tau \gg 1$). We did not use BOSS catalogue signal to noise values during fitting, because they did not accurately represent the quality of spectral detections near C IV and Mg II.

4.4.1 Continuum and Line Fits

The first step is an algorithm that searches the spectrum for narrow spikes above or below the spectra caused by cosmic rays, noise, or other anomalies. These spikes are removed by interpolation from adjacent pixels. We applied a spectral flux correction from Margala et al. (2016) when available, and otherwise applied a correction from Harris et al. (2016).

Next we perform an initial preliminary fit to make a rough redshift correction in cases where the BOSS pipeline redshift is too far offset from where we expect Mg II emission. We dynamically adjust the size of continuum flux sampled from ~2160 to 3120Å to avoid anomalous features in the spectra when fitting the continuum or emission lines (e.g. fringing as Mg II is further redshifted to the end of the spectrograph at larger z). We subtracted a modified Fe II template to remove emission local to Mg II (template provided through private correspondence with Yue Shen, Shen et al. 2016b). The template emission is from a theoretical model by Salviander et al. (2007) scaled to match the empirical template from Vestergaard & Wilkes (2001) but includes non-zero flux 2780-2830Å under Mg II line emission.

After defining the preliminary continuum, we we mask sharp absorption and make a preliminary single Gaussian fit, for a rough correction to the DR12Q catalogue redshift. We also used the preliminary fit's FWHM as a proxy measurement of Fe II emission-line broadening. Next we perform the broad absorption checks as before. Again, the Fe II template is scaled, but before final subtraction the template is broadened according to our preliminary-FWHM of the Mg II profile.

Once we establish a continuum, we check for strong broad absorption with the median fluxes in wavelength intervals 2310-2360Å and 2550-2580Å because broad absorption in these windows by Fe II is always accompanied by absorption in Mg II. If broad absorption was found, it was flagged for rejection.

Finally, for fitting Mg II $\lambda\lambda$2796,2804 line emission we ignore the doublet separation, instead using the mean. We found a robust iterative procedure that begins with a two-component Gaussian model, which yield good results with a minimum of free parameters (similar to Hamann et al. 2017). If a two-component fit that does not yield physically reasonable profile, or were too

similar in shape, we instead fit using a single Gaussian profile. A final peak wavelength measurement is performed with an additional Gaussian fit to the top two thirds of the fitted Mg II profile, to mitigate wing asymmetry in the lower one third.

In order to ensure quality spectra measurements we chose a variety of quality standards after fitting, with which to throw out spectra dominated by noise and otherwise "bad" fits. We vetted the final sample with the following quality criteria.

A minimum spectral signal-to-noise ratio is chosen as well as our own defined quality standards, such as requiring C IV and Mg II lines to be well measured based on their fit signal-to-noise >4 in both REW and FWHM. After fitting, we required quality flags for each spectra that indicate no significant problem in the Mg II emission-line or continuum fit occurred, and similarly good quality flags from the C IV measurements sample. We also placed conservative upper limits on both FWHMs to ensure the algorithm did not incorrectly fit to the continuum instead of the emission-line with our model, and obviously nonphysical. In order to further mitigate incorrect emission-fitting, and allow our general findings in the full sample to be more robust, we have chosen to ignore any spectra containing Broad Absorption Lines (BALs). Spectra were rejected for BALs by the visual inspection flag present in DR12Q, and the Balnicity Index (BI) must be `bi_civ > 0.0` and `bi_civ < 1000.0`. Any masking of absorption spikes done to properly fit an emission-line in the Mg II emission range must not be a significant fraction of the emission width, and the Mg II emission-line peak height must have a good signal to noise. We rejected fits when emission around the fitted Mg II profile has a standard deviation >0.75 to further limit the impact of noise when fitting the upper two-thirds of the Mg II emission profile. For Fe II template subtraction quality

criteria, we rejected the spectra if the intensity of Fe II was comparable to the peak intensity of Mg II line-emission. This criteria is to limit the bias introduced by the template in our Mg II profile fit.

Visual inspections of several thousand of the remaining spectra indicate that the continuum and Mg II line fits are generally excellent. We specifically examined results at the extremes of broad and narrow FWHMs, large and small REWs, strong BALs or other broad absorption that might overlap with the Mg II emission-line profiles, and spectra with low SNRs in the continuum. The most common problem is fits that underestimate the line peak height and thus overestimate the FWHMs for observed lines that have a strong narrow core on top of much broader wings.

4.4.2 Measured Quantities and Blueshifts

We measured C IV blueshift by comparing the emission redshift of Mg II from our fitting to the emission redshift of C IV λ1548,1551 measured by Hamann et al. (2017). We used the top two thirds fit of Mg II emission as the improved systemic redshift. Then we used the C IV measurement of the midpoint at half the fitted profile height as the emission velocity shifted from rest C IV. We use negative values to correspond to inflow away from the observer, and positive values as blueshifts, outflowing towards the observer. We visually inspected all ~250 cases with blueshifts >4000 km s^{-1} to ensure their validity.

For our full sample we obtained measurements for 39,249 quasars, eliminating those with strong BALs and poor data. From these, we measured a multitude of emission line properties which are supplemented by C IV measured quantities from Hamann et al. (2017). For Mg II we measured the rest-equivalent width (REW), full width at half maximum (FWHM), second moment line-dispersion (σ), and centroid redshift. From the continuum fit we took the monochromatic flux (f_{3000}) for computing a monochromatic luminosity to approximate Bolometric luminosity. We measured the Mg II emission profile with both FWHM and σ, described in Peterson et al. (2004).

4.4.3 Black Hole Masses

We computed estimates of quasar black hole mass, assuming that the Mg II broad-line region (BLR) has virialized. We consider estimates using both Mg II FWHM and σ, because spectra quality of high-z AGNs can often be insufficient for measuring line dispersion of broad lines (Peterson et al. 2004; Shen et al. 2008; Wang et al. 2009; Shen & Liu 2012; Woo et al. 2018). Using the continuum luminosity as a proxy for BLR radius and the broad line width or line dispersion for the virial velocity we estimated virial mass with,

$$\log\left(\frac{M_{\rm BH,vir}}{M_\odot}\right) = \alpha + \beta\,\log\left(\frac{\rm FWHM}{10^3\ \rm km/s}\right) + \gamma\,\log\left(\frac{\lambda L_\lambda}{10^{44}\ \rm erg/s}\right),$$

where estimator values $\alpha_{\rm FWHM} = 7.02 \pm 0.04$ or $\alpha_\sigma = 7.56 \pm 0.03$, $\beta_{\rm FWHM,\sigma} = 2.00$, and $\gamma_{\rm FWHM,\sigma} = 0.50$ are recommended from (see Table 3 in Woo et al. 2018) for using L_{3000}. These values were adopted by calibrated UV mass estimators comparing dispersion of Hβ to Mg II. There they found continuum luminosity at 3000Å provided better calibration than the line luminosity of Mg II. After making quality cuts based on good Mg II signal to noise we have a total of 38,966 quasars (ref. Table 4.1). Comparison distributions for either method are shown in Figure 4.4 and Figure 4.11. FWHM tends to overestimate large widths, and underestimate the narrow widths. Most of our fits use single Gaussians, and therefore driven by FWHM. In this work, we present results for both FWHM and σ, but opt to use FWHM to parameterize line width.

4.5 Results & Analysis

For a basis in presenting numbers of quasars, etc., we present distributions of our measured parameters. Figures 4.2 & 4.3 present distributions in redshift, Bolometric Luminosity ($L_{\rm bol}$), REW, FWHM, and σ for both C IV and Mg II.

Figure 4.2 shows the distributions of line strengths and widths. C IV has slightly larger REW than Mg II, but have similar distributions. In the general population with broad C IV emission FWHM has similar distributions for C IV and Mg II. There are many examples of quasars with FWHM(C IV) and FWHM(Mg II) both being large or small but there may be extreme cases where differences in width are exacerbated, and may correlate with other quasar characteristics. The last panel shows our integrated line dispersion for C IV and Mg II. The distributions appear similar, but there is a clear offset between the two emission lines.

Figure 4.3 displays distributions of line strength and width of C IV and Mg II. Emission line strengths generally appear to correlate in REW(C IV) and REW(Mg II), but flatter than one to one. However, spectra showing strong C IV emission generally have weaker Mg II by at least 0.2dex. Emission line widths between C IV and Mg II FWHM are generally uncorrelated. Plotting Mg II FWHM against σ, we compare the general distribution to robustly measured quasars at lower redshifts by Woo et al. (2018), and show overlap in line widths. We can see in the distribution of our sample that profiles fit with a double-Gaussian (25 percent) extend to larger values of σ than those fit with a single-Gaussian.

Our broad goal is to understand what physical or evolutionary properties of quasars lead to large BEL blueshifts, and fast powerful outflows capable of feedback. We first quantify the C IV blueshifts, and then investigate other quasar properties and physical conditions for empirical relationships with blueshift.

4.5.1 Blueshifts Across the Sample

Figure 4.5 shows distributions of Mg II REW, C IV REW and FWHM vs blueshift. There are several quasars that appear to show redshifted C IV. These redshifts may be due to the uncertainties and relative motions of C IV and Mg II, and not high velocity inflow. We visually inspected all 255 cases with measured blueshifts greater than 4000 km s^{-1}. We were concerned that these extreme cases have broad and weak C IV lines (see Section 4.6.3 below) that might be poorly or incorrectly measured. However, the vast majority of these high blueshift cases were found to have good fits. Most of the sample resides between blueshifts of 0 and 1500 km s^{-1}, with a median C IV blueshift of about 530 km s^{-1}. We measure reliable blueshifts for 1178 quasars with velocities >2500 km s^{-1}. From those, 255 quasars with blueshifts above 4000 km s^{-1}, 13 above 6000 km s^{-1}, and the highest well-measured C IV velocity $\sim$ 7000 km s^{-1}. Figures of C IV REW vs its blueshift has become common in the literature (e.g., Richards et al. 2011; Coatman et al. 2016, 2019; Rankine et al. 2020; Temple et al. 2020, 2023). This work differs in that we exclusively use the Mg II emission line as the proxy measurement for systemic redshift, where others use catalogue redshifts from template fitting or a combination of low-ionization lines, which may include Mg II. Our distribution is in broad agreement with other studies, and have comparable sample sizes, but we extend to further extremes in the C IV parameter space of line strength/weakness and blueshift. The top two panels of Figure 4.5 show not only that C IV REWs are small at large blueshifts, but they are small relative to the

low-ion line Mg II. The bottom panel shows that C IV lines can be broad at any velocity shift, but at large blueshifts they are almost exclusively broad.

Figure 4.6 is identical to Figure 4.5, with subdivisions in to boxes to further inspect local median quantities across the parameter space. This partitioning allows us to vary C IV REW and blueshift independently, and show how medians of other measured quasar properties correlate. Figure 4.7 displays median values of Bolometric luminosity, and several median properties for quasars in each box. This figure more quantitatively shows the blueshift trends with C IV line strength and width. The vertical trend of larger C IV REW with smaller $L_{\rm bol}$ is the Baldwin Effect (Baldwin 1977), but there also appears to be a weak trend for larger $L_{\rm bol}$ with larger blueshifts (see Section 4.5.3). Median C IV FWHM of each box is uniform in weak blueshifts, and dramatically increases for large blueshift quasars. At high blueshifts (>3000 km s^{-1}), C IV rarely exhibits line strength REW above 40 Å. In this high blueshift regime C IV becomes almost always broad, with median FWHM > 7000 km s^{-1}, and is broad relative to Mg II (median FWHM about 3700 km s^{-1}). Median Eddington ratio in each box also appears to increase with C IV blueshift. Median strengths of Fe II relative to the continuum, which is used to subtract the Fe II complex, appear stronger for large blueshift.

We further inspect other color-coded versions of this figure, and discuss extinction effects on luminosity due to quasar reddening, in Section 4.5.4. We inspect median composite spectre to confirm trends in median quantities with blueshift in Section 4.5.2.

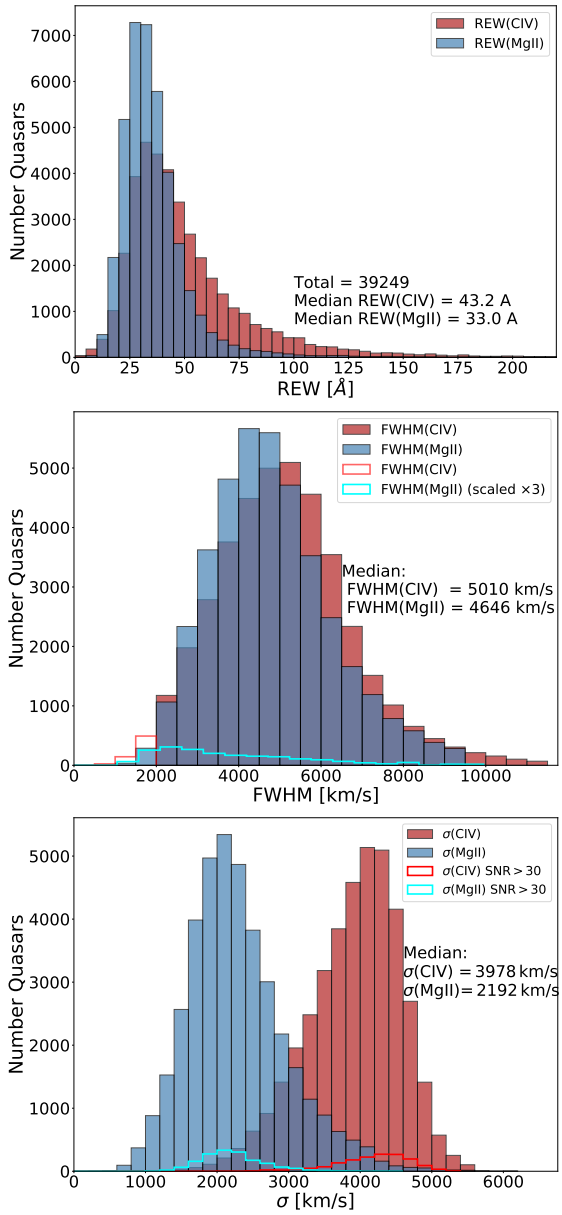

Figure 4.2: Distributions of measured quantities for our sample. *Top:* REW distributions the full sample of quasars for both C IV (blue histogram) and Mg II (red histogram) emission lines. *Middle:* FWHM distributions for all quasars for both C IV (red histograms) and Mg II (blue histograms) emission lines. Distinction between broad and narrow line quasars is made by C IV emission FWHM, where broad emission are defined by C IV FWHM $\geq$2000 km s^{-1} (solid red histogram), and narrow as C IV FWHM <2000 km s^{-1} (outlined red histogram). The solid blue histogram shows Mg II FWHM for quasars with C IV FWHM $\geq$ 2000 km s^{-1}, and the outlined cyan histogram shows Mg II FWHM for quasars with C IV FWHM < 2000 km s^{-1}. *Bottom:* σ distribution for single and linked-Gaussian profiles used in our full sample.

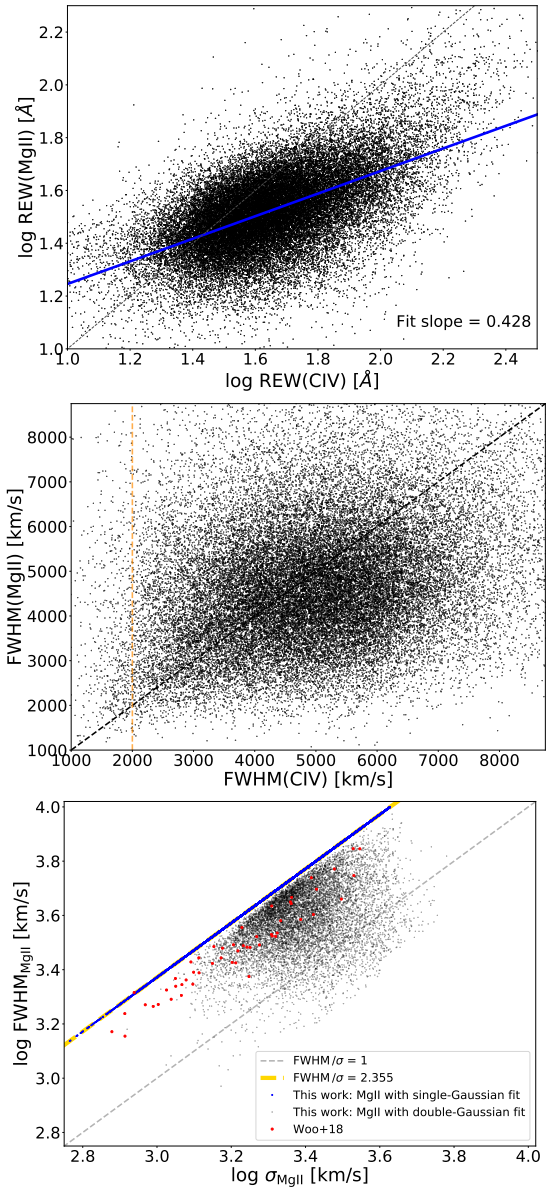

Figure 4.3: Measured quantities of emission lines plotted against one another. *Top:* REW of C IV vs Mg II of the full sample of quasars. *Middle:* The FWHM ratio of C IV vs Mg II of all quasars in our full sample. The yellow dashed line is our cutoff for broad C IV emission quasars. *Bottom:* Log FWHM(Mg II) vs log σ(Mg II) of all broad C IV emission quasars in our full sample. Black points are our linked-gaussian profile fits, blue points are our single-gaussian profile fits, and the yellow dashed line highlights the relationship of FWHM to σ for a Gaussian emission-profile. About 75 percent of the quasars in the sample are measured with single-Gaussians that yield FWHM$/\sigma$ = 2.355. We impose additional quality cuts to fits with linked-gaussian fits to omit large wing profiles of low signal to noise ratio. There is some overlap between our sample and that of Woo et al. (2018), despite their sample being near $z \approx 0.3-0.6$. All panels show one to one as a grey dashed line.

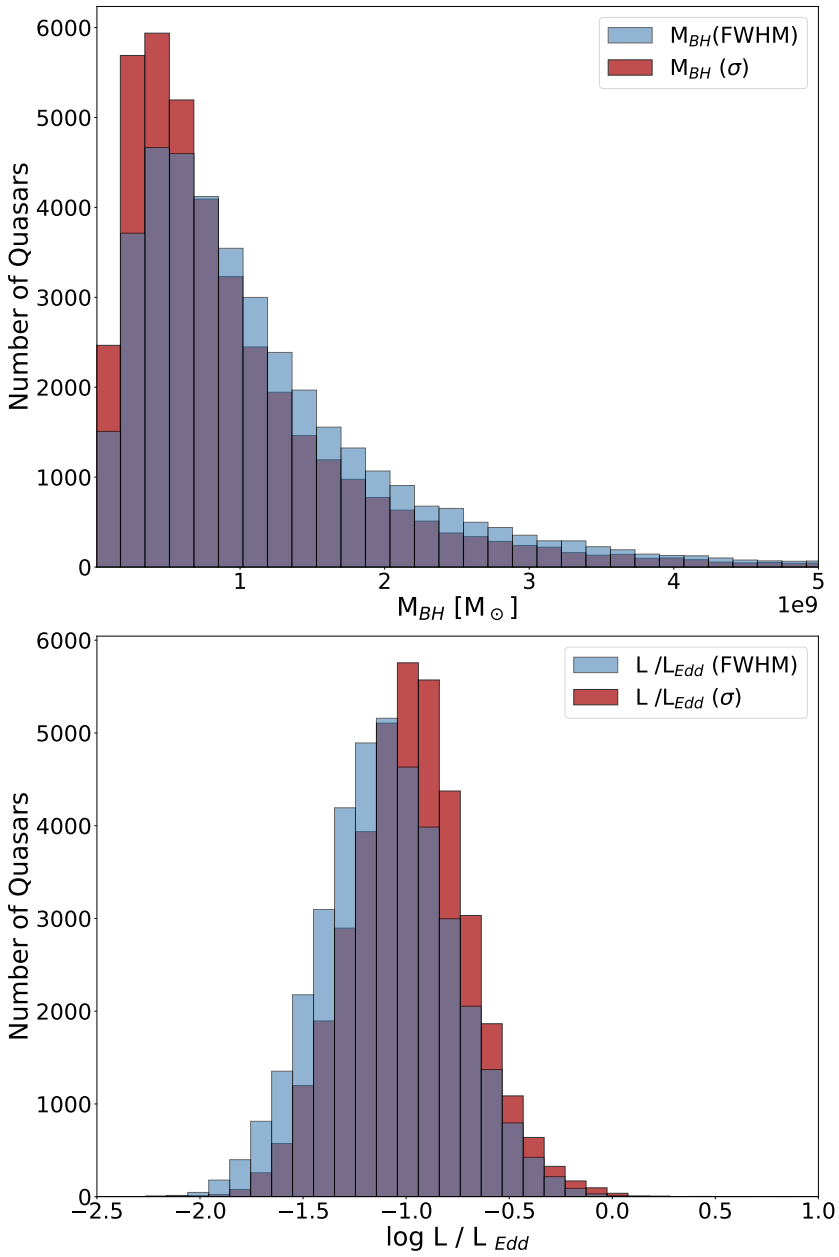

Figure 4.4: Quasar black hole masses and Eddington ratios for our sample. *Top:* Black hole masses computed from Mg II FWHM, or σ, computed from the fitted emission profile. *Bottom:* Eddington ratios computed from our Bolometric luminosity and black hole mass estimates. To ensure good measurements, we omit linked-Guassian profiles with wing component peak SNR < 0.8, or that have wing FWHM <11,000 km s^{-1} and FWHM $\frac{\text{wing}}{\text{core}}$ ratio > 5.5. Based on our repeated experiments, the M_{BH} results are not sensitive to these particular values.

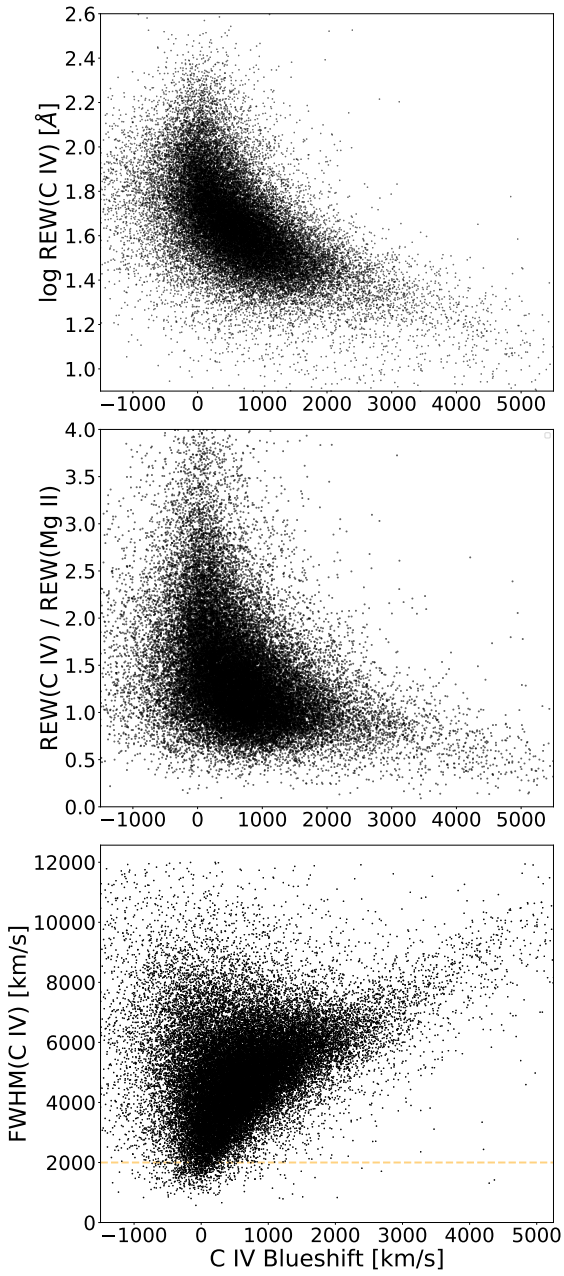

Figure 4.5: Measured quantities from our sample where all distributions exclude FWHM(C IV) <2000 km s^{-1}, unless otherwise stated. *Top:* REW(C IV) vs C IV velocity shift, exhibiting the characteristic distribution that has emerged in the literature as quasar redshift measurements have been constrained. *Middle:* The ratio of REW(C IV) to REW(Mg II) vs C IV velocity shift, showing that for higher blueshifts the REW(C IV) /REW(Mg II) $\leq\sim$1. *Bottom:* FWHM(C IV) vs C IV velocity shift of all quasars in our full sample, with a yellow dashed line indicating quasar cutoff for broad C IV line quasars for our sample. Most quasars appear to follow a trend for broader C IV emission profiles with higher C IV blueshift.

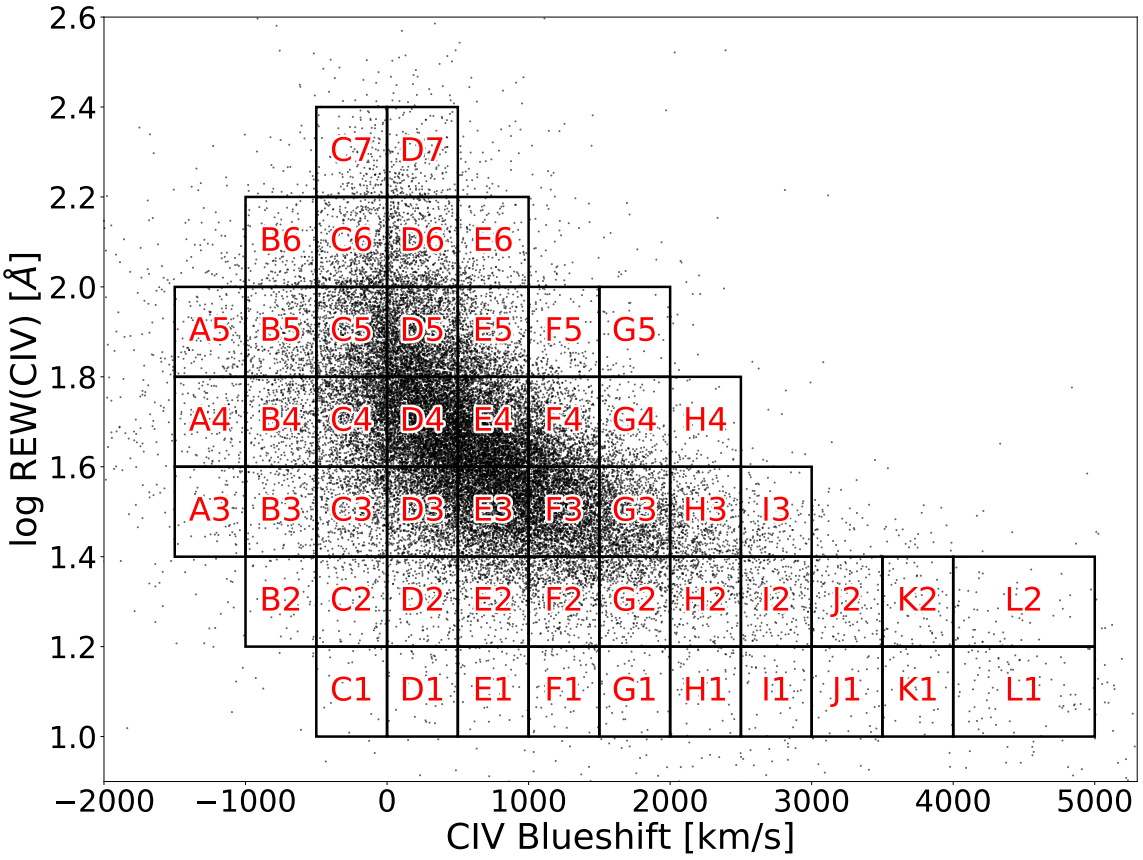

Figure 4.6: C IV REW vs velocity shift, identical to the top panel of Figure 4.5, but with partitions labelled for further analysis (see Sections 4.5.2, 4.5.3, and 4.5.4. We choose box sizes which can resolve overall trends, but not so few spectra to have poor statistics for each box. Cells are 0.2dex in height and and 500 km s^{-1} in width, except for column L, which needed to be 1000 km s^{-1} in width to include a sufficient number of quasars. Every partitioned cell contains at minimum ~100 objects.

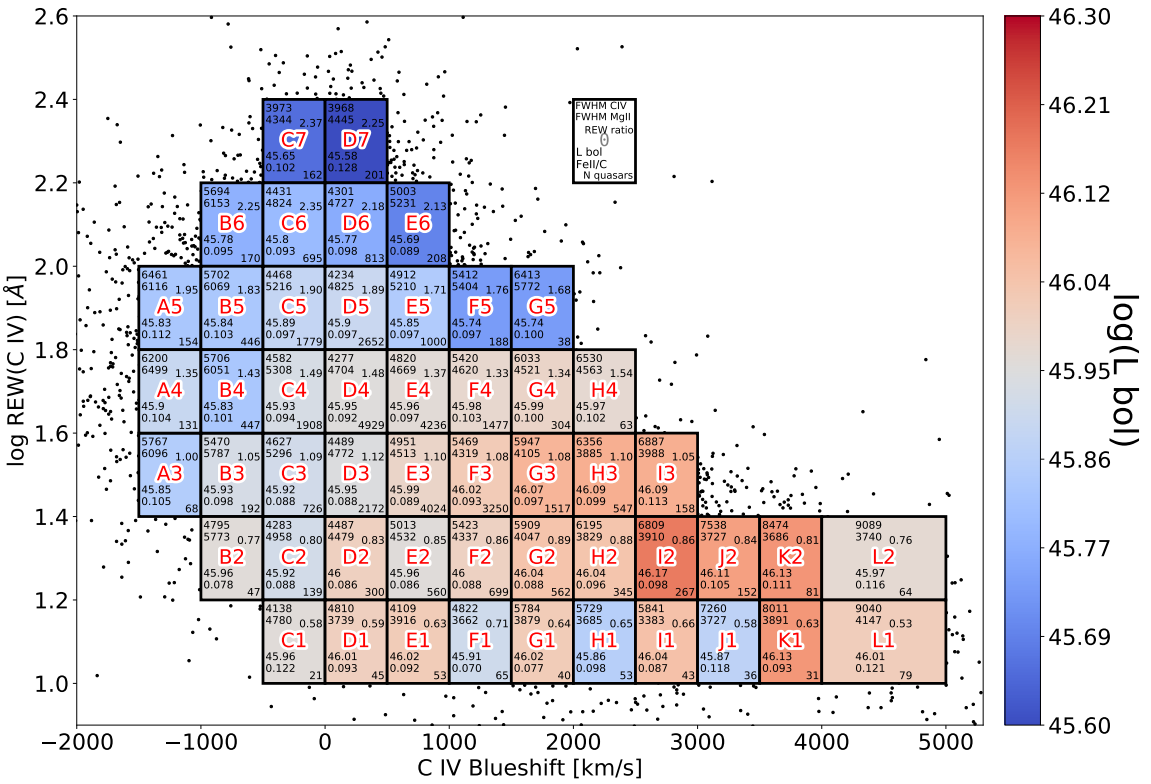

Figure 4.7: C IV REW vs velocity shift of our sample with regions color coded for median $L_{\rm bol}$. Within each boxed region we present median values from the quasar spectra. The white box at the top right gives a legend to where the values are located. These values include, FWHM of C IV and Mg II REW ratio of C IV to Mg II $L_{\rm bol}$, the relative strength of Fe II to continuum, and the number of quasars in the boxed region. The color of the region indicates the median i–$W3$ color within the box.

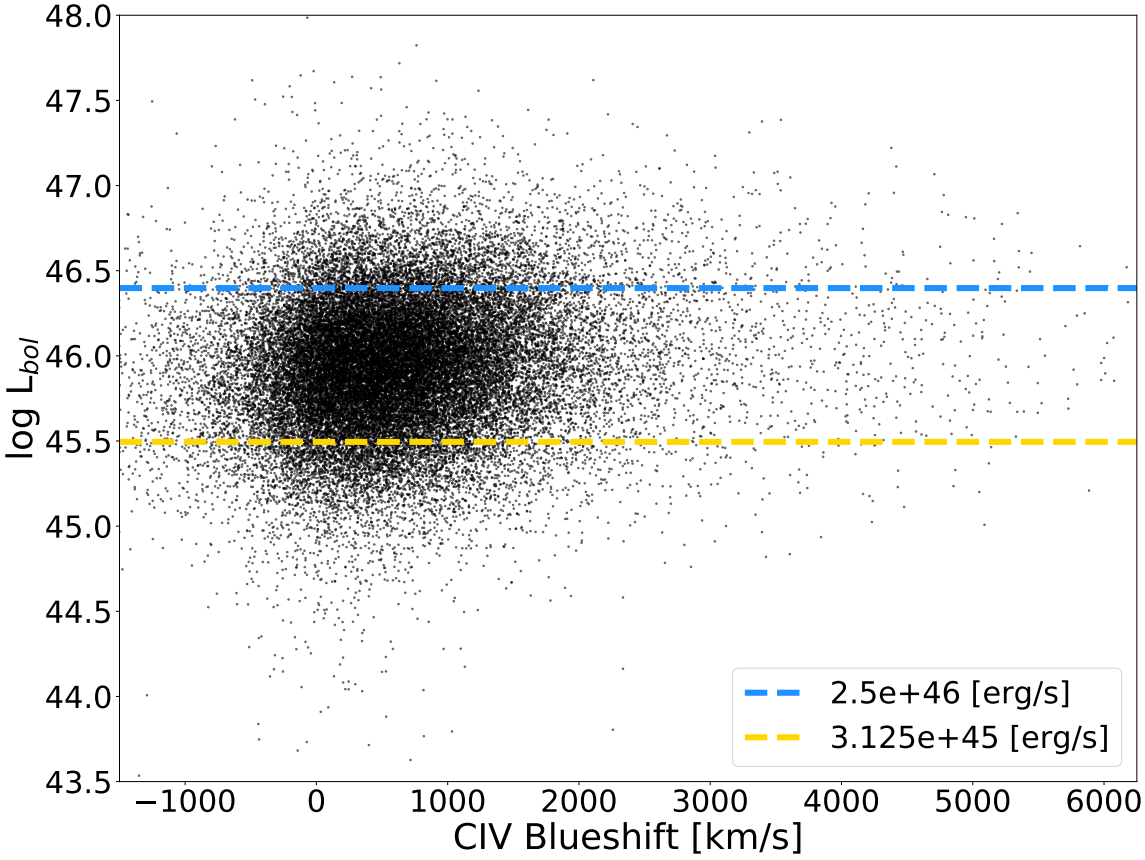

Figure 4.8: Bolometric luminosity vs blueshift, with boundaries defined in luminosity to isolate trends in blueshift without biasing composite spectra to have both high blueshift and high luminosity.

4.5.2 Composite Spectra

Here we generate composite spectra to see overall trends in quasar properties with varying C IV line strength and blueshift. We use medians of selected rows and columns across our partitioned boxes in Figure 4.6, to show variation of spectral features across a wide range of C IV REW and blueshifts. Implications of found correlations will be discussed in Section 4.6.

We isolate trends with respect to C IV blueshift from luminosity by constraining $L_{\rm bol}$, by setting an upper and lower bound for inclusion, when generating medians. Figure 4.8 shows the distribution of computed $L_{\rm bol}$ across C IV blueshifts for our sample. We construct these median composite spectra from quasars within the luminosity range $3{\times}10^{45}$ erg s^{-1} $< L_{\rm bol} <$ $2.5{\times}10^{46}$ erg s^{-1}. Imposing this constraint ensures that median luminosities of our composite quasars remain nearly constant across the full range of C IV blueshifts, and still retains a large sample of ~30,000 quasars (see Table 4.1).

Table 4.2 presents quasar parameter medians from the Composite Sample in Table 4.1, grouped by C IV velocity from -1500 to 6000 km s^{-1}, and in bins of 500 km s^{-1}. We chose this bin size to include a significant, minimum number of quasars at large blueshift bins (~100 quasars), without obscuring trends by broadening the composite emission profile. We made luminosity cuts to isolate trends that are independent of $L_{\rm bol}$ and the Baldwin Effect (see Table 4.1 and Figure 4.8). Our median λL_λ luminosities are are roughly constant across the wide range in velocity (within about 12 per cent of the overall median), confirming our luminosity criteria is effective, and shows that any other trends seen are not explained by significant variations in luminosity.

Figure 4.9 shows median spectra from the Composite Sample in Table 4.1, from -1500 to 6000 km s^{-1}, and associated with the medians in Table 4.2. Most notable, is C IV FWHM and

REW correlation with blueshift. The line strength of C IV weakens, indicated by the median REW decreasing from ~50 to 10 Å, as blueshift increases. Conversely, the line broadens with increasing blueshift. From median C IV velocity ~260 to 5260 km s^{-1}, the FWHM more than doubles from ~4300 to 9400 km s^{-1}. Mg II profile width as measured by FWHM, or σ, does not display dramatic broadening or narrowing with large changes in C IV blueshift.

Although we describe the blueshifts in terms of a parameter similar to the line centroid (Section 5.8 in Hamann et al. 2017), the blue wings in the highest blueshift cases extend beyond 11,000 km s^{-1}. In addition, the changing appearance of the C IV line profiles as we look from low to high blueshifts suggests there is a decrease in the emission from material at low velocities, rather an increase in emission from high-velocity gas.

Overall the spectra show changes in many line strengths, including He II, with increasing C IV blueshift. Near to C IV, we can see He II also gradually weakening until there is no line emission when C IV is at the its most extreme blueshift. It is important to note that while He II and C IV are getting weaker at large blueshifts, other lines from lower-ion species (C II], Mg II, etc.) stay the same or get slightly stronger. Some lines become weaker relative to others, such as weaker C III] λ1909 relative to Al III and Si III]. Some low ionization lines appear stronger, such as C II] and Fe complexes, with increasing C IV blueshift. REW for Mg II only varies slightly in comparison to C IV line strength across blueshift velocities, which is also visible in other low-ionization line strengths.

Low-ionization lines, such as O I and C II, do not shift in velocity relative to Mg II, and appear to agree with the Mg II emission centroid for systemic redshift. Any velocity shifts in these lines relative to a true quasar systemic would not be evident in our data.

Finally, C IV's asymmetric broadening and weakening is also present in high-ionization lines, such as Si IV and N V, but less apparent. However, the magnitude of all of these changes is less than what appears in C IV, consistent with less participation in a BLR outflow by lower-ionization lines.

Figure 4.10's top two panels show the median composite spectra from a single column from Figure 4.7, at C IV blueshifts 0 to 500 km $s^{-1}$and REW 16 to 251 Å. Both emission profiles of C IV and Mg II remain symmetric and gradually weaken along with C IV. All other lines in the spectrum likewise decrease in strength. Low-ionization lines, and Fe complex, also decrease in strength with C IV REW, which is not the case when C IV is weak and strongly blueshifted.

Figure 4.10's bottom two panels display the same spectral range, but using composites from specific partitioned boxes in Figure 4.6, following diagonally along the bulk of the distribution. This composite shows the same trends seen in Figure 4.9 more cleanly. Again, we see the low ionization lines remaining strong (e.g., Mg II, C II, and Fe complex), while other lines weaken with C IV. Some high ionization lines, like Si IV and N V, blueshift in a similar asymmetric pattern as C IV's profile.

4.5.3 Eddington Ratio Dependencies

Eddington ratio shows a nearly uniform correlation with increasing C IV blueshift. Table 4.2 shows Eddington ratio in the Composite Sample increases from 0.08 to 0.14, with larger C IV blueshift.

Figure 4.11 shows the distribution of Eddington ratios against blueshift for our BH Mass sample in Table 4.1, with black hole mass computed using both FWHM and dispersion methods described in Section 4.4.3. Using either Mg II FWHM or $\sigma_{\mathrm{Mg\,II}}$ to compute L_{Edd} yields a similar

distribution. We note that the $\sigma_{\mathrm{Mg\,II}}$ has less scatter than the FWHM method. However, most Mg II profiles were fit using a single Gaussian, which conversion from FWHM to σ is a constant, and so we choose to use FWHM for our distribution comparisons. Figure 4.11 illustrates that the method used to measure black hole mass does not have significant effect on Eddington ratio trends.

Figure 4.12's top panel shows log Eddington ratio color-coded across the distribution of C IV REW versus blueshift. The trend in Eddington Ratio is stronger, and more coherent, than with Bolometric luminosity seen in Figure 4.7. It is evident that the trend in Eddington ratio is not a simple correlation with C IV blueshift, and that REW is an important third parameter, because the trend does not strictly follow left to right across the REW and blueshift distribution.

4.5.4 Color Dependencies & Reddening Corrections

We show distributions of the Color Sample in Table 4.1, requiring quasar colors using r and z filters from the SDSS (York et al. 2000; Alam et al. 2015), and/or $W1$ band from WISE (Wright et al. 2010b, Yan et al. 2013), as provided in the BOSS DR12Q quasar catalogue (see Pâris et al. 2014 and Pâris et al. 2017b). r, z, and $W1$ filters fall approximately in the rest wavelengths 1960 Å, 2880 Å, and 1 μm at our Full Sample median redshift. These colors were chosen to avoid contamination by the wings of the C IV profile (specifically in r), especially if it is blueshifted, but still a wide enough sampling of emission determine a slope of the UV continuum.

Figure 4.12's bottom two panels show the Color Sample with C IV REW versus blueshift, except color coded to r–$W1$ and r–z. These quasar color panels show the same trend as Eddington ratio, although $W1$ limits the sample more due to lower sensitivity. These panels show that the color trend is not simply 2-dimentional with color vs blueshift, seen in Figure 4.13. Figure 4.13 presents the distribution of r–z and r–$W1$ colors compared to blueshift. r–z shows a distribution similar to

figures including C IV REW, with $r-z$ decreasing with increasing blueshift. This trend is less strong in the $r-W1$ distribution.

Quasars with smaller $L_{\rm bol}$ and Eddington ratios are also redder. A reddening correction could therefore weaken trends we find with $L_{\rm bol}$ and Eddington ratio. However, it's not clear that a correction is appropriate given that there might be real difference in the SED unrelated to dust reddening. If we assume these quasars have the same intrinsic SED, reddening corrections indicated by the color differences would be quite small. We confirm this within the range of $r-z$ values from 4.12, and the median redshift. Using a typical dust reddening formula (similar to those used in Richards et al. 2003), we get E(B-V) = 0.105 and extinction A_{3000} = 0.57 magnitudes, or a factor of 1.69 flux suppression.

4.5.5 Individual Spectra

Here we present spectra of individual quasars to demonstrate the reality of the highest blueshift cases and illustrate some of the range in the emission line properties not evident from the median spectra. Figures 4.14 - 4.21 are sets of individual spectra of typical quasars for illustration, or spectra with extreme properties for further discussion, chosen from regions in the top and bottom panels of Figure 4.5.

Figure 4.14 presents three individual spectra with a wide range of C IV emission strength REW >100Å, and blueshifts >2000 km s^{-1}. Quasars with these two parameters are rare in our sample (see Figure 4.5), only nine with emission-line measurements, and we present the spectra with the best signal to noise across the continuum.

Figure 4.15 presents four with <10Å, and blueshifts >2000 km s^{-1}. Most quasars with extremely weak C IV lines have a more uniform distribution of blueshifts, from ~2000 - 6000 km s^{-1}.

Figure 4.16 presents four individual spectra with extremely broad C IV (FWHM >10,000 km s^{-1}), and blueshifts >2000 km s^{-1}. These quasars consistently show the same emission profiles seen in the highest blueshifts in the composite median spectra.

Figure 4.17 presents individual spectra with blueshifts >6000 km s^{-1}, of which there are ten. J01410.94+043210.7 has strong line measurements despite the lack of Si II/Si IV coverage, and coincidentally is one of the top ten highest in C IV blueshift. It also has an absorption spike red-ward of civ, which could indicate C IV is more blueshifted, and Mg II may have a blue wing.

Figure 4.18 presents nine individual spectra with blueshifts >4000 km s^{-1} and high signal to noise. J114925.62+665949.5 is a good SNR spectra with secure C IV blueshifts, and is somewhat "typical" from these highest blueshifts. The same goes for, J115513.09+133454.9, J160513.17+325829.9, J164250.45+263122.7, and J231709.88+223145.1 although with larger C IV REW. J003355.94+012720.8, J142601.30+243245.7, and J220823.33+025839.0 are spectra with very weak, broad and uncertain C IV but the measurements are supported by blueshifted Si IV and the Mg II redshift is confirmed as at least a lower limit. J142601.30+243245.7 has a blue wing in Mg II, and C IV absorption spike. J231709.88+223145.1 is odd because the Si II, O I and maybe other low-ion lines do not support the Mg II redshift. These are uncertain but the blueshifts still appear real (just maybe not as large as indicated). Crosschecking with Fe II and C II] seems to support the Mg II redshift.

Figure 4.19 presents eight interesting spectra of blueshifts 4000 - 5000 km s^{-1}. J082936.30 +080140.6 and J231709.88+223145.1 below both well-measured narrow C IV. J103617.58+414237.1

has narrow C IV. J110018.52+314122.5 has a C IV mini-BAL at around 1355Å (corresponding to a gas velocity of ~0.13c). J111800.50+195853.4 is an example of blue asymmetry in Mg II. J135506.26+292550.3 has a C IV mini-BAL near 1270Å (corresponding to a gas velocity of almost 0.18c), confirmed by SDSS in 2006(DR7) and 2013(DR16). J150839.30+320414.2 has very broad C IV as well as blueshifted. J152731.29+511206.4 has Damped Lyman Alpha at ~1000 km s^{-1} suggesting Mg II redshift is lower limit. This hints that the low-ion BLR is also outflowing at least sometimes, and not reliable indicators of the systemic frame. J231709.88+223145.1 has relatively narrow C IV, Fe III ~1950Å may confirm redshift in spite of Si II.

Figure 4.20 presents four spectra of blueshifts 5000 - 6000 km s^{-1}. J094748.06+193920.0, J101822.95+203558.6, and J124202.12+615658.8 below have redshifted C IV absorption, possible Mg II is a lower limit.

Figure 4.21 presents three spectra with the highest blueshifts of the sample, from Fig. 4.17, and with less smoothing applied to the spectra to minimize blending of emission features. J154443.44+080052.1 is not included for having high noise spikes on top of the Mg II emission-line. J012505.27+063829.5 has the largest blueshift of the sample. J084842.64+540808.2 and J140701.59+190417.9 are 2nd largest blueshifts, confirmed by multiple weak low-ion lines, and have very broad and flat C IV profiles.

Analysis of these individual quasars confirms the reality of trends in the extremes of Fig. 4.5, and highlight unique features that could otherwise be lost by median composite spectra.

4.6 Discussion

Blueshifts observed in the broad emission lines of quasar C IV serve as valuable indicators of outflows in moderately to highly ionized gas from the regions emitting these broad lines (see Section 4.2). We present blueshift measurements of C IV in a total of 39,249 quasars with redshifts ranging from 1.52 to 2.42, as observed in the SDSS. Our main objective is to gain insights into the nature and origins of these outflows. This is achieved by studying the characteristics of the C IV blueshifts and establishing connections between the blueshifts/outflows and other spectral properties of the quasars. Constraining outflow speeds necessitates reliable systemic redshifts. Notably, our approach differs from prior studies as we determine the quasar's systemic redshifts exclusively through fitting the low-ionization Mg II emission line, which is considered close to systemic redshift of the quasar (e.g. Shen et al. 2008; Shen et al. 2016b; Li et al. 2017). This method allows us to explore a unprecedented range of outflow velocities compared to previous work, reaching blueshifts > 6000 km s^{-1}, and maintain a sample size that is statistically significant. In this section we will discuss our results for the full sample, and interesting subsamples.

Broad emission lines offer an important advantage over absorption lines when studying outflows, because they aren't confined to gas along the direct line of sight to the quasar's emission sources. However, this flexibility also means that the gas can be moving at various angles relative to our line of sight, which complicates the relationship between observed blueshifts and outflow velocities, as it becomes contingent on the specific modeling used. The blueshifts we measure by analyzing the emission-line centroids only give us a lower threshold for the actual flow velocities. In situations where there are exclusively radial motions, and negligible additional sources of line broadening, the most accurate estimate of outflow velocities comes from the most pronounced

blueshifts in the blue portion of the observed line profiles (e.g., the v_{98} parameter as employed by Perrotta et al. 2019). By utilizing the parameters provided in our study, we can approximate the actual C IV outflow velocities based on the blueshifts of the line centers, plus half of the measured full width at half maximum (FWHM), while also accounting for half of the doublet separation in C IV (equivalent to 250 km s^{-1}). For example, in the high-blueshift quasar J100351+001502 shown in Figure 4.17, we could infer that the C IV outflow speed is roughly 6009 + 5296 - 250 ~ 11,000 km s^{-1}.

Our composite median spectra reveal consistent trends of weakening He II with increasing C IV blueshift (see Figures 4.9 and 4.10). We see that high blueshifts correspond to both weaker C IV strength, broader emission profile, and higher Eddington ratios (see top panel of Figure 4.12). We are the first to show that these trends extend to the most extreme blueshift velocities, which indicate radiative line-driving may be one of the mechanisms generating extreme outflows (Leighly & Moore 2004; Richards et al. 2011; Rankine et al. 2020; Temple et al. 2023).

Observational evidence strongly supports both of these factors as correlating with faster outflows. For instance, the inverse correlation between the He II λ1640 emission-line REW and larger C IV emission-line blueshifts (Leighly & Moore 2004; Richards et al. 2011; Rankine et al. 2020; Temple et al. 2023) as well as faster C IV broad absorption-line (BAL) outflows (Baskin et al. 2013; Hamann et al. 2018; Rankine et al. 2020) indicates the importance of softer UV spectra in driving outflows. This inverse relation is also observed in hyper-luminous quasars (Vietri, G. et al. 2018). Furthermore, larger C IV blueshifts have been found to correlate with higher Eddington ratios (Baskin & Laor 2005; Coatman et al. 2016; Rankine et al. 2020; Temple et al. 2023). Higher Eddington ratios can provide a stronger radiative driving force relative to gravity. Weak He II

indicates a weaker far-UV flux, thus a softer UV continuum, and helps maintain moderate ionization levels and substantial opacities in the outflow to enable radiative driving in the near-UV (Leighly 2004).

As C IV REW decreases with blueshift, we see low-ionization lines becoming stronger, and a trend of weaker C III] relative to Al III and Si III]. There have been possible models proposed to explain this trend, but higher densities and/or lower degrees of ionization would decrease C III] relative to Si III] and Al III (Leighly & Moore 2004; Leighly 2004; Richards et al. 2011).

4.6.1 Eddington Ratio Distributions

Figure 4.12 displays several trends which reveal complexities to our goal of finding what drives powerful outflows. We find larger Eddington ratios also correlates with increasing blueshift (bottom panel of Figure 4.12, and also indicated in Baskin & Laor 2005; Coatman et al. 2016; Rankine et al. 2020; Temple et al. 2023). When the luminosity of the quasar is near to $L_{\rm Edd}$, and the gravitational force from the SMBH is nearly balanced, it becomes easier to drive an outflow. Eddington ratio may therefore be an important factor in allowing an ensemble of conditions (e.g., high luminosity, continuum shape) to take maximum affect.

We confirmed any reddening that could change the Eddington ratios in Figure 4.12 may be influenced by about A_{3000} = 0.57 magnitudes extinction, or a factor of 1.69 flux suppression. The effect on Eddington ratios will go as the square-root of that, a factor of 1.30 or 0.11 in log. Comparing that to the bottom panel in Fig. 4.12 shows that performing a reddening correction as above would weaken the trend but not undo it. This is a maximal correction, because the 0.3 color difference is

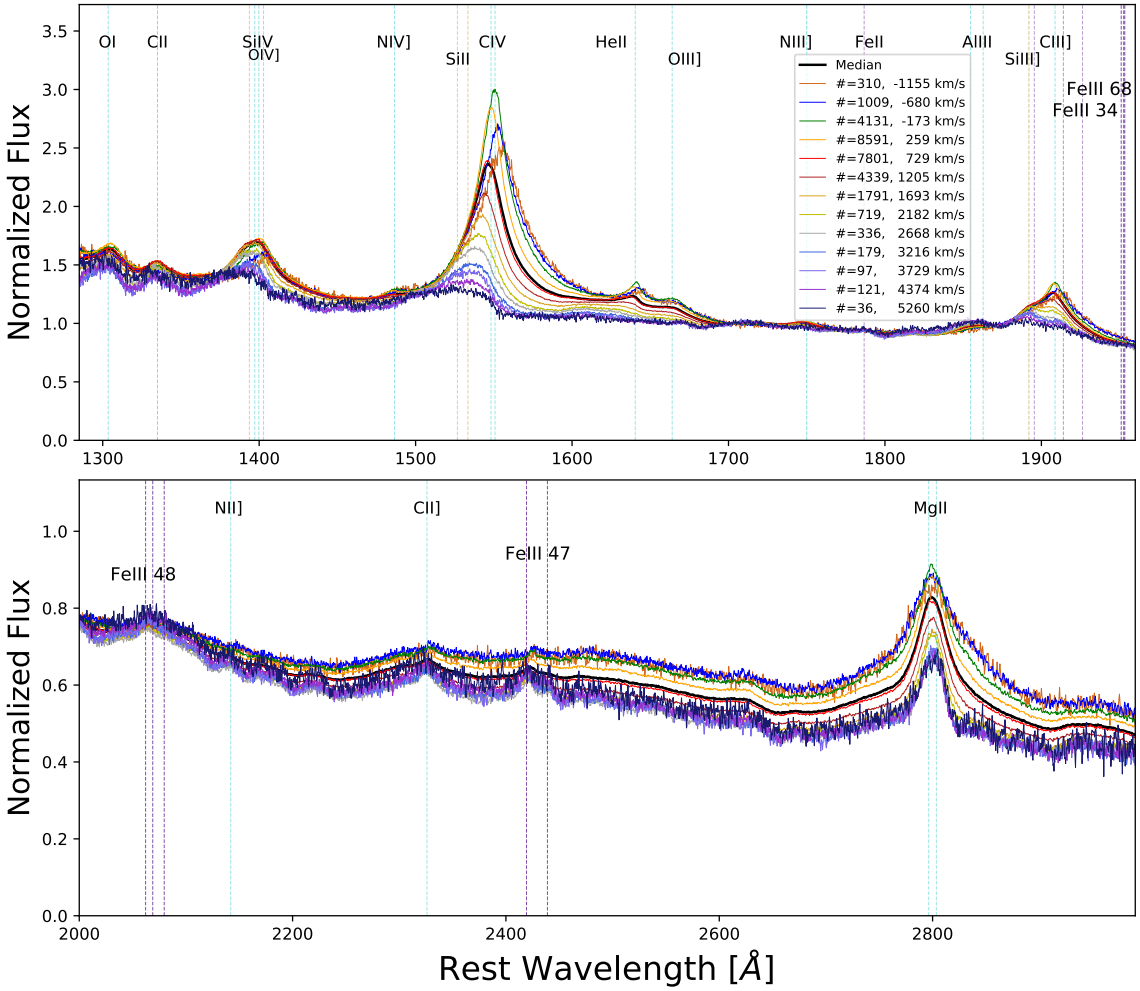

Figure 4.9: Median composite spectra from the Composite Sample. These spectra are generated from vertical columns, from Figure 4.8, defined 500km s^{-1} in width from −1500 to 6000 km s^{-1}. Color coded in the legend are the number of spectra used to generate each composite, and their median C IV blueshift. For more information, see Table 4.2. Spectra are normalized to unity at ∼ 7000Å, before taking the median. Spectra included with C IV velocity over 4000 km s^{-1} are visually confirmed to have similar blueshifted profiles as Si IV and/or confirmed Mg II redshift with Si II. Something straight forward to correlate is stronger low-ion lines and weaker He II and C III]/Al III at larger blueshifts.

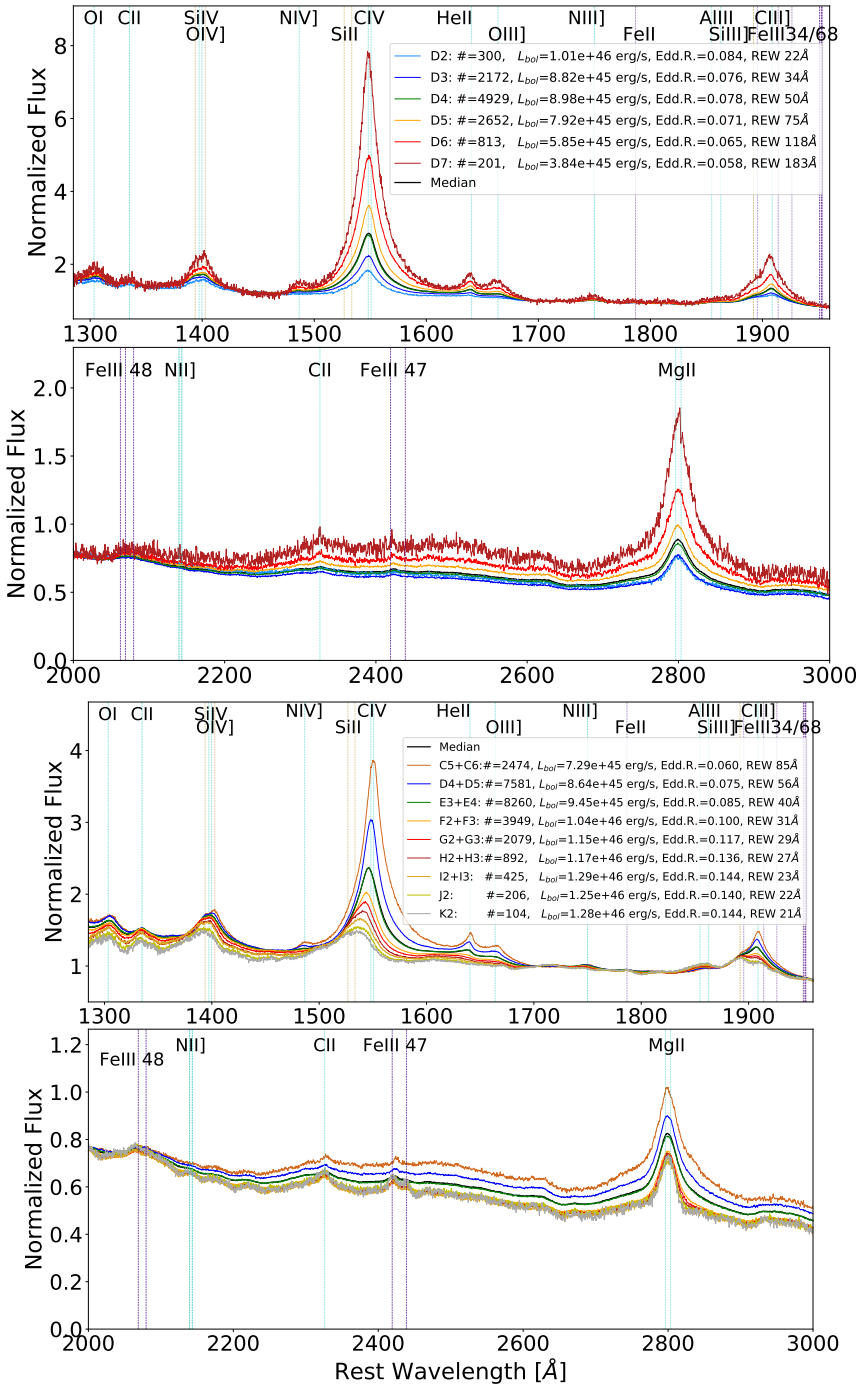

Figure 4.10: Median composite spectra from selected regions of Figure 4.6. The legend presents the number of spectra used for the composite, and median values for luminosity, Eddington Ratio, and C IV REW. *Top:* Ranges of C IV REW between velocities 0 and 500 km s^{-1}. Each bin is defined moving from 16 to 251Å, using $\sim$ 0.2 dex increments. *Bottom:* Diagonal region across the population as REW decreases and C IV blueshift increases.

Velocity Range	Total Spectra	λL_λ [ergs s^{-1}]	Eddington Ratio	REW (C IV) [Å]	C IV Blueshift [km s^{-1}]	Blueshift Standard Deviation [km s^{-1}]	FWHM (C IV) [km s^{-1}]	REW (Mg II) [Å]	FWHM (Mg II) [km s^{-1}]	σ (Mg II) [km s^{-1}]
−1500 - −1000	310	8.20×10^{45}	0.04	60	−1155	132	6479	38	6414	2838
−1000 - −500	1009	7.87×10^{45}	0.04	62	−680	136	5767	38	6112	2735
−500 - 0	4131	8.31×10^{45}	0.06	61	−173	139	4526	37	5254	2448
0 - 500	8591	8.65×10^{45}	0.08	52	259	143	4335	35	4776	2243
500 - 1000	7801	9.05×10^{45}	0.08	41	729	142	4927	33	4659	2155
1000 - 1500	4339	9.48×10^{45}	0.09	34	1205	142	5473	31	4425	2072
1500 - 2000	1791	1.00×10^{46}	0.10	30	1693	138	5967	28	4161	1970
2000 - 2500	719	9.63×10^{45}	0.12	27	2182	143	6257	26	3822	1843
2500 - 3000	336	1.04×10^{46}	0.13	23	2668	142	6685	25	3781	1789
3000 - 3500	179	1.00×10^{46}	0.13	20	3216	146	7447	24	3680	1769
3500 - 4000	97	9.34×10^{45}	0.14	18	3729	148	8087	23	3686	1725
4000 - 5000	121	9.86×10^{45}	0.12	14	4374	274	8951	24	3908	1860
5000 - 6000	36	8.86×10^{45}	0.11	10	5260	295	9436	21	4018	1942
−1500 - 6000	29460	8.94×10^{45}	0.08	43	538	804	5048	33	4682	2195

Table 4.2: Median line properties at different velocity bins of the Composite Sample in Table 4.1, with a limited luminosity range. These bins correspond to the spectra in Figure 4.9 & the top panel of Figure 4.10. Medians were taken of the distribution of values in each bin.

generous. More importantly, we assumed all of the color difference is due to dust reddening instead of intrinsic color differences in the quasars that might be related to outflows/blueshifts. A reddening correction, if warranted, does not undo these trends.

4.6.2 Color Distributions

Additional correlations with SED shape can also influence outflow velocities (Richards et al. 2011; Baskin et al. 2013). Color as measured by spectral index, or broadband color, have indicated slight asymmetric blueshifts in C IV correlated with bluer colors (Richards et al. 2003; Leighly & Moore 2004; Gallagher et al. 2005; Richards et al. 2011). We see trends in SED color (see Figures 4.13 and 4.12), showing that bluer color across the UV to Near-IR correlates with blueshift out to extreme velocities. It has been shown that extreme reddening across UV to IR can also correlate with extreme blueshifts/outflows Perrotta et al. (2019). The "less luminous" quasars are redder. In fact, their luminosities are underestimated because of reddening, and the Baldwin Effect is at least partly a reddening trend, and luminosity.

Quasars can have intrinsically red SEDs without involving dust. Quasars defined by a steep optical-continuum, which are intrinsically red without dust reddening, have been seen to have stronger C IV, C III], and He II emission (Richards et al. 2003). Redder colors can also be attributed to more extinction/reddening along inclined viewing angles in (Baskin et al. 2013), but they do not see a color trend for higher BAL speeds, which should correlate with inclination angle. Emission line blueshifts should have weaker dependence on viewing angle because they sample material moving in all directions, not serendipitous absorption along line of sight. Small differences in reddening could be small differences in viewing angle, therefore extremely small changes in $\cos(\theta)$ factor affecting the measured blueshifts. A more detailed analysis would require specific models for the dust and

outflow geometries around quasars, but is beyond the scope of this work. We note that the trends seen in Figures 4.13 and 4.12 could be due mostly, or entirely, to intrinsic color differences in the quasar SEDs.

Overall, an interesting result that is revealed by our color coded "3-dimentional" parameter space of C IV REW vs blueshift is that they show trends better than the 2D scatter plots. This reveals that the blueshifts are a multi-dimensional/multi-parameter problem. Future studies may look for where large blueshifts cluster in a multi-dimensional parameter space to determine the fundamental causes.

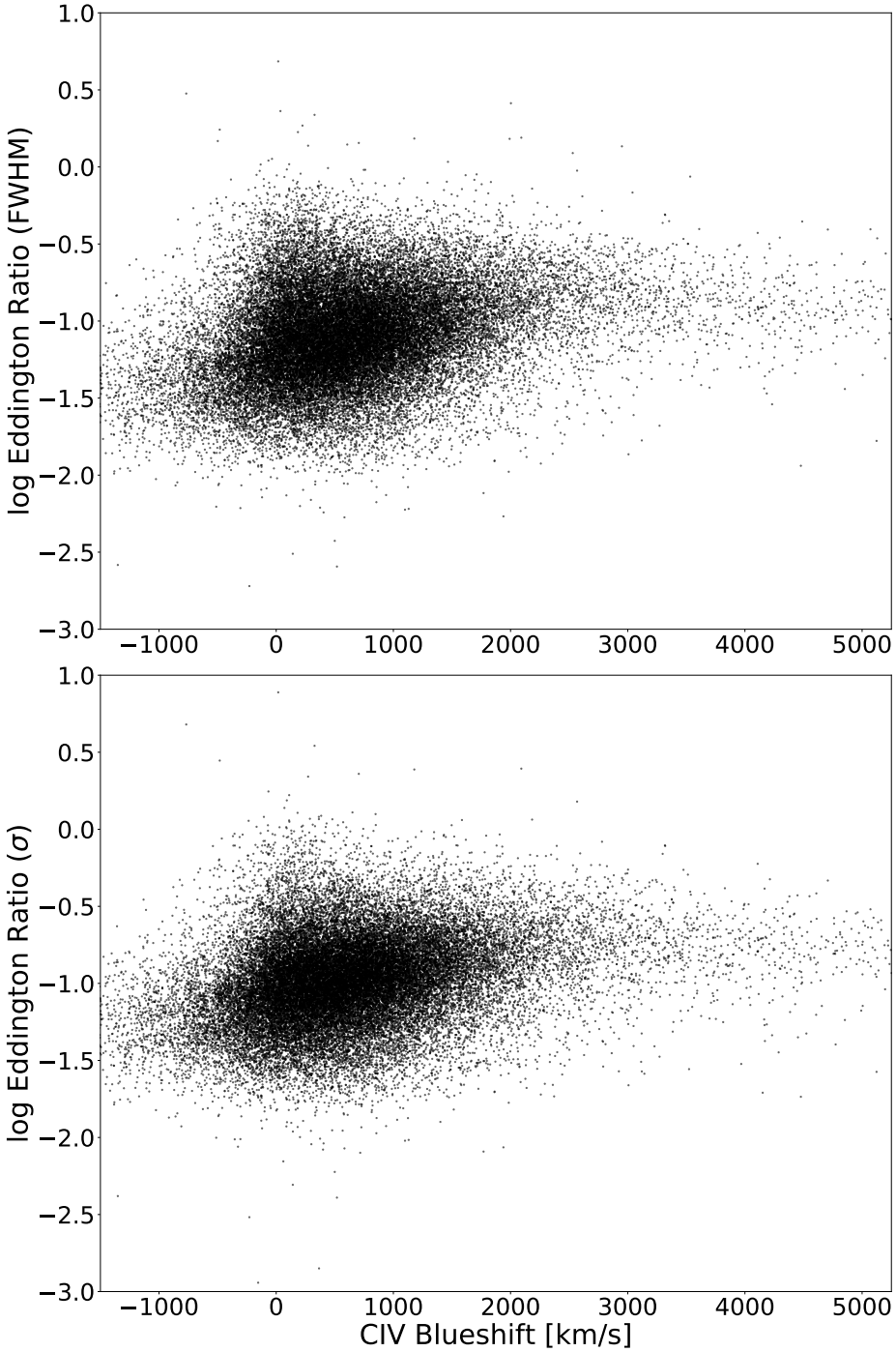

Figure 4.11: Distribution of C IV Blueshift vs Eddington ratio using σ or FWHM of Mg II for computing $L_{\rm Edd}$. *Top:* Eddington ratio computed with FWHM of Mg II. *Bottom:* Eddington ratio computed with σ of Mg II. Eddington luminosity computed using σ shows a narrower distribution than with FWHM.

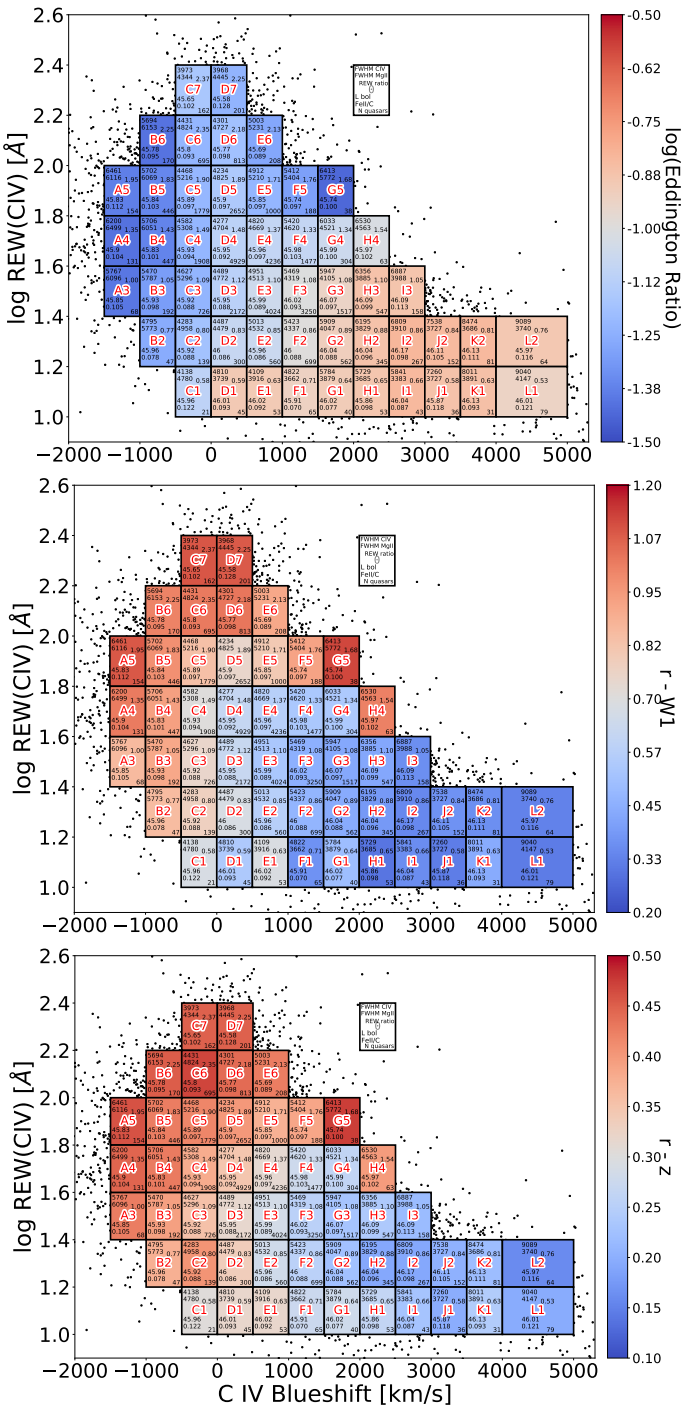

Figure 4.12: C IV REW vs velocity shift with regions color coded for various parameters within the respective region. *Top:* color coded for median Eddington ratio from the BH Mass sample of Table 4.1. *Middle:* color coded with median r–$W1$ from spectra that have $W1$ detection (see Color Sample in Table 4.1). *Bottom:* color coded for r–z, and shows a similar color correlation as r–$W1$.

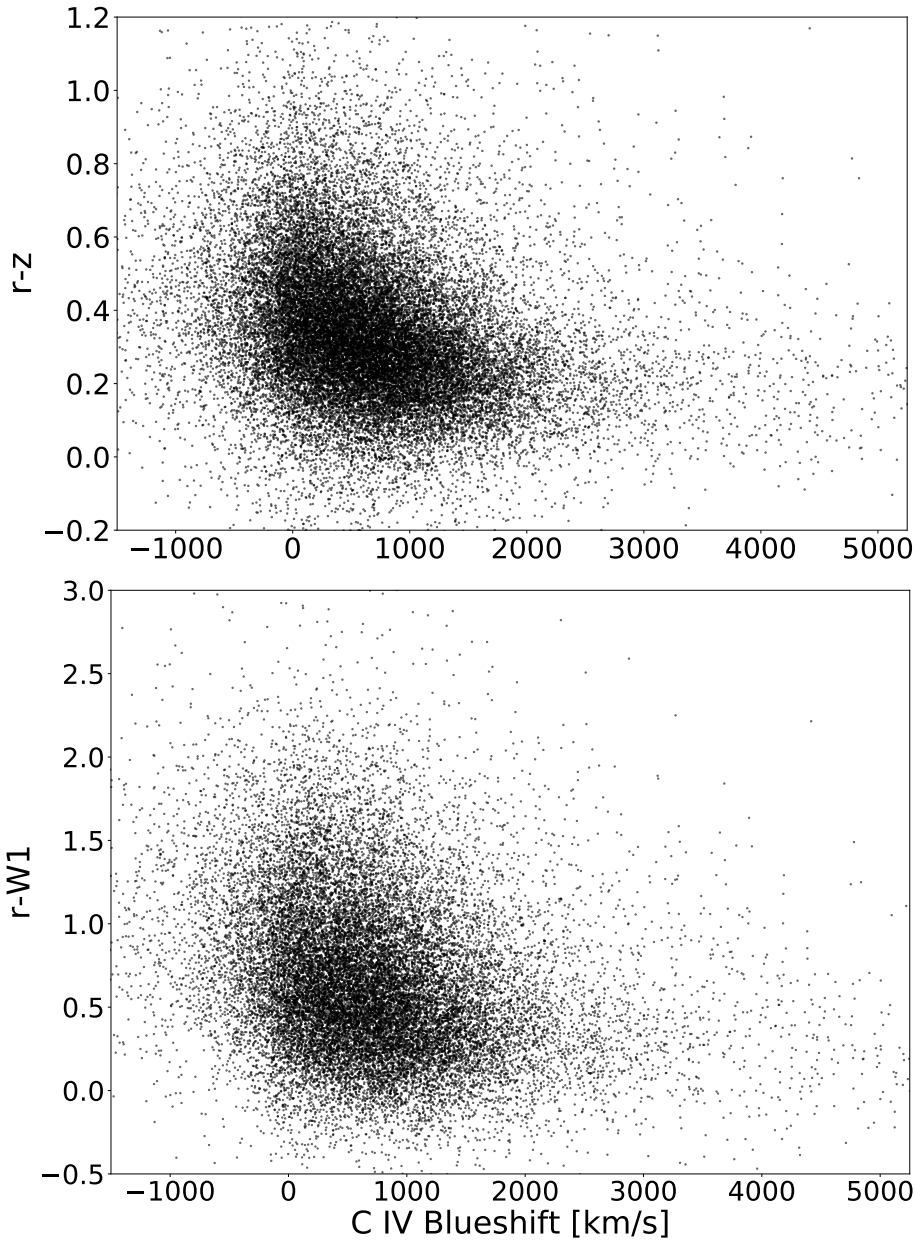

Figure 4.13: C IV velocity shift vs continuum colors for quasars with r,z, and/or $W1$ detections. *Top:* Blueshift vs (r–z) color in our sample with r and z mag data. *Bottom:* Blueshift vs (r–$W1$) color in our $W1$-detected quasars.

4.6.3 Individual Spectra

Broad studies of large quasar populations seldom present rare and interesting cases such as spectra with the most extreme properties. We present individual spectra to convey two points. i) demonstrate the reality of the most extreme cases with blueshifts >6000 km s^{-1}. Our composite figures only consider blueshifts <5000 km s^{-1} because there are too few to construct meaningful medians, and the wide range in blueshifts would blend the C IV profile. ii) display well-measured and interesting spectra at large blueshift. For example, spectra with extreme properties of C IV like large REW, and cases of a strong blue wing in Mg II, that may not be evident from composite spectra.

A surprising feature in many high-blueshift spectra is a peculiar narrow absorption spike at rest wavelengths of C IV. This absorption feature is not typical in quasars with average broad and symmetric C IV profiles, and is smoothed out of median composite spectra. Five of our top 13 fastest-blueshift spectra have this narrow absorption feature (J012505.7+063829.5, J014010.94+043210.7, J105208.27+151004.0, J12402.28+511026.7, and J125935.85+152704.3, and possibly J084842.64+540808.2 and J124502.28+511025.7 as well), The absorption feature is commonly seen in spectra with blueshifts >4000 km s^{-1}, and also high signal to noise spectra when C IV is broad and blueshifted (see Fig. 4.16). The origin of this absorption spike is not immediately clear. One hypothesized explanation is an orientation effect of the accretion disk and BLR, which forms a narrow associated absorption-line system at the systemic redshift of C IV (Richards et al. 2021).

Another unexpected result is blueshifted wings in Mg II profiles. This profile asymmetry is frequently seen in the most blueshifted C IV spectra. J01410.94+043210.7 has strong line measurements that show a blue excess in the Mg II profile, and also contains a C IV absorption spike at a slightly redshifted wavelength, which could also indicate our blueshift velocity is a lower limit. There are similar scenarios in J094748.06+193920.0, J101822.95+203558.6, J125935.85+152704.3 and J142601.30+243245.7. It has been speculated that low-ionization broad-lines could also be involved in outflows under extreme conditions (Hamann et al. 2017; Gillette et al. 2023a). These blueshifted wings may have consequences for Mg II mass estimates of the SMBH, or for other measurements that assume broad-lines are virialized (Shen et al. 2016a; Shen et al. 2016b; Coatman et al. 2016; Shen et al. 2019; Rankine et al. 2020; Temple et al. 2023; Gillette et al. 2023a). Future studies may constrain velocities for these extremely blueshifted outflows, perhaps with non-UV emission lines.

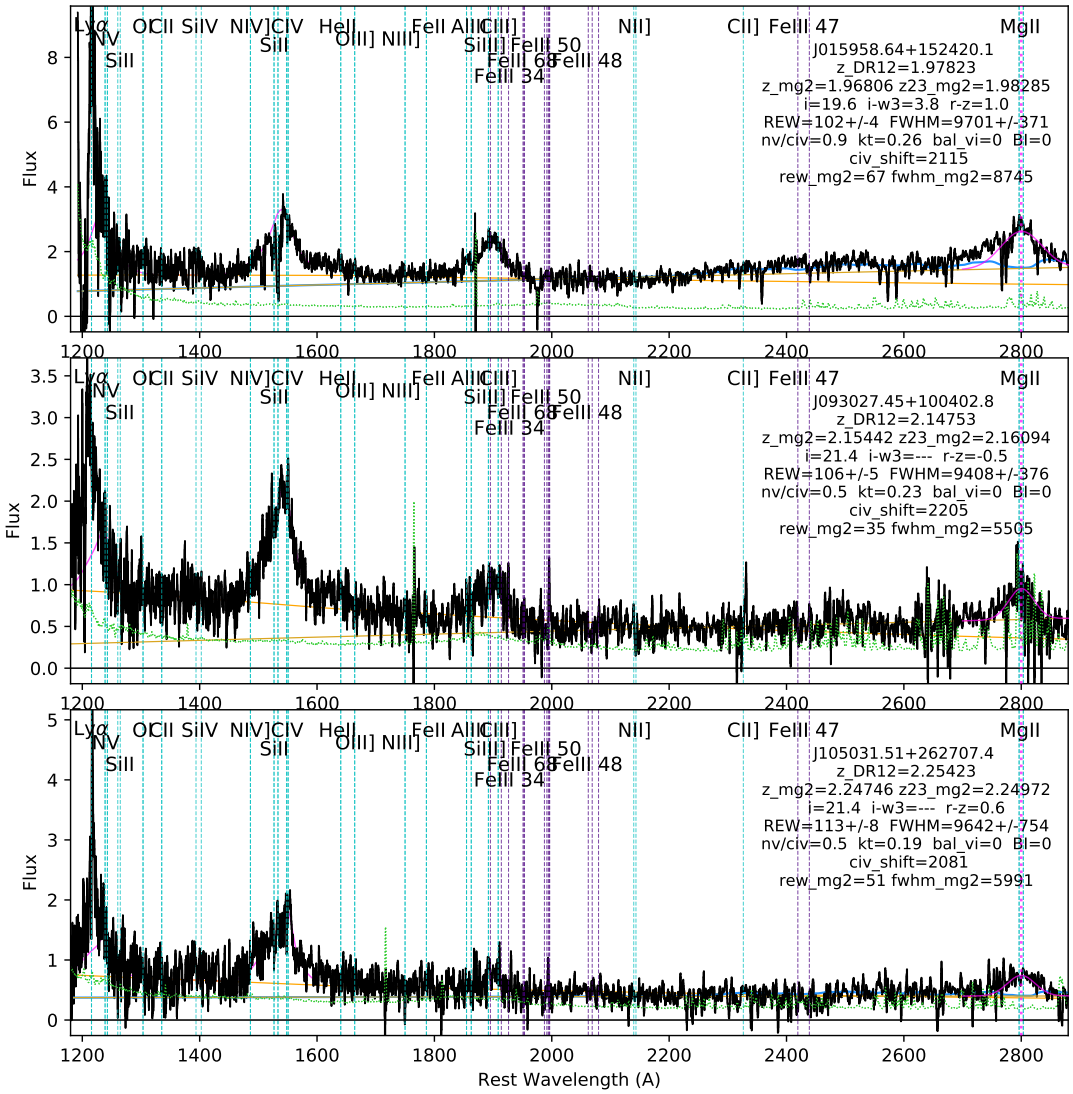

Figure 4.14: Selected spectra with REW(C IV) >100Å, and blueshifted >2000 km s^{-1}.

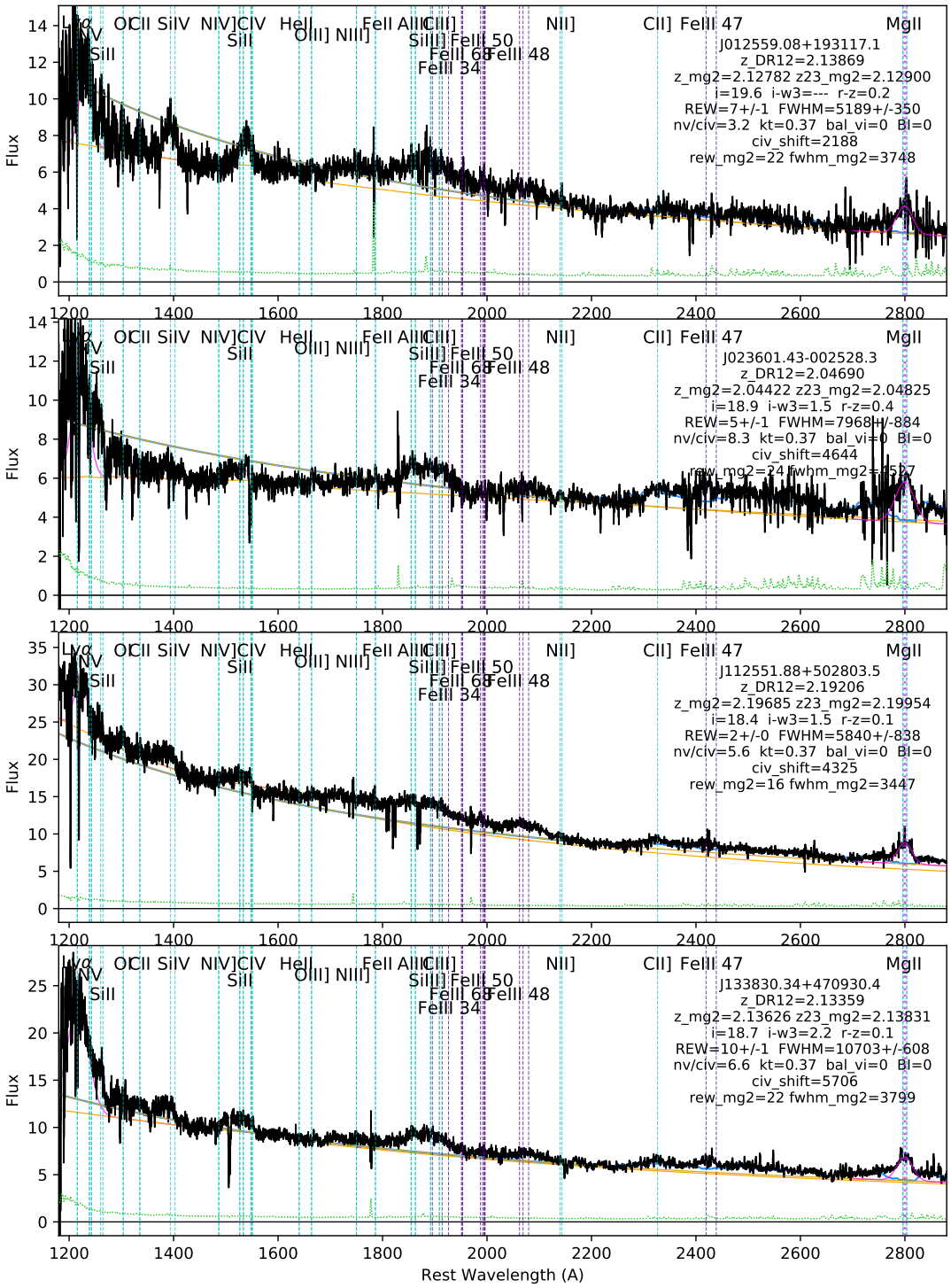

Figure 4.15: Selected spectra with REW(C IV) <10Å, and blueshifted >2000 km s^{-1}.

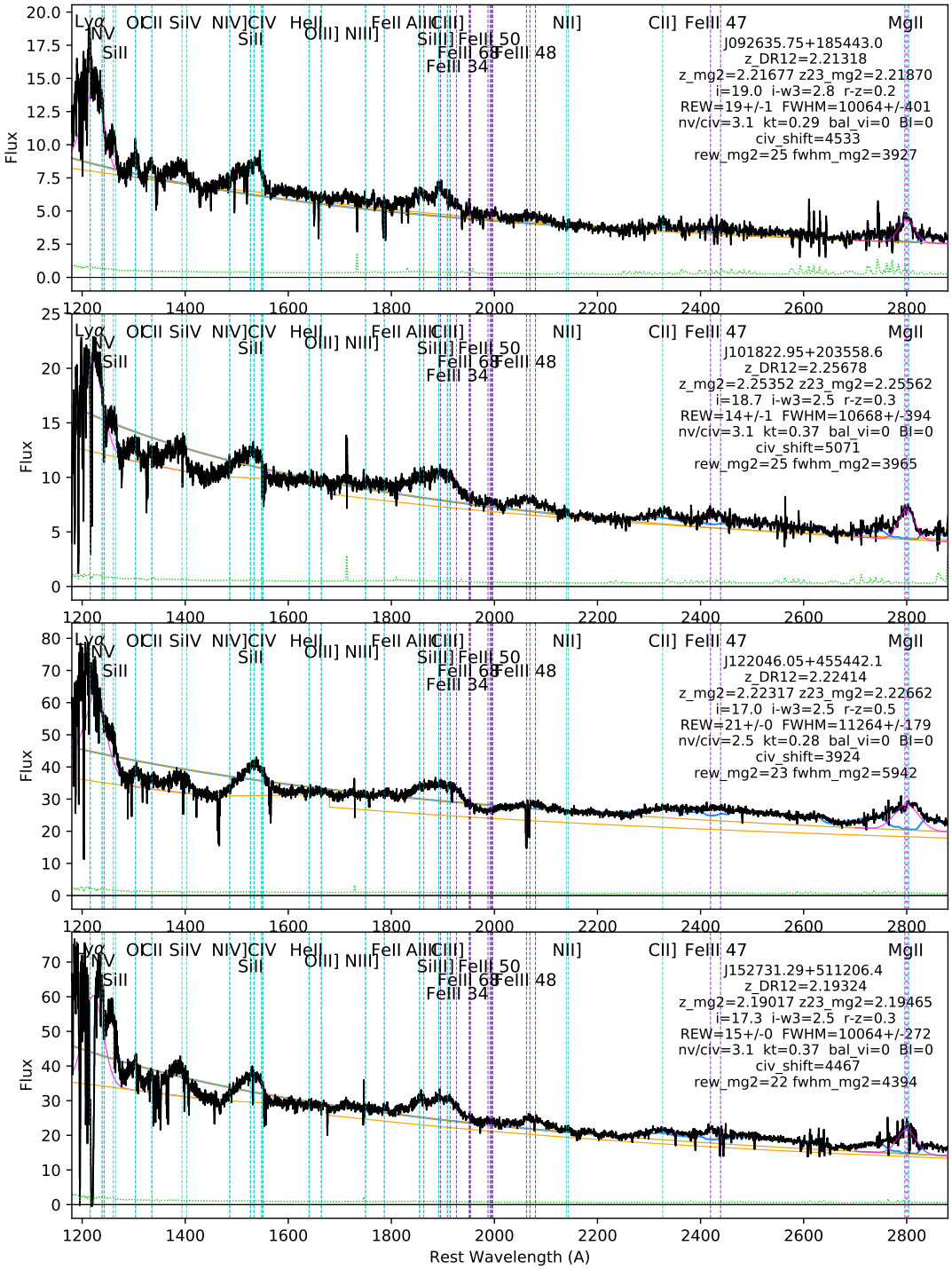

Figure 4.16: Selected spectra with FWHM(C IV) >10,000 km s^{-1}, and blueshifted >2000 km s^{-1}.

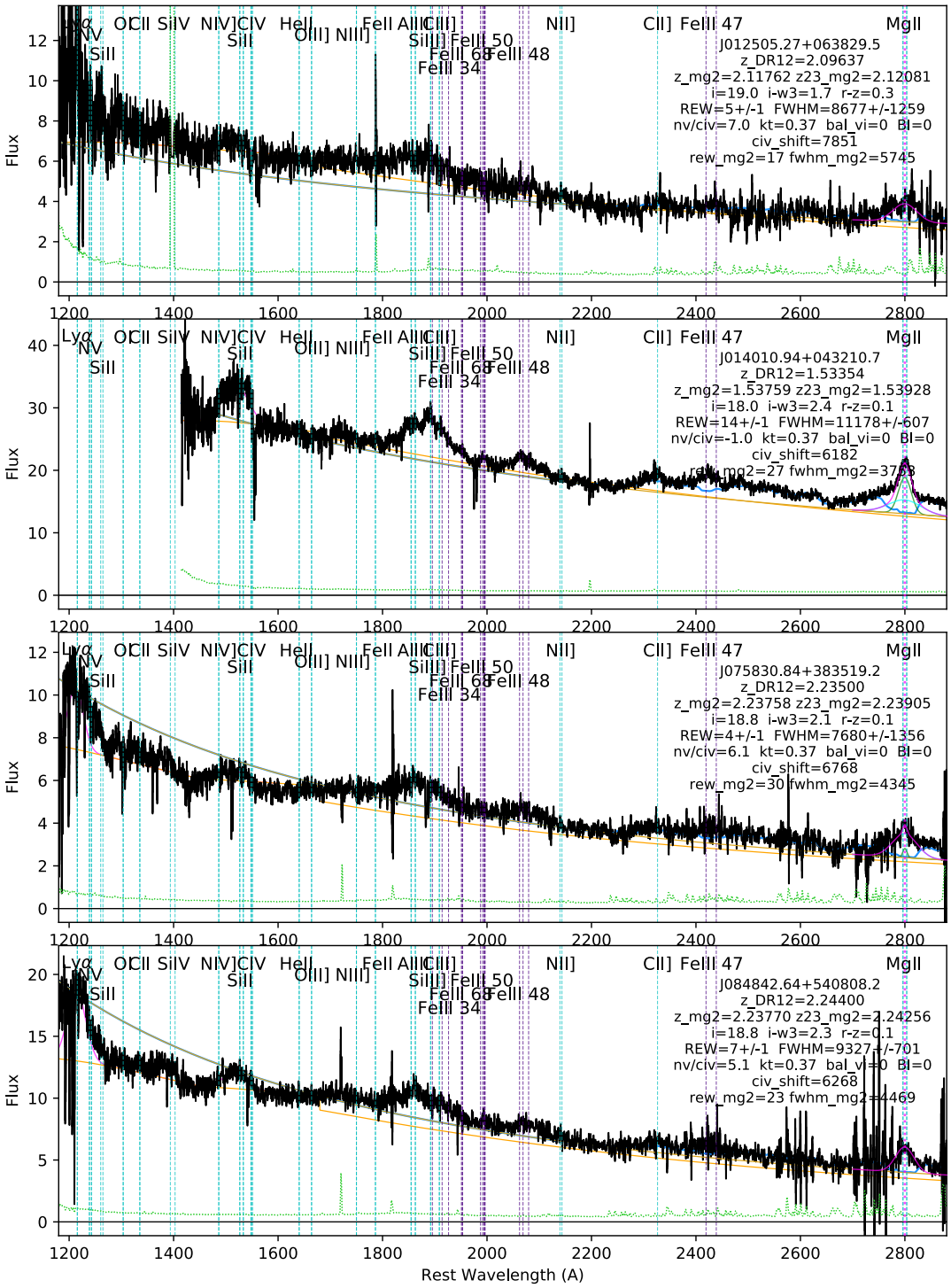

Figure 4.17: Selected spectra with highest C IV Blueshifts > ~6000 km s^{-1}.

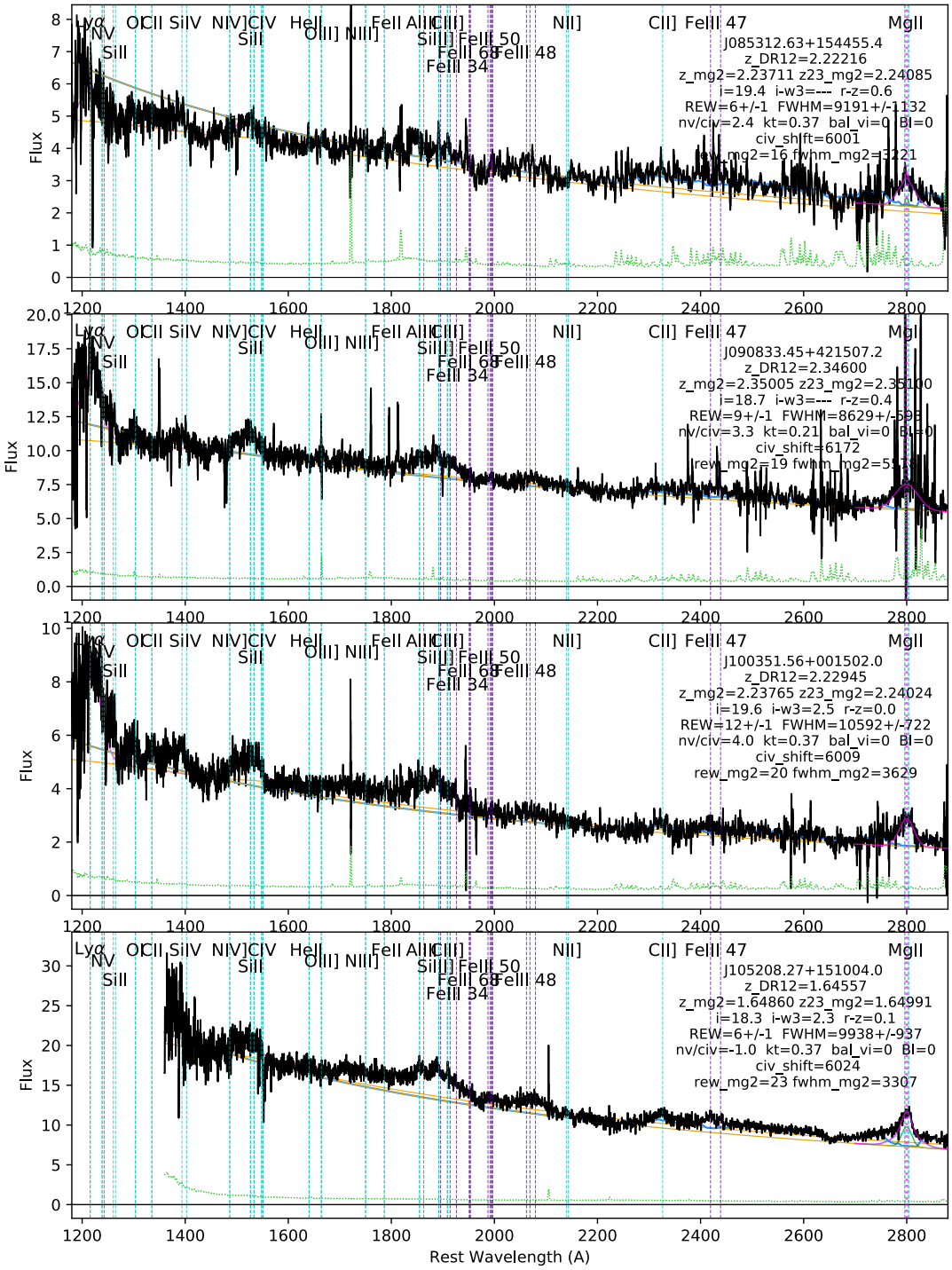

Figure 4.17: *continued.*

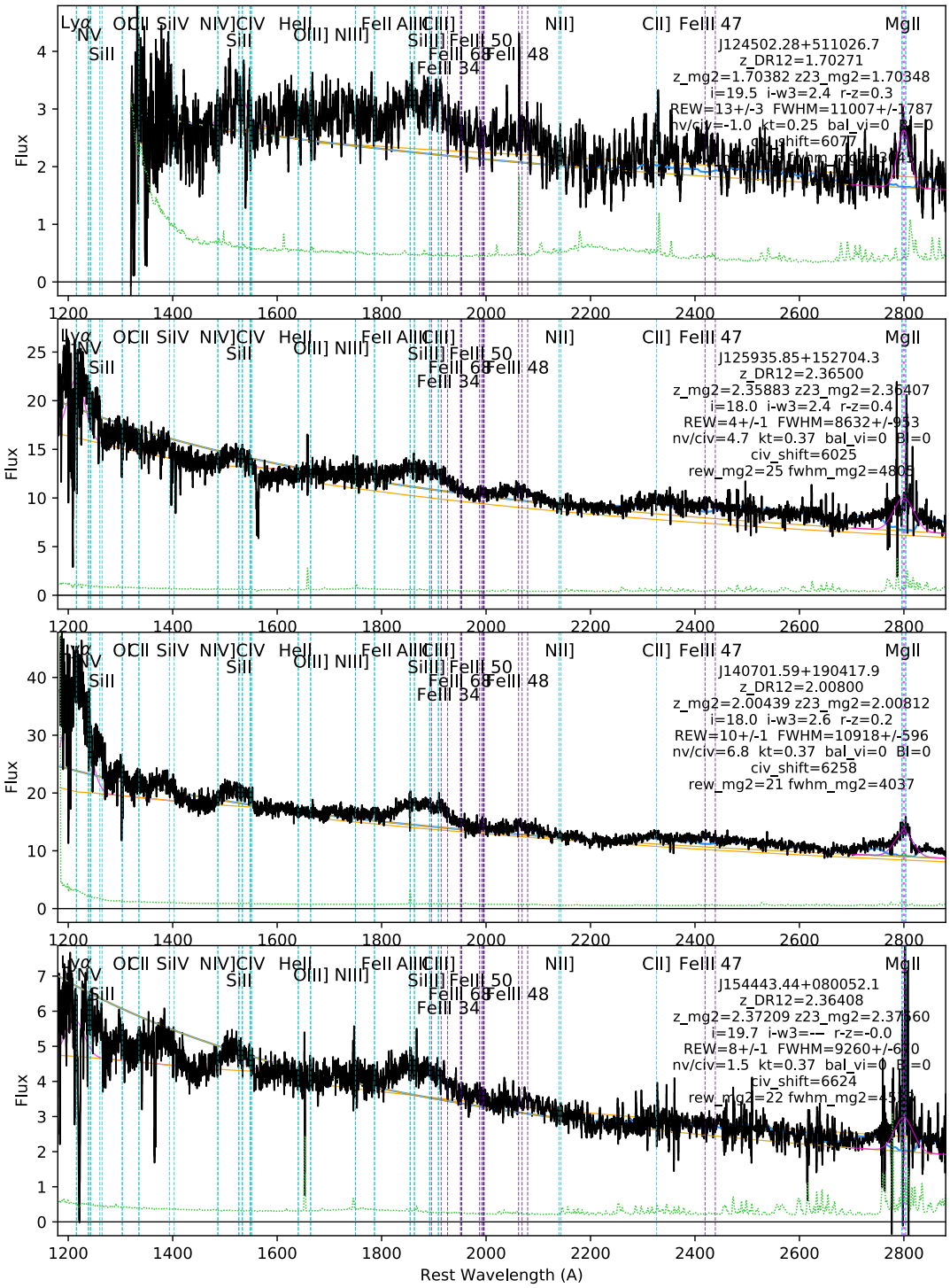

Figure 4.17: *continued.*

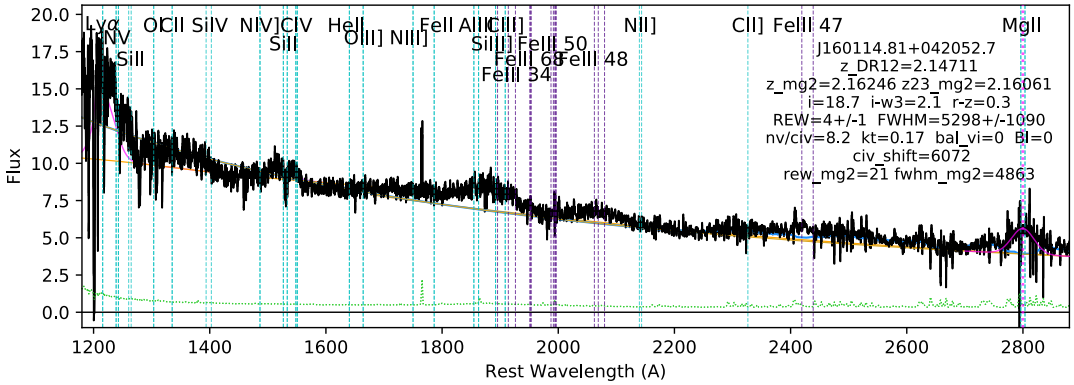

Figure 4.17: *continued.*

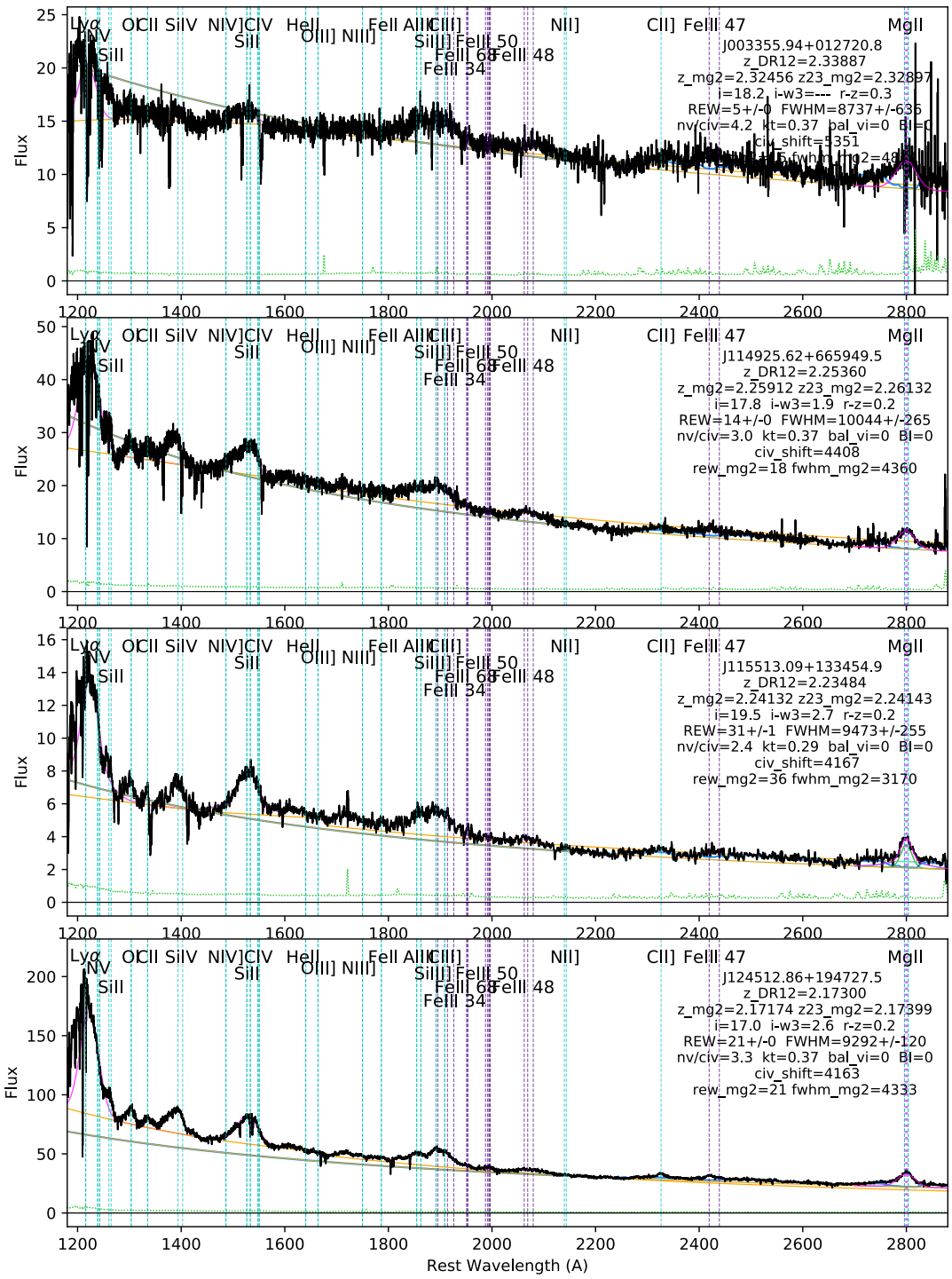

Figure 4.18: Selected spectra with high C IV blueshifts (>4000 km s^{-1}) and goon signal to noise.

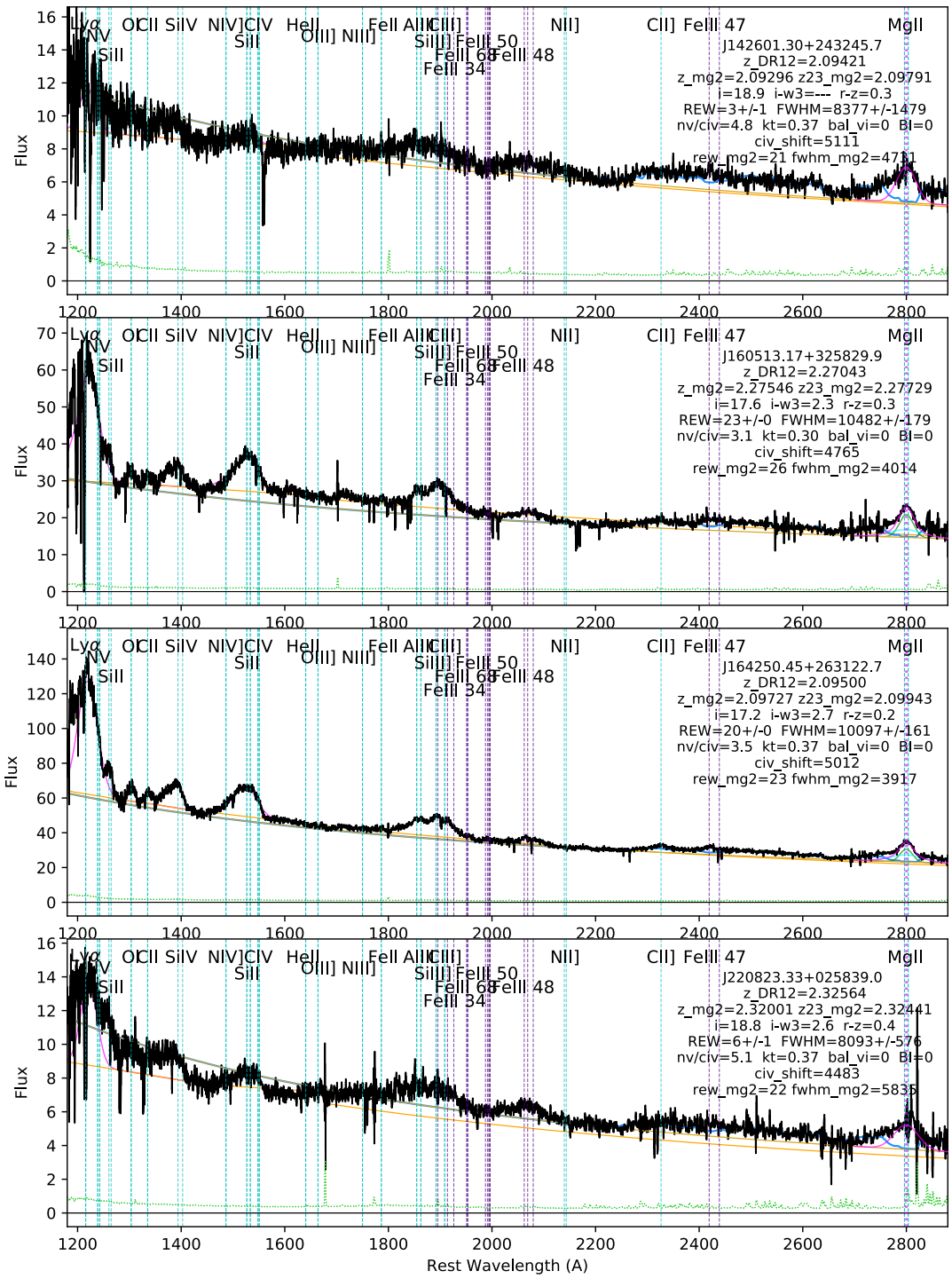

Figure 4.18: *continued.*

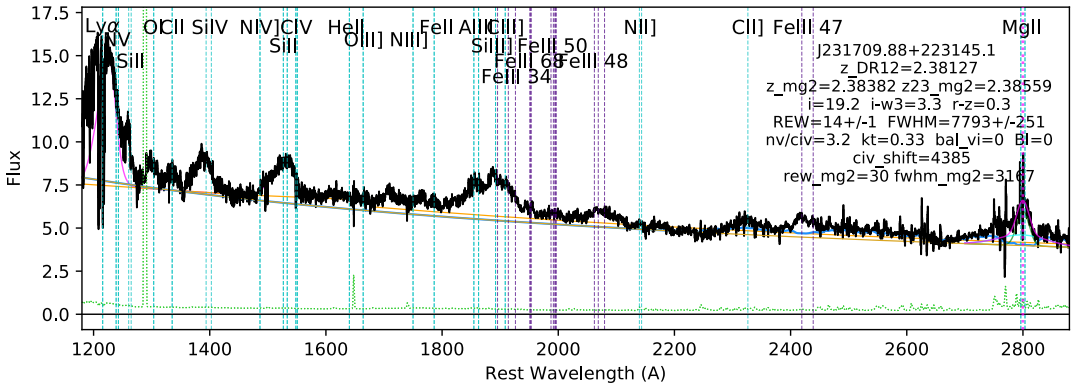

Figure 4.18: *continued.*

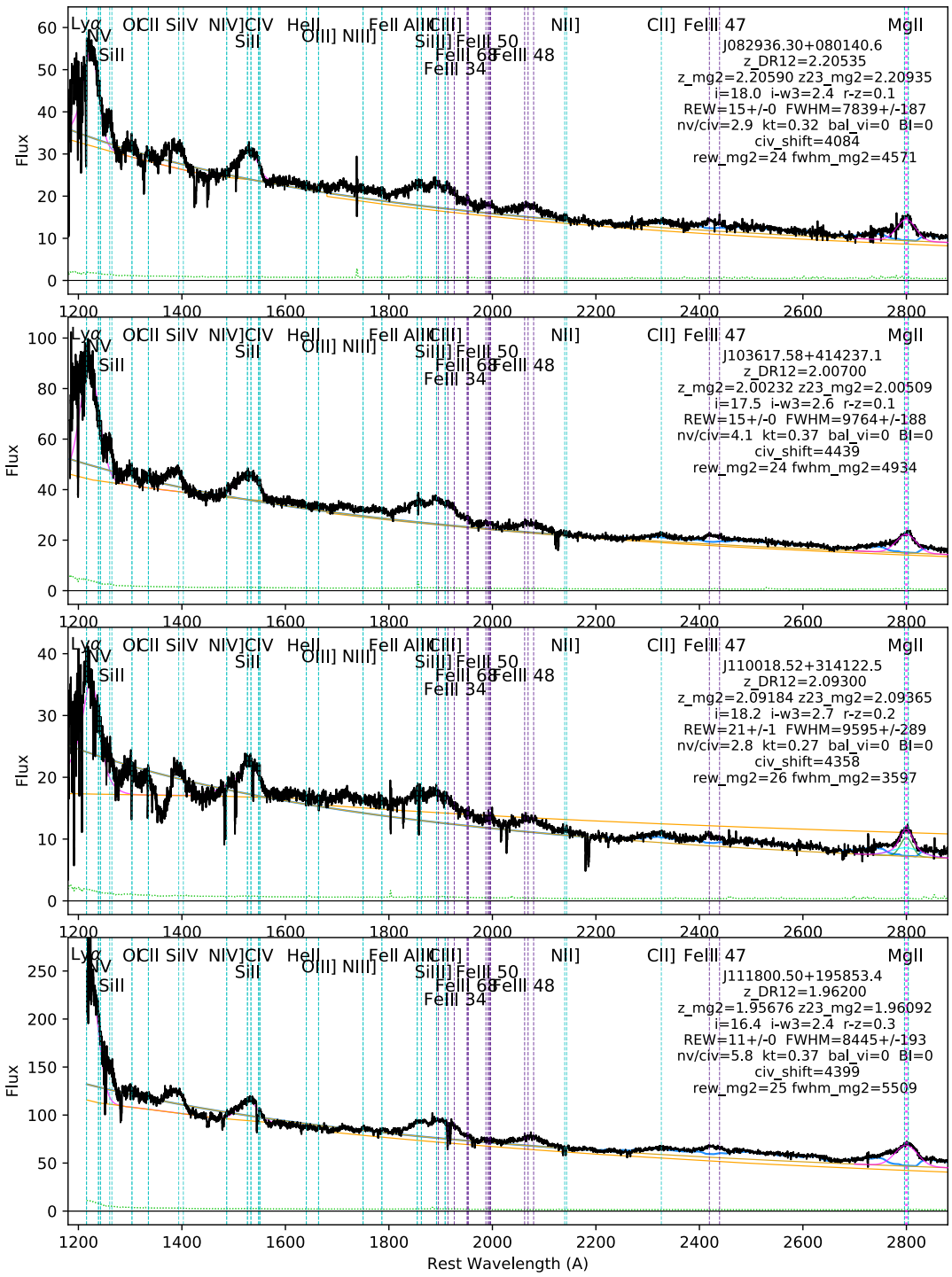

Figure 4.19: Selected spectra with C IV blueshifted 4000 - 5000 km s^{-1}.

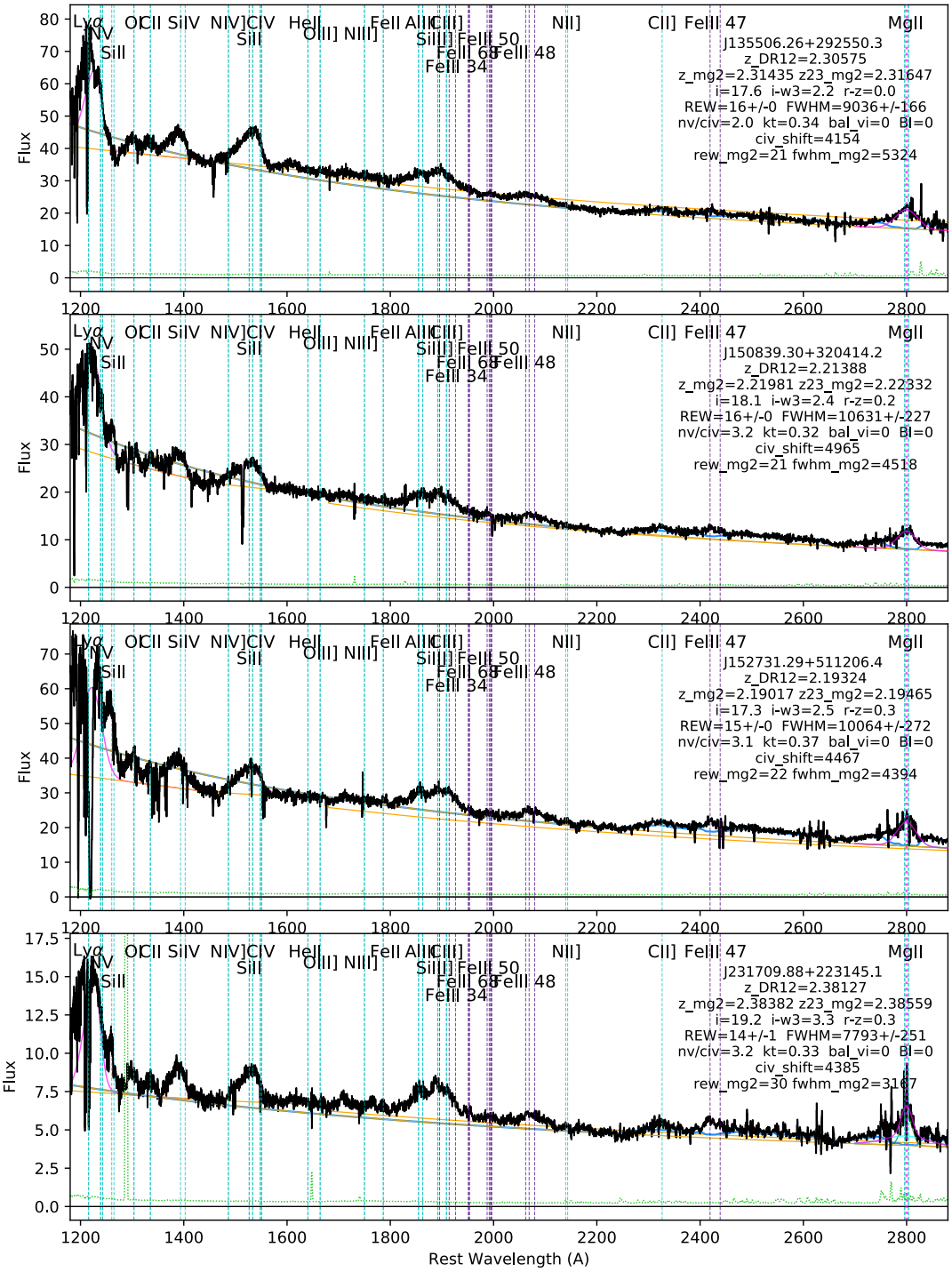

Figure 4.19: *continued.*

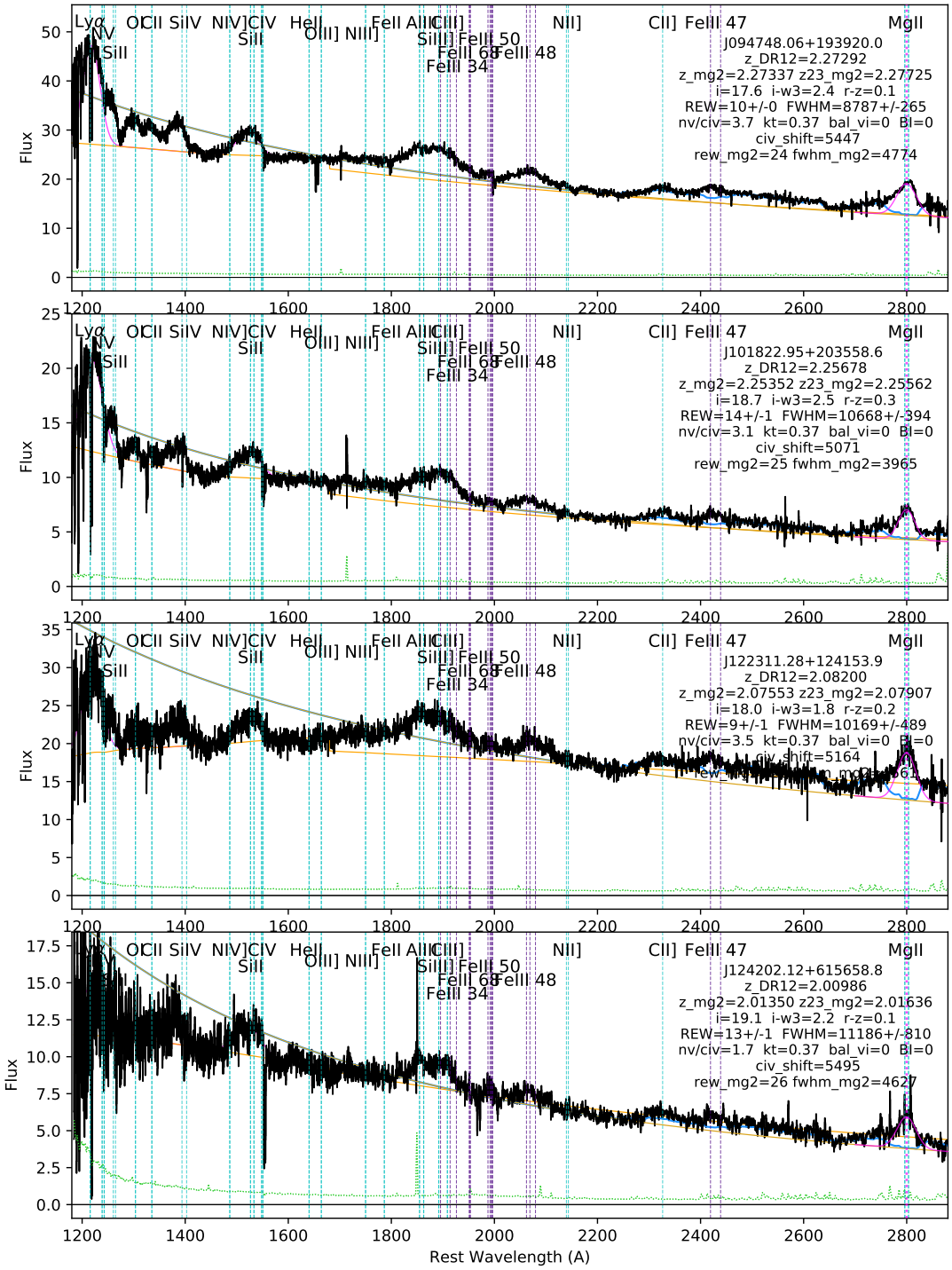

Figure 4.20: Selected spectra with C IV blueshifted 5000 - 6000 km s^{-1}.

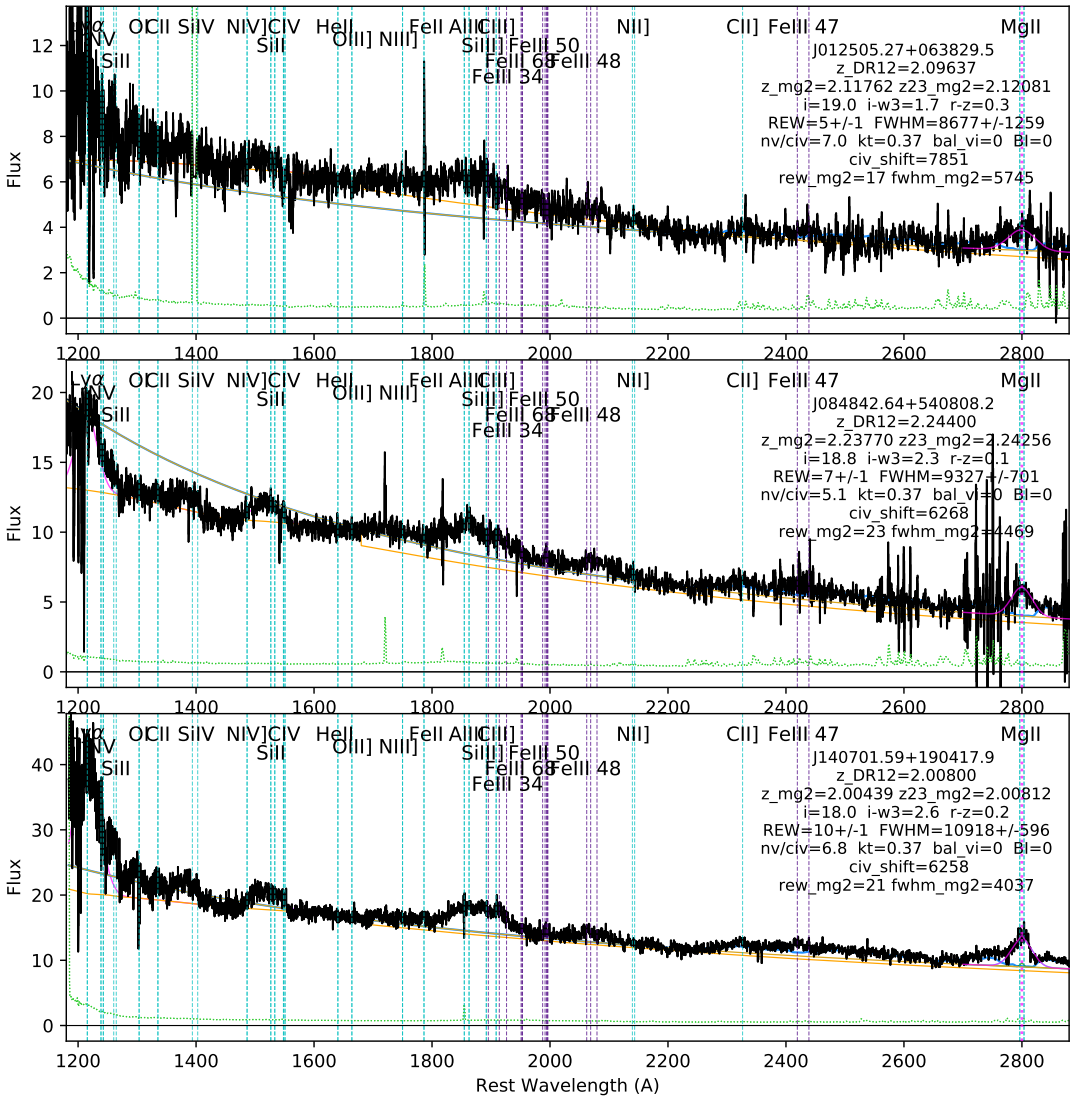

Figure 4.21: Selected spectra with the highest C IV blueshifts of our sample.

4.7 Summary

We present a sample of 39,249 quasars with improved redshift estimates to constrain outflows at extreme speeds, to understand the factors driving outflows across a wide range of velocities. We focus on the blueshift velocities of C IV emission, relative to Mg II, and comparing them with other spectral properties.

This study differs from previous work by determining redshifts solely from the Mg II line, allowing us to explore an unprecedented range of outflow velocities and maintain a statistically significant sample size. We identify two primary factors contributing to stronger outflows: higher Eddington ratios, which provide a stronger radiative driving force relative to gravity, and a softer far-UV continuum, where weaker far-UV flux helps maintain moderate ionization levels and substantial opacities in the outflow.

Our analysis reveals consistent trends, such as the weakening of He II emission with increasing C IV blueshift. High blueshifts correspond to weaker C IV strength and broader emission profiles. This study suggests that radiative line-driving may be a mechanism generating extreme outflows. As the C IV rest equivalent width (REW) decreases with blueshift, low-ionization lines become stronger, and there is a trend of weaker C III] relative to Al III and Si III]. A possible explanations for this trend is higher densities, and/or lower degrees of ionization, at farther BLR distances.

We also find a correlation between larger Eddington ratios and increasing blueshift, and discuss the potential influence of reddening on the Eddington ratios but note that a reddening correction would not undo the observed trends.

Additionally, correlations with SED shape and color are explored. Asymmetric blueshifts in C IV are correlated with bluer continuum colors in the UV, particularly in less luminous quasars. Quasars can have intrinsically redder SEDs without involving dust, and the trends observed in continuum shape and reddening may be attributed to intrinsic color differences in the quasar SEDs.

Finally we look at individual spectra with extreme characteristics in their C IV emission profiles. We confirm the reality of trends measured across the breadth of C IV parameter space, including line strength, profile width, and blueshift.

Our analysis suggests that the relationship between C IV REW and blueshift is better understood in a multi-dimensional parameter space rather than through 2D scatter plots, indicating that blueshifts are influenced by multiple factors. We propose that future studies should investigate where large blueshifts cluster in multi-dimensional parameter space to determine the fundamental causes.

Chapter 5

Conclusions

Collectively the work presented in this dissertation sheds new light on the multifaceted nature of quasar outflows and their implications for quasar evolution and galactic environments. In Chapter 2, the study of Extreme Red Quasars' Lyα halos provides insights into the spatial properties and kinematic characteristics at circumgalactic scales. Chapter 3 extends the investigation to ERQ outflows, revealing their unique properties and challenging conventional norms seen in blue quasars. These extreme outflows prompt inquiries into the underlying driving forces and their potential impact on spectral features. In Chapter 4, a comprehensive analysis of a large quasar sample unveils correlations between outflow velocities, Eddington ratios, and continuum shapes, emphasizing the interplay of these factors in generating the most extreme outflows. Together, these publications contribute a holistic understanding of outflows' complex interdependencies with quasar properties, offering a foundation for future studies into the broader implications of these phenomena for galaxy evolution.

5.1 Big Picture

Collectively our findings from these three publications provide a comprehensive and nuanced understanding of quasar outflow properties, feedback mechanisms, and galactic/quasar evolution. In Chapter 2, the examination of ERQ Lyα halos and their kinematic characteristics unveils insights into the complex interactions between quasar-driven outflows and their galactic environments. By investigating the circular, compact morphology and calm kinematics of these halos, we offer valuable contributions to the understanding of feedback processes and the connections between Lyα emission and host galaxy properties. With velocity shifts of the Lyα emission much weaker, at houndreds of km s^{-1}, than the shifts found in [O III] for ERQs, at thousands of km s^{-1}, potential feedback mechanisms in ERQs may take place on smaller size-scales than the inner halo regions probed.

In Chapter 3, our focus shifts towards a more detailed analysis of ERQ outflows and their implications. The identification of extreme outflows in ERQs, characterized by significant C IV blueshifts, [O III] outflow velocities, and distinctive spectral features, challenges the norms observed in normal blue quasars. These extraordinary outflows prompt inquiries into the underlying driving forces. Obtaining the requisite Bolometric luminosities, for calculating Eddington ratios, proves more intricate for ERQs than for typical blue quasars due to their potentially unconventional intrinsic spectral energy distributions. The potential identification of significant shifts in low-ionization UV lines further highlights the unique nature of ERQs' outflow properties, and their potential influence on broad emission line regions.

Chapter 4 expands our investigation to a broader quasar sample, encompassing a range of outflow velocities. By considering the C IV blueshift velocities relative to Mg II, we discern a complex interplay of factors that influence outflow characteristics. The correlation between Eddington ratios, continuum shapes, and outflow velocities offers intriguing insights into the underlying mechanisms driving these extreme phenomena. Higher Eddington ratios and softer-UV continua emerge as potential contributors to the most extreme outflow velocities. Furthermore, the exploration of individual spectra with exceptional characteristics strengthens the observed trends, and emphasizes the multi-dimensional nature of outflow behavior.

Taken together, these three publications contribute to a comprehensive narrative of quasar evolution and outflows, revealing the intricate relationships between spectral features, kinematics, and galactic environments. The exploration of ERQ properties and their departure from the norm serve as a foundation for understanding the role of outflows in shaping quasar behavior and their potential impacts on host galaxies. As we transition from the ERQ-specific investigations in the first two chapters, to the broader analysis of quasar outflows in the last chapter, we continue to uncover the underlying principles governing these remarkable astrophysical phenomena.

5.2 Future Work

The work presented in this dissertation can be built upon by additional data probing the galaxies hosting ERQs. Size scales probed by Lyα halos leave open the possibility of galactic companion interactions in the extended circumgalactic environment, at the boundary of the intergalactic medium. These inner halo observations also do not resolve compact, fast outflows at smaller scales within the host galaxy. ERQ outflows themselves could be better understood when their quasar properties are constrained, such as Eddington ratio, to determine if the extreme ERQ outflows follow the same trends as normal quasars with high outflow speeds. These comparisons may give clues as to the underling drivers of the unusual ERQ spectral properties and outflows.

Future studies of the fundamental causes of quasar outflows should investigate where large blueshifts cluster in multi-dimensional parameter space. The addition of UV slope and xray properties may strengthen the hypothesis that a softer far-UV spectrum is needed to drive powerful quasar outflows. Exploring deeper into the complex relationships between spectral properties, Eddington ratios, continuum shapes, and other key parameters, we can construct a more comprehensive understanding of the mechanisms driving extreme outflows in quasars, paving the way for insights into the broader implications of these outflows on galactic scale processes and their potential to shape the evolving universe.

Bibliography

Alam S., et al., 2015, ApJS, 219, 12

Alexandroff R., et al., 2013, MNRAS, 435, 3306

Alexandroff R. M., et al., 2018, MNRAS, 479, 4936

Antonucci R., 1993, ARA&A, 31, 473

Arrigoni Battaia F., Hennawi J. F., Prochaska J. X., Oñorbe J., Farina E. P., Cantalupo S., Lusso E., 2019, MNRAS, 482, 3162

Astropy Collaboration et al., 2013, A&A, 558, A33

Astropy Collaboration et al., 2018, AJ, 156, 123

Baldwin J. A., 1977, ApJ, 214, 679

Baron D., Netzer H., Poznanski D., Prochaska J. X., Förster Schreiber N. M., 2017, MNRAS, 470, 1687

Baskin A., Laor A., 2005, MNRAS, 356, 1029

Baskin A., Laor A., Hamann F., 2013, MNRAS, 432, 1525

Bischetti, M. et al., 2017, A&A, 598, A122

Borisova E., Lilly S. J., Cantalupo S., Prochaska J. X., Rakic O., Worseck G., 2016a, ApJ, 830, 120

Borisova E., et al., 2016b, ApJ, 831, 39

Cai Z., et al., 2019, ApJS, 245, 23

Calistro-Rivera G., et al., 2021, A&A, 649, A102

Casebeer D. A., Leighly K. M., Baron E., 2006, ApJ, 637, 157

Chen C., Hamann F., Simon L., Ma B., 2019, ApJ, 887, 78

Coatman L., Hewett P. C., Banerji M., Richards G. T., 2016, MNRAS, 461, 647

Coatman L., Hewett P. C., Banerji M., Richards G. T., Hennawi J. F., Prochaska J. X., 2019, MNRAS, 486, 5335

Costa T., Sijacki D., Haehnelt M. G., 2014, MNRAS, 444, 2355

Costa T., Arrigoni Battaia F., Farina E. P., Keating L. C., Rosdahl J., Kimm T., 2022, MNRAS, 517, 1767

Cutri R. M., et al., 2011, Explanatory Supplement to the WISE Preliminary Data Release Products

Cutri R. M., et al., 2013, Explanatory Supplement to the AllWISE Data Release Products

DeFelippis D., Genel S., Bryan G. L., Nelson D., Pillepich A., Hernquist L., 2020, ApJ, 895, 17

Dekel A., et al., 2009, Nature, 457, 451

Dempsey R., Zakamska N. L., 2018, MNRAS, 477, 4615

Di Matteo T., Springel V., Hernquist L., 2005, Nature, 433, 604

DiPompeo M. A., Hickox R. C., Eftekharzadeh S., Myers A. D., 2017, MNRAS, 469, 4630

Eisenstein D. J., et al., 2011, AJ, 142, 72

Farina E. P., et al., 2019, ApJ, 887, 196

Faucher-Giguère C.-A., Kereš D., 2011, MNRAS, 412, L118

Fawcett V. A., Alexander D. M., Rosario D. J., Klindt L., Fotopoulou S., Lusso E., Morabito L. K., Calistro Rivera G., 2020, MNRAS, 494, 4802

Fossati M., et al., 2021, MNRAS, 503, 3044

Fumagalli M., Hennawi J. F., Prochaska J. X., Kasen D., Dekel A., Ceverino D., Primack J., 2014, ApJ, 780, 74

Gallagher S. C., Richards G. T., Hall P. B., Brandt W. N., Schneider D. P., Berk D. E. V., 2005, AJ, 129, 567

Gardner J. P., et al., 2006, SSR, 123, 485

Gaskell C. M., 1982, ApJ, 263, 79

Geach J. E., Peacock J. A., Myers A. D., Hickox R. C., Burchard M. C., Jones M. L., 2019, ApJ, 874, 85

Gillette J., Hamann F., 2023, BOSS Quasar Outflows Traced by C IV (arXiv:2309.02490)

Gillette J., Hamann F., Lau M. W., Perrotta S., 2023a, Accurate Systemic Redshifts and Outflow Speeds for Extremely Red Quasars (ERQs) (arXiv:2305.11223)

Gillette J., Lau M. W., Hamann F., Perrotta S., Rupke D. S. N., Wylezalek D., Zakamska N. L., Vayner A., 2023b, Compact and Quiescent Circumgalactic Medium and Lyα Halos around Extremely Red Quasars (ERQs) (arXiv:2303.12835)

Glikman E., Helfand D. J., White R. L., Becker R. H., Gregg M. D., Lacy M., 2007, ApJ, 667, 673

Glikman E., Simmons B., Mailly M., Schawinski K., Urry C. M., Lacy M., 2015, ApJ, 806, 218

Glikman E., et al., 2022, ApJ, 934, 119

Greene J. E., et al., 2014, ApJ, 788, 91

Hamann F., Sabra B., 2004, in Richards G. T., Hall P. B., eds, AGN Physics with the Sloan Digital Sky Survey. ASP Conference Series. pp 203–213

Hamann F., Kanekar N., Prochaska J. X., Murphy M. T., Ellison S., Malec A. L., Milutinovic N., Ubachs W., 2011, MNRAS, 410, 1957

Hamann F., et al., 2017, MNRAS, 464, 3431

Hamann F., Herbst H., Paris I., Capellupo D., 2018, MNRAS, 483, 1808

Harris D. W., et al., 2016, AJ, 151, 155

Hewett P. C., Wild V., 2010, MNRAS, 405, 2302

Hopkins P. F., Hernquist L., Cox T. J., Di Matteo T., Robertson B., Springel V., 2006, ApJS, 163, 1

Hopkins P. F., Hernquist L., Cox T. J., Kereš D., 2008, ApJS, 175, 356

Hopkins P. F., Torrey P., Faucher-Giguère C.-A., Quataert E., Murray N., 2016, MNRAS, 458, 816

Hunter J. D., 2007, CS&E, 9, 90

Huscher E., Oppenheimer B. D., Lonardi A., Crain R. A., Richings A. J., Schaye J., 2021, MNRAS, 500, 1476

Kereš D., Katz N., Fardal M., Davé R., Weinberg D. H., 2009, MNRAS, 395, 160

Khrykin I. S., Hennawi J. F., Worseck G., Davies F. B., 2021, MNRAS, 505, 649

Klindt L., Alexander D. M., Rosario D. J., Lusso E., Fotopoulou S., 2019, MNRAS, 488, 3109

Lau M. W., Hamann F., Gillette J., Perrotta S., Rupke D. S. N., Wylezalek D., Zakamska N. L., 2022, MNRAS, 515, 1624

Leighly K. M., 2004, ApJ, 611, 125

Leighly K. M., Moore J. R., 2004, ApJ, 611, 107

Li J., et al., 2017, ApJ, 846, 79

Li Z., Steidel C. C., Gronke M., Chen Y., 2020, MNRAS, 502, 2389

Liu G., Zakamska N. L., Greene J. E., Nesvadba N. P. H., Liu X., 2013, MNRAS, 436, 2576

Mackenzie R., et al., 2021, MNRAS, 502, 494

Margala D., Kirkby D., Dawson K., Bailey S., Blanton M., Schneider D. P., 2016, ApJ, 831, 157

Marino R. A., et al., 2019, ApJ, 880, 47

Monadi R., Bird S., 2022, MNRAS, 511, 3501

Morrissey P., et al., 2018, ApJ, 864, 93

Muzahid S., Srianand R., Arav N., Savage B. D., Narayanan A., 2013, MNRAS, 431, 2885

Navarro J. F., Frenk C. S., White S. D. M., 1997, ApJ, 490, 493

Nelson D., Genel S., Vogelsberger M., Springel V., Sijacki D., Torrey P., Hernquist L., 2015, MNRAS, 448, 59

Netzer H., 2015, ARA&A, 53, 365

Netzer H., 2019, MNRAS, 488, 5185

Netzer H., 2020, MNRAS, 494, 1611

O'Sullivan D., Chen Y., 2020, arXiv e-prints, p. arXiv:2011.05444

O'Sullivan D. B., Martin C., Matuszewski M., Hoadley K., Hamden E., Neill J. D., Lin Z., Parihar P., 2020, ApJ, 894, 3

Oliphant T. E., 2007, CS&E, 9, 10

Pâris I., et al., 2014, A&A, 563, A54

Pâris I., et al., 2017b, A&A, 597, A79

Pâris I., et al., 2017a, A&A, 597, A79

Perrotta S., Hamann F., Zakamska N. L., Alexandroff R. M., Rupke D., Wylezalek D., 2019, MNRAS, 488, 4126

Peterson B. M., et al., 2004, ApJ, 613, 682

Rankine A. L., Hewett P. C., Banerji M., Richards G. T., 2020, MNRAS, 492, 4553

Richards G. T., Vanden Berk D. E., Reichard T. A., Hall P. B., Schneider D. P., SubbaRao M., Thakar A. R., York D. G., 2002, AJ, 124, 1

Richards G. T., et al., 2003, AJ, 126, 1131

Richards G. T., et al., 2011, AJ, 141, 167

Richards G. T., Plotkin R. M., Hewett P. C., Rankine A. L., Rivera A. B., Shen Y., Shemmer O., 2021, ApJL, 914, L14

Rosario D. J., Fawcett V. A., Klindt L., Alexander D. M., Morabito L. K., Fotopoulou S., Lusso E., Calistro Rivera G., 2020, MNRAS, 494, 3061

Ross N. P., et al., 2015, MNRAS, 453, 3932

Rupke D., To A., 2021, IFSFIT: Integral Field Spectroscopy FITting, doi:10.5281/zenodo.5659520

Rupke D. S. N., Veilleux S., 2011, ApJL, 729, L27

Rupke D. S. N., Veilleux S., 2013, ApJ, 768, 75

Rupke D. S. N., Gültekin K., Veilleux S., 2017, ApJ, 850, 40

Rupke D. S. N., et al., 2019, Nature, 574, 643

Salviander S., Shields G. A., Gebhardt K., Bonning E. W., 2007, ApJ, 662, 131

Sanders D. B., Soifer B. T., Elias J. H., Neugebauer G., Matthews K., 1988, ApJL, 328, L35

Sanderson K. N., Prescott M. M. K., Christensen L., Fynbo J., Møller P., 2021, ApJ, 923, 252

Shen Y., Liu X., 2012, ApJ, 753, 125

Shen Y., et al., 2007, AJ, 133, 2222

Shen Y., Greene J. E., Strauss M. A., Richards G. T., Schneider D. P., 2008, ApJ, 680, 169

Shen Y., et al., 2016a, ApJ, 818, 30

Shen Y., et al., 2016b, ApJ, 831, 7

Shen Y., et al., 2019, ApJS, 241, 34

Shen X., Hopkins P. F., Faucher-Giguère C.-A., Alexander D. M., Richards G. T., Ross N. P., Hickox R. C., 2020, MNRAS, 495, 3252

Somerville R. S., Hopkins P. F., Cox T. J., Robertson B. E., Hernquist L., 2008, MNRAS, 391, 481

Sorini D., Dave R., Cui W., Appleby S., 2021, arXiv e-prints, p. arXiv:2111.13708

Stacey H. R., Costa T., McKean J. P., Sharon C. E., Rivera G. C., Glikman E., van der Werf P. P., 2022, MNRAS

Suresh J., Nelson D., Genel S., Rubin K. H. R., Hernquist L., 2019, MNRAS, 483, 4040

Temple M. J., Banerji M., Hewett P. C., Rankine A. L., Richards G. T., 2020, MNRAS, 501, 3061

Temple M. J., et al., 2023, Testing AGN outflow and accretion models with CIV and HeII emission line demographics in z=2 quasars (arXiv:2301.02675)

Tumlinson J., Peeples M. S., Werk J. K., 2017, ARA&A, 55, 389

Urry C. M., Padovani P., 1995, PASP, 107, 803

Vayner A., et al., 2021, MNRAS, 504, 4445

Vayner A., et al., 2023, arXiv e-prints, p. arXiv:2303.06970

Veilleux S., Meléndez M., Tripp T. M., Hamann F., Rupke D. S. N., 2016, ApJ, 825, 42

Vestergaard M., Wilkes B. J., 2001, ApJS, 134, 1

Vietri, G. et al., 2018, A&A, 617, A81

Wang J.-G., et al., 2009, ApJ, 707, 1334

Wang W., Wylezalek D., De Breuck C., Vernet J., Humphrey A., Villar Martín M., Lehnert M. D., Kolwa S., 2021, A&A, 654, A88

Weymann R. J., Morris S. L., Foltz C. B., Hewett P. C., 1991, ApJ, 373, 23

Woo J.-H., Le H. A. N., Karouzos M., Park D., Park D., Malkan M. A., Treu T., Bennert V. N., 2018, ApJ, 859, 138

Wright E. L., 2006, PASP, 118, 1711

Wright E. L., et al., 2010a, AJ, 140, 1868

Wright E. L., et al., 2010b, AJ, 140, 1868

Wu J., et al., 2018, ApJ, 852, 96

Wylezalek D., Zakamska N. L., 2016, MNRAS, 461, 3724

Wylezalek D., et al., 2022, ApJL, 940, L7

Yan L., et al., 2013, AJ, 145, 55

York D. G., et al., 2000, AJ, 120, 1579

Zakamska N. L., et al., 2016, MNRAS, 459, 3144

Zakamska N. L., et al., 2019, MNRAS, 489, 497

Zhang S., et al., 2017, ApJ, 836, 86

den Brok J. S., et al., 2020, MNRAS, 495, 1874